MODELLING OF ANOMALOUS CHARGE CARRIERS TRANSPORT IN DISORDERED ORGANIC SEMICONDUCTORS

CHOO KAN YEEP

FACULTY OF SCIENCE
UNIVERSITY OF MALAYA
KUALA LUMPUR

2017

MODELLING OF ANOMALOUS CHARGE CARRIERS TRANSPORT IN DISORDERED ORGANIC SEMICONDUCTORS

CHOO KAN YEEP

THESIS SUBMITTED IN FULFILMENT OF THE REQUIREMENTS FOR THE DEGREE OF DOCTOR OF PHILOSOPHY

DEPARTMENT OF PHYSICS
FACULTY OF SCIENCE
UNIVERSITY OF MALAYA
KUALA LUMPUR

2017

UNIVERSITY OF MALAYA
ORIGINAL LITERARY WORK DECLARATION

Name of Candidate: **CHOO KAN YEEP**

Matric No: **SHC100060**

Name of Degree: **DOCTOR OF PHILOSOPHY**

Title of Thesis (“this Work”):

MODELLING OF ANOMALOUS CHARGE CARRIERS TRANSPORT IN DISORDERED ORGANIC SEMICONDUCTORS

Field of Study:

THEORETICAL PHYSICS

I do solemnly and sincerely declare that:

(1) I am the sole author/writer of this Work;
(2) This Work is original;
(3) Any use of any work in which copyright exists was done by way of fair dealing and for permitted purposes and any excerpt or extract from, or reference to or reproduction of any copyright work has been disclosed expressly and sufficiently and the title of the Work and its authorship have been acknowledged in this Work;
(4) I do not have any actual knowledge nor do I ought reasonably to know that the making of this work constitutes an infringement of any copyright work;
(5) I hereby assign all and every rights in the copyright to this Work to the University of Malaya (“UM”), who henceforth shall be owner of the copyright in this Work and that any reproduction or use in any form or by any means whatsoever is prohibited without the written consent of UM having been first had and obtained;
(6) I am fully aware that if in the course of making this Work I have infringed any copyright whether intentionally or otherwise, I may be subject to legal action or any other action as may be determined by UM.

Candidate’s Signature Date:

Subscribed and solemnly declared before,

Witness’s Signature Date:

Name:

Designation:

ABSTRACT

Performance of organic devices is affected by material disorders, which yields low mobility, dispersive current and scaling noise behaviour. Anomalous transport and scaling noise behaviour are inadequately described by Fick's law and characterised by low-frequency noise method. This work reports the study of (i) scaling behaviour of current noise in organic field-effect transistors (OFETs) using methods of fractal noise analysis and, (ii) the modelling of anomalous charge transports in disordered organic semiconductors based on fractional calculus. Current noises of Poly(3-hexylthiophene) (P3HT) OFETs were measured at various source-drain voltages (V_{ds}) and characterised using the power spectral density method and detrended fluctuation analysis. Current noises were found to follow white noise, $1/f$ and Brownian noise characteristic at low, intermediate and high V_{ds}, respectively. For V_{ds} above -40 V, Brownian noise will be masked out by $1/f$ noise. Multiple-trapping mechanism is integrated with the drift-diffusion equation and then generalised to the time-fractional drift-diffusion equation (TFDDE) to model the anomalous transports and reproduce the transient photocurrents in regiorandom P3HT (RRa-P3HT) and regioregular P3HT (RR-P3HT). The TFDDE is solved by using finite difference scheme and Poisson solver is implemented to calculate the electric field. It is found that by acquiring extra energy from high electric field, charge carriers escape easily from trap centres and propagate with higher velocity resulting in higher current. Larger amount of charge carriers will be generated at higher illumination and they will be hopping near the mobility edges, hence encountering lesser capturing events. This explains why movement of charge carriers at higher illumination is less dispersive than the movement of charge carriers at lower illumination. It is also noted that transport dynamic of charge carriers in RR-P3HT is relatively less dispersive and has higher mobility than that of the RRa-P3HT since RR-P3HT has lower capturing rate and is less energetically disordered.

ABSTRAK

Prestasi peranti organik dipengaruhi oleh kecelaruan bahan yang menghasilkan mobiliti rendah, serakan arus elecktrik dan sifat hingar berskala. Angkutan anomali dan sifat hingar berskala adalah tidak sesuai diterangkan oleh hukum Fick dan dicirikan oleh kaedah hingar frekuensi-rendah. Kajian ini bertujuan untuk (i) mengkaji sifat hingar berskala arus elektrik dalam transistor kesan-medan organik (OFETs) dengan menggunakan kaedah analisis hingar fraktal dan (ii) untuk permodelan angkutan anomali dalam semikonduktor organik bercelaru berdasarkan kalkulus pecahan. Hingar arus elektrik untuk Poly(3-hexylthiophene) (P3HT) OFETs diukur pada pelbagai voltan salir-sumber (V_{ds}) dan kemudian dianalisiskan dengan kaedah ketumpatan spektra kuasa dan analisis fluktuasi nyahpola. Hingar arus elektrik yang bersifat putih, $1/f$ dan Brown ditunjukkan masing-masing pada V_{ds} rendah, pertengahan dan tinggi. Hingar Brown akan dihilangkan oleh hingar $1/f$ untuk V_{ds} yang lebih tinggi dari -40 V. Mekanisme perangkap berganda disepadukan dengan persamaan resapan-hayutan dan kemudian diitlakkan ke persamaan resapan-hayutan pecahan masa (PRHPM) untuk memodel angkutan anomali dan menghasilkan arusfoto elektrik semasa dalam regiorandom P3HT (RRa-P3HT) dan regioregular P3HT (RR-P3HT). PRHPM diselesaikan dengan kaedah perbezaan terhingga dan penyelesaian Poisson juga dilaksanakan untuk penghitungan medan elektrik. Penghasilan arus yang lebih tinggi pada medan elektrik tinggi adalah disebabkan oleh pembebasan dan perlonjatan pembawa cas dari pusat perangkap yang lebih mudah. Pergerakan pembawa cas pada pencahayaan tinggi adalah kurang terserak kerana cas melompat berhampiran pinggiran mobiliti dengan menghadapi perangkapan yang lebih kecil. Selain itu, dinamik angkutan pembawa cas dalam RR-P3HT adalah kurang terserak dan mempunyai mobiliti lebih tinggi dari RRa-P3HT kerana RR-P3HT mempunyai kadar perangkapan yang lebih rendah dan kurang tenaga bercelaru.

ACKNOWLEDGEMENTS

First and foremost, I would like to express my sincere gratitude to my supervisors Prof. Dr. Sithi V. Muniandy and Dr. Woon Kai Lin for their continuous knowledge sharing, motivation, encouragement and support given to me during my study.

I would like to thank Dr. C. L. Chua for his help in fabrication of OFET and current-voltage measurements. I would also like to thank Mr. Gan Ming Tao for his precious time spent in several detailed discussions about the mathematical techniques required in my works.

In particular, I am deeply grateful to Dr. Renat T. Sibatov for his kindness and precious times spent in numerous discussions on the anomalous transport theory in disordered materials. I am also very grateful to Dr. Frédéric Laquai (Max Planck Institute for Polymer Research, Germany) for providing me the detailed information on the device parameters and experiment conditions of the time-of-flight measurements published in his works.

Last but not least, my sincere thanks go to my parents, siblings and friends who have been consistently supporting me throughout the journey of my study and thesis writing.

TABLE OF CONTENTS

LIST OF FIGURES

LIST OF TABLES

LIST OF SYMBOLS AND ABBREVIATIONS

AlGaAs	:	Aluminium gallium arsenide
C_{10}-DNTT	:	2,9-di-decyl-dinaphtho-[2,3-b:20,30-f]-thieno-[3,2-b]-thiophene
C_8-BTBT	:	2,7-dioctyl[1]benzothieno[3,2-b][1]benzothiophene
CELIV	:	Charge extraction by linearly increasing voltage
C_n-BTBT	:	2,7-dialkyl[1]benzothieno[3,2-b][1]-benzothiophene
CP	:	Caputo
CTRW	:	Continuous-time random walk
DDE	:	Drift-diffusion equation
DE	:	Diffusion equation
DFA	:	Detrended fluctuation analysis
DLA	:	Diffusion-limited aggregation
DMM	:	Digital multimeter
DOS	:	Density of states
DSA	:	Dynamic signal analyser
DUT	:	Device under test
FBM	:	Fractional Brownian motion
FDDE	:	Fractional drift-diffusion equation
FDE	:	Fractional diffusion equation
FET	:	Field-effect transistor
FFPE	:	Fractional Fokker-Planck equation
FFT	:	Fast Fourier transform
FKKE	:	Fractional Klein-Kramer equation
FLE	:	Fractional Langevin equation
FPE	:	Fokker-Planck equation

GaAs	:	Gallium arsenide
GaInP	:	Gallium indium phosphide
GDM	:	Gaussian disorder model
GL	:	Grüwald-Letnikov
GLE	:	Generalised Langevin equation
HBT	:	Heterojunction bipolar transistors
HMDS	:	Hexamethyldisilazane
IFS	:	Iterated function system
InGaAs	:	Indium gallium arsenide
InP	:	Indium phosphide
KCl	:	Potassium chloride
L.H.S.	:	Left hand side
LE	:	Langevin equation
LFN	:	Low-frequency noise
MATR	:	Miller-Abrahams transition rate
MSD	:	Mean squared displacement
MTR	:	Marcus transition rate
MVRHM	:	Mott variable range hopping model
NDI	:	Naphthalene diimide
OFET	:	Organic field-effect transistor
OLED	:	Organic light-emitting diode
OSC	:	Organic solar cell
OSK	:	Oscilloscope
OTFT	:	Organic thin-film transistor
OTS	:	Octadecyl triethoxysilane
P3HT	:	Poly(3-hexylthiophene)

PBI	:	Perylene Bisimide
PCE	:	Power conversion efficiency
PDE	:	Partial differential equation
PDF	:	Probability density function
PDVT	:	Poly[2,5-bis(alkyl)pyrrolo[3,4-*c*]pyrrole-1,4(*2H*,*5H*)-dione-*alt*-5,5′-di(thiophen-2-yl)-2,2′-(*E*)-2-(2-(thiophen-2-yl)vinyl)thiophene]
PSA	:	Power spectrum analyser
PSD	:	Power spectral density
R.H.S.	:	Right hand side
r.m.s.	:	Root mean square
RL	:	Riemann-Liouville
RRa-P3HT	:	Regiorandom poly(3-hexylthiophene)
RR-P3HT	:	Regioregular poly(3-hexylthiophene)
RTS	:	Random telegraph signal
S/N	:	Signal-to-noise
SHG	:	Optical second-harmonics-generation
SiO_2	:	Silicon dioxide
SMU	:	Source-measurement unit
TFDDE	:	Time-fractional drift-diffusion equation
TOF	:	Time-of-flight
TFT		Thin-film transistor
VO-TFDDE	:	Variable-order time-fractional drift-diffusion equation
$C_{B_H(t)}\left(t_1,t_2\right)$	:	Covariance of $B_H(t)$
${}_{0}^{RL}D_t^{\alpha}$	:	RL factional derivative operator of order α
${}_{0}^{C}D_t^{\alpha}$	:	Caputo factional derivative operator of order α

${}_{-\infty}^{W}D_t^{\alpha}$: Weyl factional derivative operator of order α

${}_{0}^{RL}D_t^{-\alpha}$: RL factional integral operator of order α

${}_{0}^{C}D_t^{-\alpha}$: Caputo factional integral operator of order α

${}_{-\infty}^{W}D_t^{-\alpha}$: Weyl factional integral operator of order α

${}_{a}D_t^{\alpha}$ or $\partial^{\alpha}/\partial t^{\alpha}$: Factional derivative operator of order α

${}_{a}D_t^{-\alpha}$ or $\partial^{-\alpha}/\partial t^{-\alpha}$: Factional integral operator of order α

μ : Mobility

η : Friction constant

α : Disorder parameter or fractional derivative order

$\Gamma(\alpha)$: Gamma function with real argument α

$\lambda(k)$: Fourier transform of $\lambda(x)$

$\Psi(t)$: Cumulative jump probability within $(0,t)$

$\lambda(x)$: Jump length PDF

$\delta(x)\delta(t)$: Initial condition of random walker

$\alpha(x,t)$: Disorder parameter or fractional derivative order in space and time

$\rho(x,t)$: Charge density

τ_0 : Average time of delocalisation

ω_0 : Capture rate of charge carrier into the localised state

ε_0 : Permittivity of vacuum

σ^2 : Laplace transform of spatial step

τ_c : Characteristic waiting time

τ_{D} : Deep trapping lifetime

α_{DFA} : Scaling exponent for DFA

β_{PS} : Scaling exponent of PSD

ε_{r} : Relative permittivity of material

τ_{rc} : RC time constant

Δt : Time interval

Δx : Space interval

$1/f$: Flicker noise

$B_H(t)$: Fractional Brownian motion

c : Charge carrier capture coefficient

$c(x,t)$: Concentration of particle

C_i : Capacitance

D : Diffusion coefficient

D_α : Anomalous diffusion coefficient

D_B : Box dimension

D_f : Fractal dimension

D_H : Hausdorff dimension

e : Electronic charge

$E[B_H(t)]$: Mean of $B_H(t)$

E_0 : Mean value of the exponential energy DOS of charge carrier

f : Frequency

$F(x)$: External force

$f(x,t)$: Function of space x and time t

H : Hurst exponent

i : Space index

$I_T(t)$: Average current density

$j(x,t)$: Flow current density

k : Time index

K_α : Anomalous diffusion constant

$K_\alpha(x,t)$: Anomalous advection coefficient at x and t

k_B : Boltzmann constant

L : Device length

l_d : Average length of delocalisation

m : Mass of particle

N : Total number of particles

$n(x',t')$: PDF just arrived at position x' at time t'

$p(x,0)\delta(t)$: Initial photo-generated charge carriers

$p(x,t)$: Total charge carrier density at x and t

$p_f(x,t)$: Sum of free charge carrier density at x and t

$p_t(x,t)$: Sum of trap charge carrier density at x and t

r_1 : Transition probability of flow to right

r_2 : Transition probability of flow to left

s : Time variable

$S(f)$: Power spectral density

t : Time variable

T : Temperature

t_tr : Transit time

$v(\mathrm{x})$: Velocity

$V(x)$: Applied potential

V_a : Applied bias

$Var[B_H(t)]$: Variance of $B_H(t)$

V_{ds} : Source-drain voltage

V_g : Gate voltage

V_s : Source voltage

V_{th} : Threshold voltage

$W(k,u)$: Fourier-Laplace of $W(x,t)$

$w(t)$: Waiting time PDF

$w(u)$: Laplace transform of $w(t)$

$W(x,t)$: PDF of being in x at time t

$W_0(k)$: Fourier transform of $W_0(x)$

$W_0(x)$: Initial condition of $W(x,t)$

x : Position in one-dimensional Cartesian-coordinate space

$Y(j)$: Integrated time series

Σ^2 : Jump length variance

LIST OF APPENDICES

CHAPTER 1: INTRODUCTION

A brief overview on the prospects and challenges faced in organic electronics is provided in this chapter together with the motivation and objectives of this work. Besides, the outline of the thesis is also presented at the end of this chapter.

1.1 Prospects and challenges in organic electronics

Since the first conducting polymer reported in 1970's (Heeger et al., 2002), organic semiconductor and polymer materials have drawn tremendous research and also industry attentions due to their several key advantages, namely: (i) low temperature and relatively simple processing yield energy-efficient production and reduction in manufacturing cost, (ii) versatility of synthesis processes which facilitate the production of enormous choices of engineered organic semiconductors and polymer materials for enhancement in mobility, light conversion efficiency, temperature resistance and long term stability, (iii) well-matched on a wide range of flexible plastic substrates and transparent glasses and (iv) continuous improvement on large-area printing technique which allows high throughput production of organic semiconductor and polymer devices.

Owing to the above mentioned advantages, organic semiconductors and polymers have become very promising choices of materials for realisation of flexible display and lighting technologies, large-area printable optoelectronic devices for energy harvesting, flexible and wearable electronic and optoelectronic devices and organic sensors, which are fabricated based on organic light-emitting diodes (Ho et al., 2015), organic solar cells (Milichko et al., 2016) and organic field-effect transistors (Sirringhaus, 2014). Anticipating the coming of new applications of OLEDs and OFETs is certainly tempting, and has been envisioned in Figure 1.1. Besides, there are also research interests branching into production of green materials and devices that possess human and environmentally friendly features, including biodegradability and biocompatible (Irimia-Vladu, 2014).

Figure 1.1: Green electronics: biodegradable and biocompatible materials and devices for sustainable future. (Irimia-Vladu, 2014)

IDTechEx forecasted that investments in producing cheap and high performance organic semiconductor or polymer-based optoelectronic and electronic devices will be continuously growing and generating a market worth of US$70 billion in 2027 from the current market value of US$29 billion in 2017. As shown in Figure 1.2, the main contributors to the total market worth are due to OLEDs and conductive ink. In additions, a great potential market growth is expected for flexible electronics, logic and memory, and thin film sensors due to the advancement in research and development (Das, 2017).

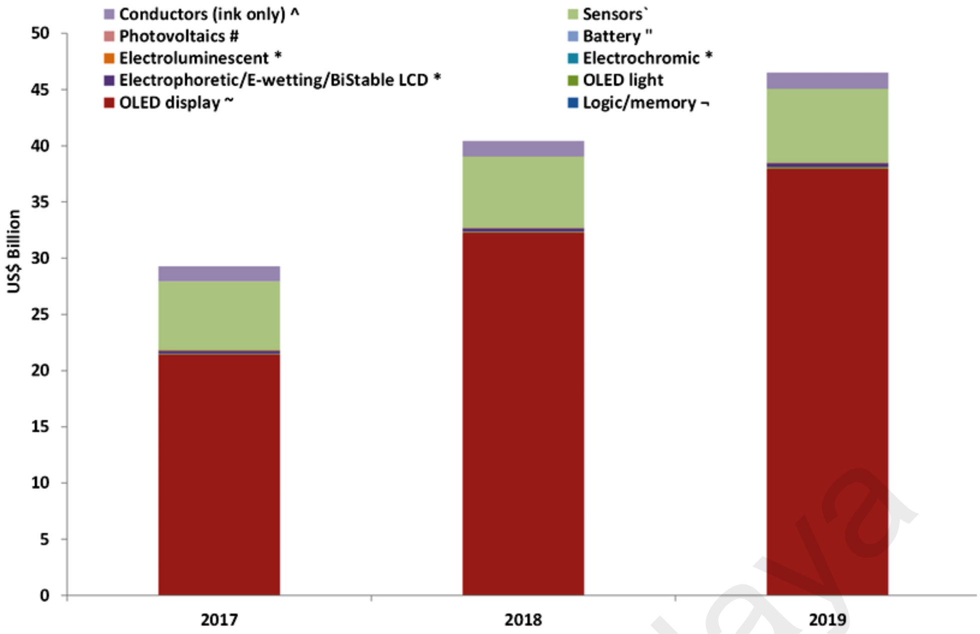

Figure 1.2: Partial market forecast by component type in US$ billion predicted by IDTechEx. (Das, 2017)

Organic and polymer-based solar cells are among the potential candidates for realisation of green optoelectronic devices as they can be printed on either a large-area flexible or a glass substrate for solar energy harvesting and electricity generation (Mazzio & Luscombe, 2015; Sekine et al., 2014). For instance, solar energy could be harvested by the OSCs when they are printed on the windows of a building or a small panel on a wearable device. Due to the huge investments and intense collaborations between governments, industrial partners and researchers, the power conversion efficiency of polymer based solar cells has significantly increased from roughly 2% in 2010 to slightly beyond 8% in 2015 as depicted in Figure 1.3 (Benten et al., 2016). These solar cells are fabricated using conjugated polymers which act as the electron donor and acceptor and also enhance the flexibility and mechanical properties of the device as compared to that of the solar cell based on polymer-fullerene blend.

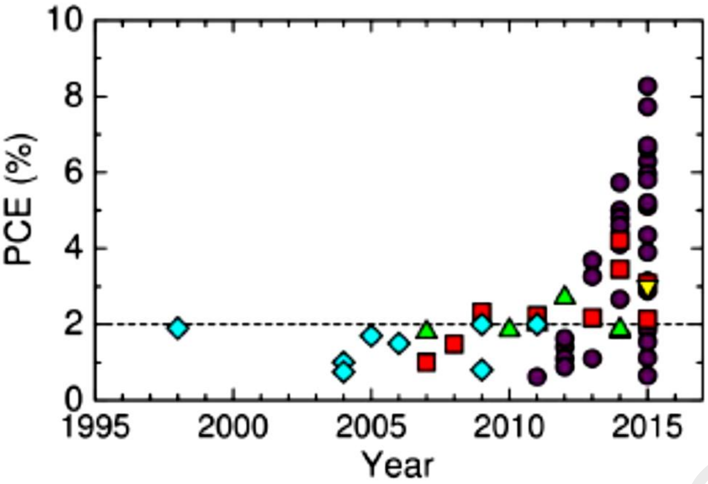

Figure 1.3: Progress on efficiency of polymer-polymer based solar cell. (Benten et al., 2016)

OFET plays a significant role as the building block for the development of low-cost, flexible and stretchable analogue and digital electronics circuits which could consist of logic gates, memory, sensors as well as microprocessors. The development of field-effect transistors based on organic semiconductors and polymer materials has began in the 1980's (Assadi et al., 1988; Ebisawa et al., 1983; Mori, 2008; Tsumura et al., 1986). Unfortunately, the reported mobility is relatively low, ranging from 10^{-5} to 10^{-4} cm^2/Vs and restricted its use in high speed electronic applications. However, owing to enormous choices of materials and synthesis techniques, researchers were able to engineer materials for organic semiconductor and polymer FETs, leading to significant improvements in mobility over the last three decades. The magnitude of charge carrier mobility has raised in several orders of magnitude from 10^{-5} cm^2/Vs to 40 cm^2/Vs, as shown in Figure 1.4, for FETs fabricated using conjugated polymer, small-molecule organic semiconductor thin film to single crystalline organic semiconductor (Chen et al., 2012; Hasegawa & Takeya, 2009; Minemawari et al., 2011).

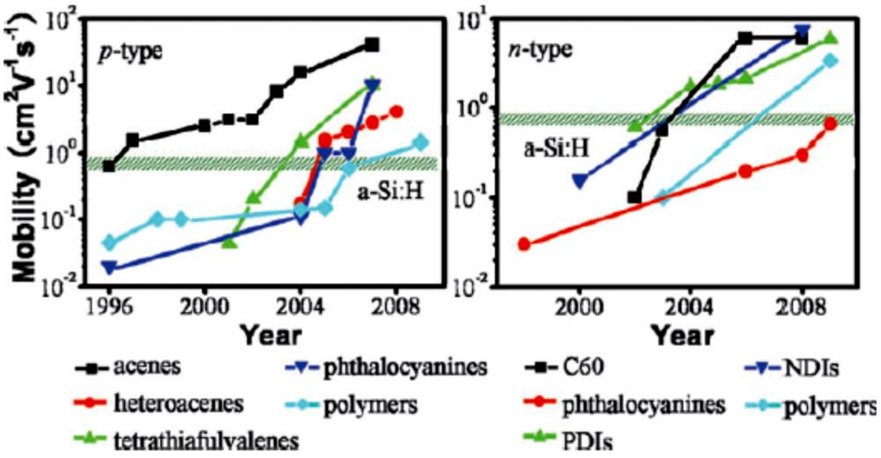

Figure 1.4: Progress in mobility improvement for *p*-type and *n*-type OFETs. (Dong et al., 2010)

An example of the application of organic transistors is realised in the fabrication of 8-bit, 40 instructions per second, flexible microprocessors as shown in Figure 1.5. The leftmost foil consists of two microprocessors and the rightmost foil consists of a microprocessor with two instruction foils. The size of one microprocessor is 2 × 1.7 cm^2 and it consists of 3381 pentacene transistors with width of 5 μm and mobility of 0.15 cm^2/Vs. Besides the technological importance of OFET, it is also utilised to study the fundamental physics of transport dynamics of charge carrier, surface, interface and light emission properties of organic semiconductor and polymer materials (Shirota & Kageyama, 2007).

Since charge carrier transport in organic semiconductors and polymer materials depend very much on the intermolecular hopping via π-conjugates, thus fabrication of single crystal to achieve higher molecular order and reduction in π-stacking distance have become a promising trend to improve mobility, defect reduction and noises of the material. As the material performance is gradually improving, a smart, biodegradable, biocompatible, environmental friendly and sustainable system which features with solar-powered, embedded microprocessors, memory, sensors and display units as illustrated in Figure 1.1 could be realised in the future.

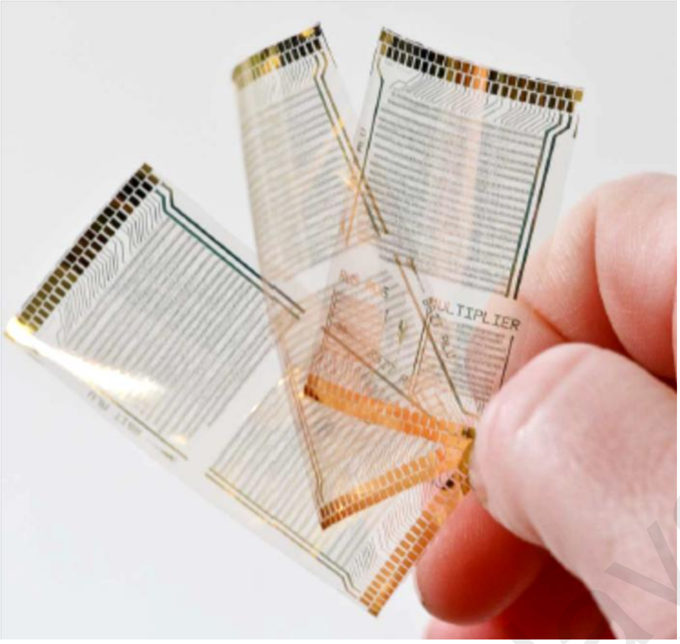

Figure 1.5: 8-bit, 6 Hz plastic microprocessor made of 3381 pentacene transistors fabricated on a plastic foil. (Myny et al., 2012)

1.2 Motivation and Objectives

Disorderness in organic semiconductor and polymer causes low mobility and fluctuation in number of charge carriers which lead to low speed, low bandwidth, high noise floor and low signal-to-noise ratio. These unwanted effects eventually degrade the device performance and limit its applications. Disordered properties in organic semiconductor and polymer may also be reflected in current noise spectra as it has a tendency to deviate from the typical 1/*f* noise characteristics and led to anomalous charge transport with long-current tail. It has been known that the multi-scaling current noise and anomalous transport behaviour are inadequately described by the conventional 1/*f* type spectral interpretation and Fick's diffusion law, respectively. On the other hand, it has been demonstrated that fractal analysis is useful for analysing nonstationary signal and it is rather tempting to explore its application in studying scaling behaviour of current noise in OFET. Likewise, fractional calculus has found many applications in the modelling of complex phenomena with nonlocal effects, namely long memory and long range dependence. Almost every dynamical equation known in the fields of physical science have been reformulated using fractional differential/integral operators. Thus, it is once again obvious to generalise the Fick's diffusion equation to the fractional drift-diffusion equation to model the anomalous transport dynamics in disordered material. While the theoretical formulations are robust and intuitive, analytical solution to time-fractional drift-diffusion equation is not always possible in most general cases. One has ultimately resort to numerical solutions with efficient algorithms that could handle and optimise non-local differential operators. In this study, the focus will also be on the understanding of the origins of the scaling behaviours of current noise in OFETs, the causes of long-tail transient currents and the suitability of fractional drift-diffusion equation for modelling of charge carrier transport in disordered organic semiconductors. Therefore the objectives of this study are:

1. to analyse the scaling behaviours of current noise in P3HT OFET using fractal noise theory.
2. to relate the scaling behaviours of current noise to the charge carriers transport mechanisms through the spectra and scaling exponents.
3. to study the anomalous charge carriers transport dynamics in disordered organic semiconductors at different fields and light intensities.
4. to develop a phenomenological model which is capable of describing the normal and anomalous charge carrier transports based on fractional differential equation.

1.3 Organisation of thesis

Chapter 1 provides a brief overview and challenges on organic electronics that are relevant to the present work, especially in defining the motivation and the objectives of this study. Literature review is provided in Chapter 2. Brief description on the background theory is included here to lead the reader to the related concepts and tools required in this work. An overview about organic semiconductors and polymers, operations and noises in the field-effect transistors, fractal modelling of signals, surfaces and transport dynamics are given in this chapter. Several normal and anomalous transport theories are presented in this chapter. Chapter 2 also introduces the fractional calculus theory, which serves as the mathematical framework for the derivation of anomalous transport model for disordered material. The fabrication and characterisation of OFET, low-frequency noise measurement and fractal analysis techniques are demonstrated in the first half of Chapter 3. The second part of this chapter continues with the derivation of the anomalous transport equation incorporated with multiple-trapping using fractional calculus, the numerical methods required to solve the fractional drift-diffusion equation and ends with the simulation procedures. Chapter 4 begins with a summary of the measurement conditions of P3HT OFET and then followed by the discussion on the scaling behaviours of current noise subjected to the presence of trap centres at different applied source-drain voltage. The simulation conditions for modelling the charge transport in RR-P3HT and RRa-P3HT materials are given in the beginning of Chapter 5 and then ended with the discussions on the transport dynamics of RRa-P3HT at various applied bias and RR-P3HT at different light intensity levels. Conclusions of this work, recommendations and suggestions for future work are reported in Chapter 6.

CHAPTER 2: LITERATURE REVIEW AND BACKGROUND THEORY

Chapter 2 begins with a brief overview on the development of materials for plastic electronics, followed by the operation, performance limiting factors and charge transport theory of OFETs. Description on the fractal theory is given because it serves as the fundamental concept for current noise analysis. Several charge transport theories based on normal diffusion process are presented because they are commonly used to model charge transport in crystalline material. Besides, these models can be generalised to describe the anomalous charge transport in disordered materials using fractional calculus. Lastly, the details of the anomalous transport models are given in the last section of this chapter.

2.1 Materials for organic electronics

Organic semiconductors and polymers used for the fabrication of plastic electronics could be classified into conjugated polymers, hybrid organic-inorganic structures, molecular semiconductors, small molecule semiconductors and single crystal structure polymers. Transistors which are fabricated using the latter two structures have demonstrated high mobility values exceeding the mobility of amorphous silicon and is comparable to the mobility of polysilicon.

Pentacene is one of the important polymers that has been extensively studied and used in the fabrication of OFET. This is simply due to the mobility of pentacene is matching up to the mobility of amorphous semiconductors. Günther and co-workers had demonstrated that the mobility of pentacene OFET could achieve a value up to 0.45 cm^2/Vs (Günther et al., 2015). They also found out that the mobility of the pentacene OFET would be reduced when the deposition rate is increased. This is because a larger amount of grain boundaries is induced in the channel region and hinders the movement of charge carriers leaving the device. Dong and co-workers (Dong et al., 2016) utilised a very thin single crystal pentacene OFET as shown in Figure 2.1 to achieve the highest mobility of 5.7 cm^2/Vs among pentacene OFETs. The thin layer of single crystal pentacene was grown from a seed crystal directly on a bare silicone dioxide substrate using the physical vapour transport method. Thus, pentacene molecules were aligned themselves orderly to form a monolayer crystal on the SiO_2 substrate. This significantly enhanced the diffusion of charge carries in the single crystal structure and yielded very high mobility.

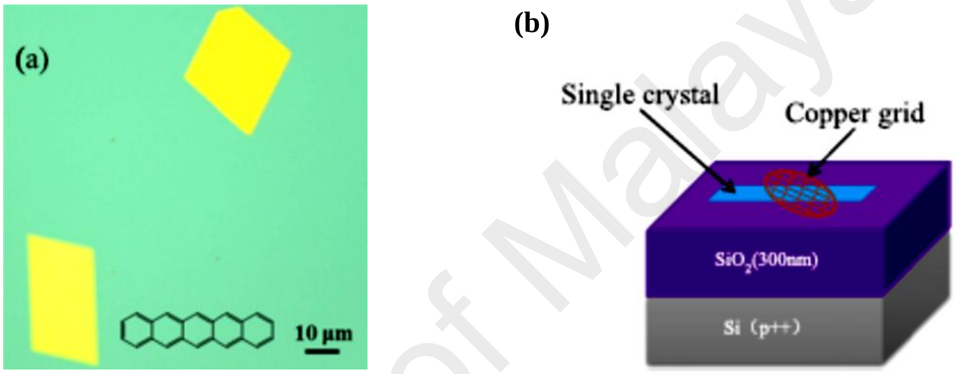

Figure 2.1: (a) Very thin pentacene single crystals deposited on a SiO_2/Si substrate, (b) Copper grid is used as mask to complete fabrication of the OFETs. (Dong et al., 2016)

Besides pentacene, poly(3-hexylthiophene) is also one of the extensively studied semiconducting conjugated polymers for electronic and optoelectronic applications due to its exceptional properties such as high mobility, solution-based processability and thermal properties (Bhatt et al., 2014; Dang et al., 2011). It has been demonstrated that the performance of P3HT polymer is greatly influenced by its backbone couplings which result in various types of regioisomers and the molecular weight. Regioregular P3HT is produced if the entire polymer consists of only the monomers with head-to-tail coupling configuration and less structural defects. On the other hand, regiorandom P3HT could have the various types of coupling configurations (Loewe et al., 1999; Terje & Reynolds, 2006) and Figure 2.2 shows some of the P3HT di-block copolymers.

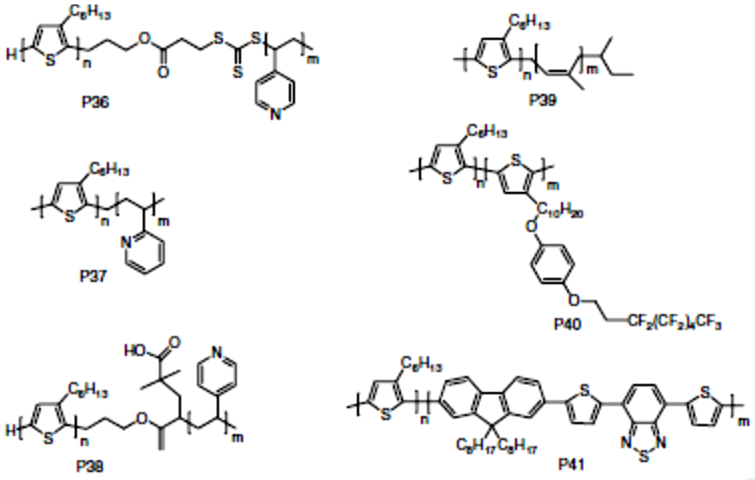

Figure 2.2: Examples of P3HT di-block copolymers. (Bhatt et al., 2014)

It had been shown that RR-P3HT has higher mobility than the mobility of RRa-P3HT (Mauer et al., 2010). The high mobility achieved for P3HT is 0.4 cm^2/Vs which was measured from the RR-P3HT FETs (Baeg et al., 2010). Although the mobility demonstrated so far for P3HT OFET has significantly improved, but it is still not suitable for high-speed device applications which are made from semiconductor materials. Recently, Nawaz and co-workers reported the highest mobility of 1.2 cm^2/Vs which was measured from the defect free regioregular poly(3-hexylthiophene-2,5-diyl) OFET (Nawaz et al., 2016). Besides, mobility ranging from 2 to 8.2 cm^2/Vs produced from PDVT-based OFET has been reported (Chen et al., 2012). The reduction in the distance between the π-stacking has tremendously improved the mobility of the P3HT-based OFET from 10^{-5} cm^2/Vs to 8 cm^2/Vs.

Single crystal structure polymers have been extensively studied in recent years due to its high-order alignment of molecules and high mobility. Figure 2.3 shows a crystal structure and molecular arrangement of the single crystal C_n-BTBT derivatives which were produced by using the Friedel-Crafts acylation and Wolff-Kishner reduction techniques with BTBT serving as the starting material. The mobility of the BTBT derivatives was reported to be ranging from 0.16 to 2.75 cm^2/Vs for $5 \leq n \leq 14$ (Ebata et al., 2007). Later on, Minemawari and co-workers successfully synthesised the single crystals of C_8-BTBT organic semiconductor by using the combination of anti-solvent crystallisation and inkjet printing techniques. They then fabricated C_8-BTBT TFTs which produced highest average mobility of 16.4 cm^2/Vs due to the high crystallinity of the C_8-BTBT structure (Minemawari et al., 2011). The mobility value of the C_8-BTBT is also comparable and higher than the mobility of the amorphous semiconductor (μ = 0.5 to 1 cm^2/Vs). It had been reported that single-crystal rubrene OFET fabricated using the crystal lamination technique was able to achieve a high mobility value up to 30 cm^2/Vs (Kalb et al., 2007) and other high performance single crystal materials for OFETs are also reported in (Hasegawa & Takeya, 2009). Hence, the developments of the anti-solvent crystallisation and inkjet printing techniques have realised the fabrication of high performance single crystal organic semiconductors and large-area, flexible optoelectronic and electronic devices. Besides, it had also been demonstrated that top-contact, bottom-gate TFTs fabricated using small-molecule C_{10}-DNTT organic semiconductor achieved a high mobility value up to 8.5 cm^2/Vs. C_{10}-DNTT was deposited using the vacuum deposition technique for a thickness of 10 nm while maintaining the temperature of the substrate at 80 °C. The mobility of the C_{10}-DNTT TFTs would be reduced to 2.8 cm^2/Vs if the deposition is carried out by solution shearing technique and further reduced to 1.3 cm^2/Vs if the channel region is oriented perpendicular to the shearing direction (Hofmockel et al., 2013).

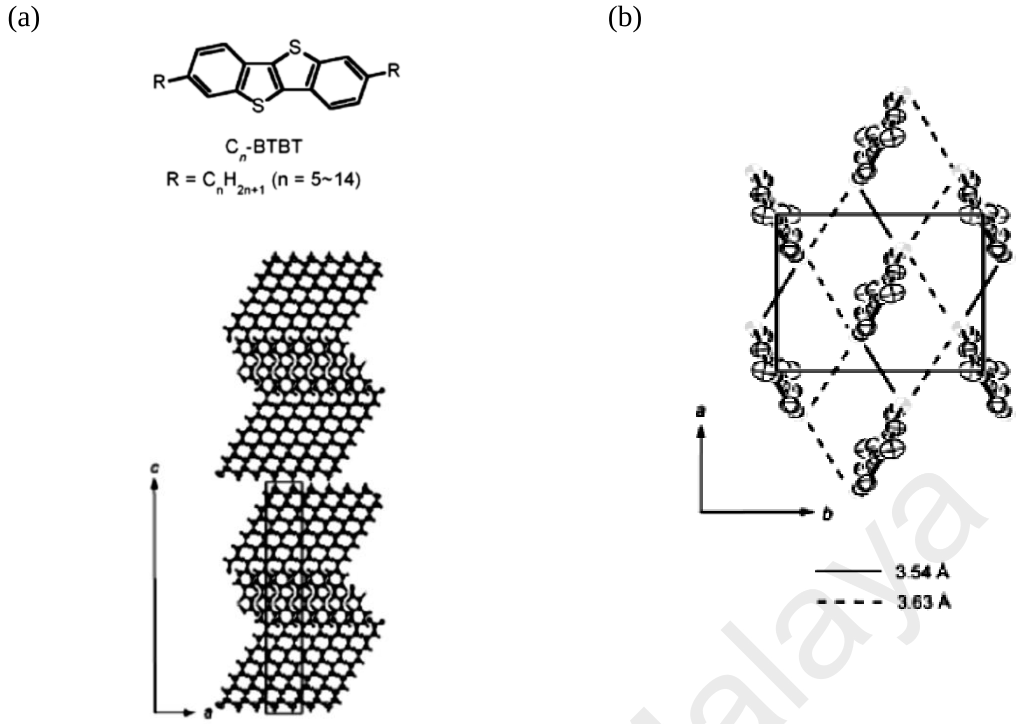

Figure 2.3: (a) Structure and (b) molecular arrangement of C_n-BTBT. (Ebata et al., 2007)

On top of the efforts spent on the development of *p*-type OFET, there are also some works dedicated to the development of *n*-type and ambipolar OFET as they are also important constituents of making complementary transistors, circuits, solar cells and light-emitting diodes (Choi et al., 2015; Zhao et al., 2013). Schmidt and co-workers had demonstrated that *n*-type OTFT based on halogenated PBI dyes deposited on SiO_2 gate treated with *n*-OTS could achieve electron mobility greater than 0.5 cm^2/Vs, which is comparable to the mobility of *p*-type OFETs and amorphous semiconductors FETs (Schmidt et al., 2009). This is because the PBI π-stacking with very small interplanar distance results in highly dense and parallel arrangement of molecules that leads to the high electron mobility. The highest electron mobility of 6 cm^2/Vs was demonstrated by the *n*-type OTFT made of *N*,*N′*-bis(cyclohexyl) naphthalene-1,4,5,8-bis(dicarboximide) and its structure is shown in Figure 2.4. The high mobility is achieved because the cyclohexyl end groups of the NDI helps in optimising the crystalline structure packing through the intermolecular stacking (Shukla et al., 2008).

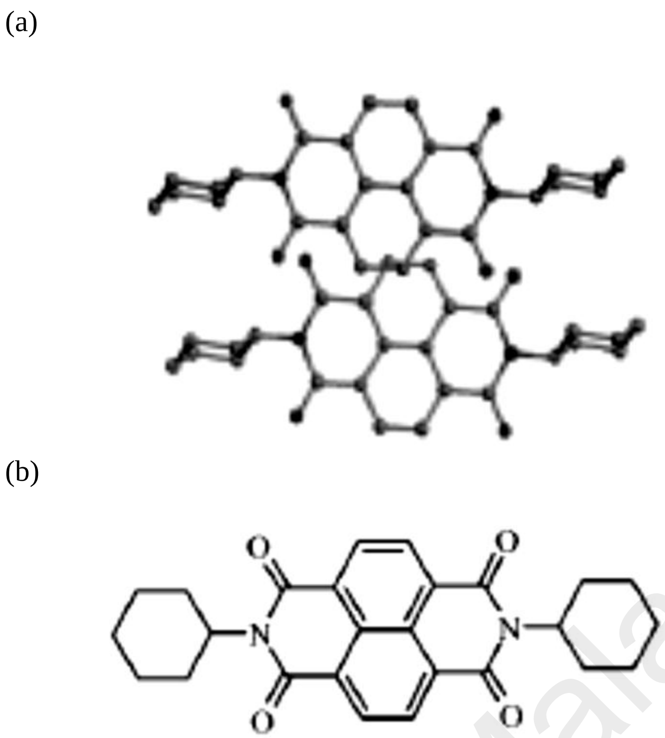

Figure 2.4: (a) Molecular and (b) single structure of N,N′-bis(cyclohexyl)naphthalene diimide. (Shukla et al., 2008)

2.2 Operation of field-effect transistor

Figure 2.5 shows the top-contact and bottom-contact configurations of an OFET. Basically, a field-effect transistor consists of an organic or inorganic semiconducting active layer which is separated from the gate electrode by a layer of dielectric; source and drain electrodes are separated by a channel length L and in contact with the semiconducting layer. The source electrode is usually kept at zero bias and meant for charge carrier injection. When the gate voltage V_g (potential difference between the source and gate electrodes) is biased at a more positive (negative) level than that of the source voltage V_s, electrons (holes) are injected into the semiconducting layer within the channel region. The amount of accumulated charges is proportional to the gate voltage V_g and the capacitance per unit area C_i of the dielectric. Before these charge carriers are moving to the drain electrode and then giving rise to current, the deep trap centres at the interface between the semiconducting and dielectric layers in the channel region have to be filled by these charge carriers first. Thus, there is an extra voltage, namely the threshold voltage V_{th}, required to compensate this effect and the effective gate voltage is given as $V_g - V_{th}$ before current is resulted.

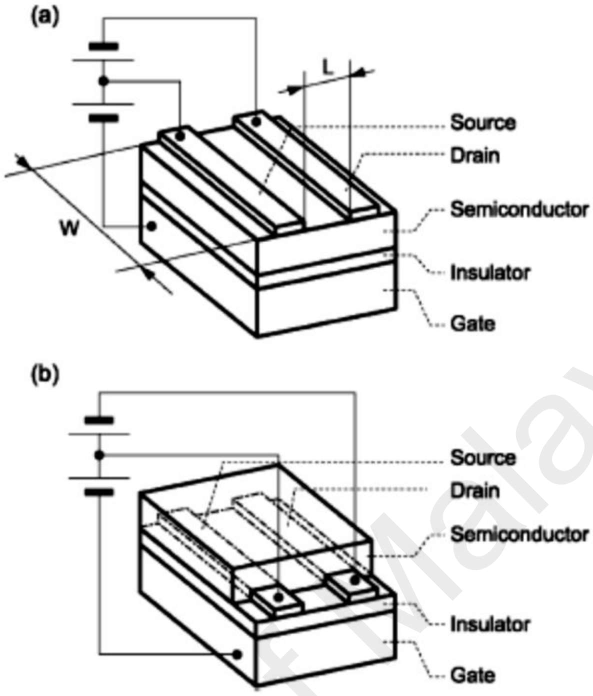

Figure 2.5: (a) Top-contact and (b) bottom-contact configurations of OFET. (Shirota & Kageyama, 2007)

When a small source-drain voltage V_{ds} (potential difference between the source and the drain electrodes) is applied, charge carriers could flow through the channel region and be extracted from the drain electrode. The resulted source-drain current I_{ds} is linearly proportional to the V_{ds} and it is given by (Shirota & Kageyama, 2007),

$$I_{ds} = \frac{\mu W C_i}{L}\left(V_g - V_{th}\right)V_{ds}, \tag{2.1}$$

where W is the width of the channel region. The characteristic of I_{ds} in the linear region is depicted on the L.H.S. of the dashed-line in Figure 2.6. If the V_{ds} is increased until $V_{ds} = V_g - V_{th}$, the FET is now at its pinch-off condition where a small depletion region is formed next to the drain electrode. Since the electric field in the depletion region is relatively higher than the electric field at the pinch-off point, thus space-charge saturation current is resulted when the charge carriers near the pinch-off point are swept across the depletion region into the drain electrode. If V_{ds} is continually increased, the depletion region will be expanded and leads to the shortening of the channel length. However, the potential at the pinch-off point is still unchanged ($V_g - V_{th}$) and the same for the potential that drops between the pinch-off point and the source electrode. Thus, the resulted current saturates after the pinch-off condition is achieved. The I_{ds} resulted from the transistor at saturation condition is given by

$$I_{ds} = \frac{\mu W C_i}{2L}\left(V_g - V_{th}\right)^2 . \tag{2.2}$$

The characteristic of I_{ds} in the saturation region is depicted on the R.H.S. of the dashed-line in Figure 2.6. The saturation current could be increased by increasing gate voltage.

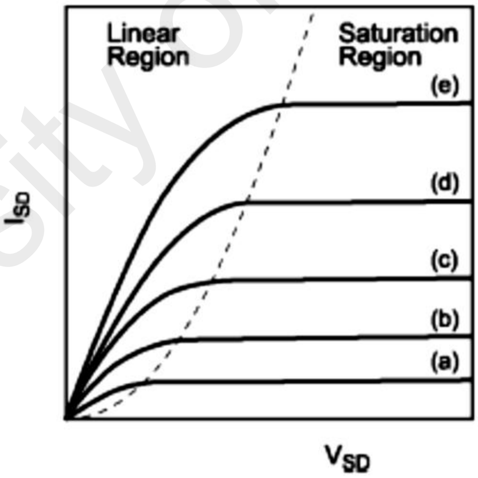

Figure 2.6: Current-voltage characteristic of an OFET for increasing V_g from (a) to (e). (Shirota & Kageyama, 2007)

2.3 Performance limiting factors of transistors

Low mobility and noise could be the most significant factors which could undermine the optimal performance of an OFET, thus a brief description on these factors and the methods used to characterise them are provided in this section.

2.3.1 Noises in organic field-effect transistor

Current noise could be simply described as the random fluctuation in the current produced from a device such as field-effect transistor. High current noise will yield a low S/N ratio value which could set a limit on the performance of the device and hence restrict the application of the device as an electronic switch, amplifier or logic device. Commonly, the noise characteristics of a transistor could be studied through their LFN power spectra. This approach has been proven to be useful for probing the transport dynamics at microscopic level, bulk or interface defects and trap density information as demonstrated in several published works (Johanson et al., 2002; Jurchescu et al., 2008; Ke et al., 2008; Pénarier et al., 2002). This is because current-voltage measurement can only represent the macroscopic behaviour of the devices; it is not so useful for studying defects and trap centres related dynamics that are present in the devices. The gate voltage dependence of mobility obtained by using time-of-flight (TOF) measurement can be used as a device parameter to probe the information of the structural imperfection and impurities (Tanase et al., 2003). However, high precision TOF measurement requires an expensive and intricate setup thus hampers its affordability.

Figure 2.7 shows the normalised noise power spectra of undoped amorphous silicon at different temperatures reported by Johanson and co-workers. They concluded that the slopes β of the noise power spectra at low-frequency depended very weakly on temperature with slope values only slightly rising from 1.15 to 1.3 when temperature was increased whereas the β at high frequency did not depend on temperature with value of 0.6 (Johanson et al., 2002). They also found the noise power spectra only depended very weakly on doping. Later on, they reported that the generation-recombination noise is associated with shallow trap levels occurring in the device and $1/f$ noise is believed to be caused by a large number of generation-recombination trap centres that produces a cumulative generation-recombination noise (Kasap & Capper, 2006).

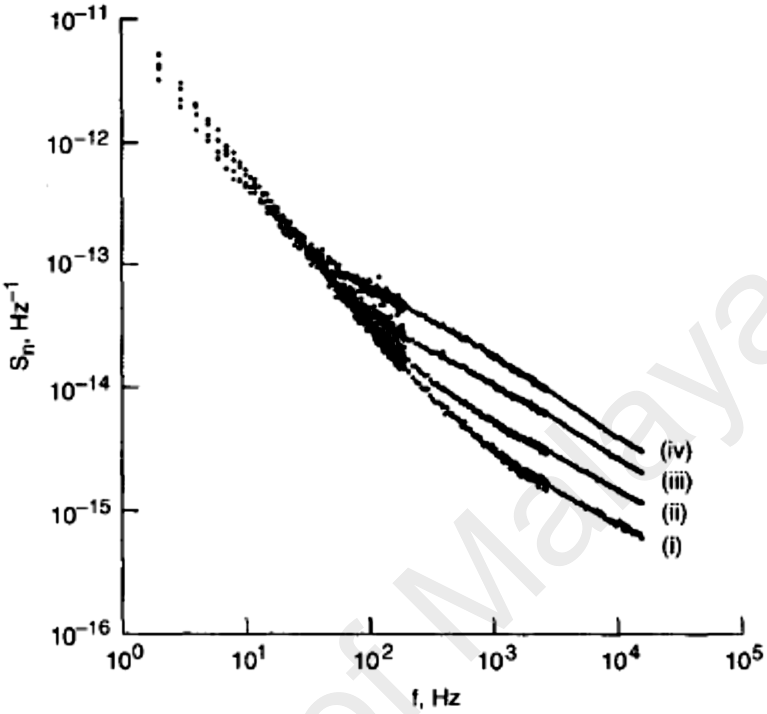

Figure 2.7: Normalised noise power spectra of undoped amorphous silicon at four temperature (i) 495 K, (ii) 483 K, 467 K and (iv) 454 K. (Johanson et al., 2002)

Figure 2.8 shows the noise power spectra for various III-V semiconductor HBT with emitter areas of the same order of magnitude which were measured at the same base bias current (Pénarier et al., 2002). It could be noticed that the 1/*f* and Lorentzian-type noises are presented in the noise power spectra of AlGaAs/GaAs and GaInP/GaAs HBTs but Lorentzian-type noise is less apparent for the GaInP/GaAs HBTs. The noise power spectra for InP/InGaAs HBTs are only made up by the 1/*f* and white noises. White noise is frequency independent and given by $2eI_b$ where I_b is the base current. The Lorentzian-type noise is induced by the generation-recombination of charge carrier from trap centres which are located near the emitted-base interface. The 1/*f* noise could be produced by the recombination of charge carries at the surface or space charge region.

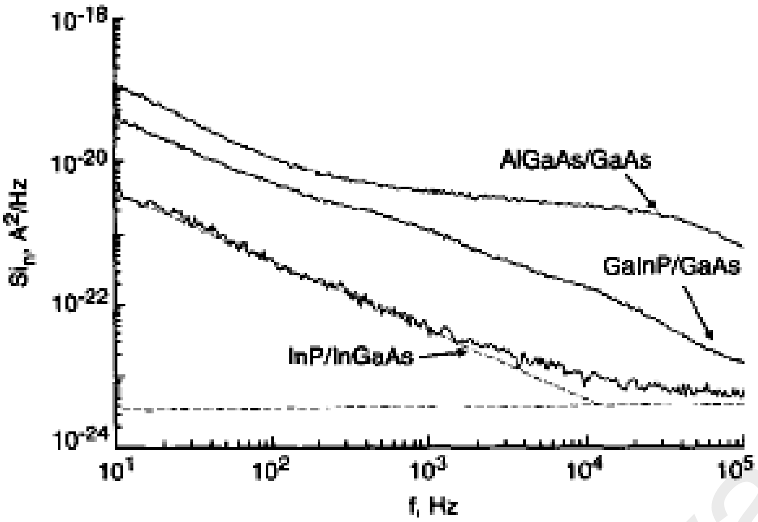

Figure 2.8: Noise power spectra for various III-V semiconductor heterojunction bipolar transistors. (Pénarier et al., 2002)

Figure 2.9 shows the low-frequency noise power spectra density for HMDS treated RR-P3HT OFET for various channel lengths. It could be seen that the noise level increases with the channel length of the OFET. Lorentzian-type of noise is observed at low frequency which is induced by generation and recombination of charge carries by a small amount of trap centres. The noise power spectra density is also found to deviate from the 1/*f* noise behaviour. The 1/*f* noise is believed to be caused by the fluctuation in the number of charge carriers which is induced by the generation and recombination or charge carriers at the grain boundaries (Ke et al., 2008). Since the 1/*f* noise is influenced by the grain boundaries, improvements on the quality of grain boundaries through the fabrication processes will reduced the 1/*f* noise.

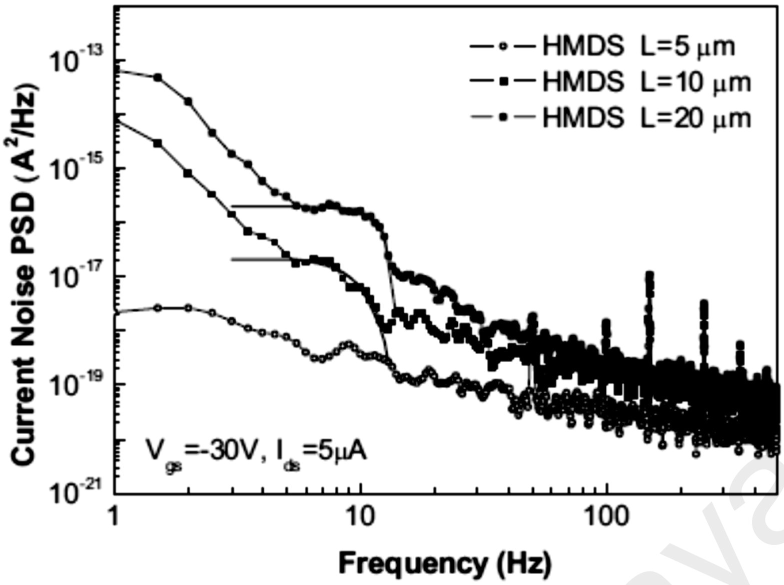

Figure 2.9: Low-frequency noise power spectra density for HMDS treated RR-P3HT OFET. (Ke et al., 2008)

In brief, the fluctuation in output current of a transistor could be due to the (i) random variation in the number of charge carriers leaving the device, (ii) random generation and recombination of charge carriers while drifting across the active region or interface of the device, (iii) variation in the mobility of charge carriers and (iv) material disorders. Besides, it is obvious that the noise power spectra could deviate from the 1/*f* noise behaviour and presents certain degree of power-law scaling behaviour as evidenced from the noise power spectra that are measured from the transistors made of amorphous silicon (amorphous structure), III-V semiconductor (crystalline structure) and P3HT (disordered structure) materials.

It is reckoned that accurate characterisation of the low-frequency noise can serve as a simple but powerful transport dynamics, device fabrication and performance diagnosis tool. Most of the conventional noise analysis methods are developed based on the PSD method which is calculated from the Fourier transform and only works well with stationary noise. However, noise often contains nonstationary components and power-law scaling behaviour as reported in (Brophy, 1968, 1969; Huo et al., 2003; Johanson et al., 2002; Ke et al., 2008; Nelkin & Harrison, 1982; Pénarier et al., 2002). The notion of nonstationarity refers to time-dependence of the basic statistics such as mean and variance of the time series, and hence requires time evolutionary PSD (such as time-frequency distribution). For example, the presence of trends or dynamical changes in the time series would render a simple PSD method to be inaccurate. A common practice would be to perform windowed Fourier transform or to perform the Fourier spectrum analysis on non-contagious segments of the time series and to take ensemble average of the power spectrum. This is done under presumption that the segments of the time series are approximately stationary.

A more robust technique like the DFA, which can handle both stationary and nonstationary fractal time series, would provide better estimation of the scaling exponents present in the multiple regions of the times series. The utilisation of DFA on the analysis of multiscaling noise resulted from semiconductor circuits and devices has been demonstrated (da Silva Jr. et al., 2005; Shiau, 2011; Silva et al., 2009). Since the current noise of OFET presented some scaling property similar to the current noise of amorphous or III-V semiconductor transistors, it is believed that the DFA method would be a potential method which could be used to study the current noise of the OFET.

2.3.2 Dispersive current and low mobility

Mobility is one of the important figure-of-merits that determines the speed and bandwidth of electronic devices especially transistors. Accurate mobility measurement is crucial to provide the real performance of the device. Thus, many methods have been established for mobility measurement. Some of these methods are the TOF measurement (Tiwari & Greenham, 2009), CELIV (Juška et al., 2000; Pivrikas et al., 2005) and SHG spectroscopy (Iwamoto et al., 2003; Manaka et al., 2005, 2006).

Figure 2.10(a) and Figure 2.10(b) show typical non-dispersive and dispersive transient photocurrents measured by the TOF measurement. The inset in Figure 2.10(b) is the double-log plot of the transient photocurrent. The non-dispersive transient current takes a step-like or nearly square pulse shape as shown in Figure 2.10(a). The step-like pulse shape demonstrates that most of the charge carriers exceed the device at nearly the same time. Thus, mobility of the non-dispersive transport is inversely proportional to the transit time t_{tr} (the time when charge carriers are leaving the device as indicated by τ in Figure 2.10).

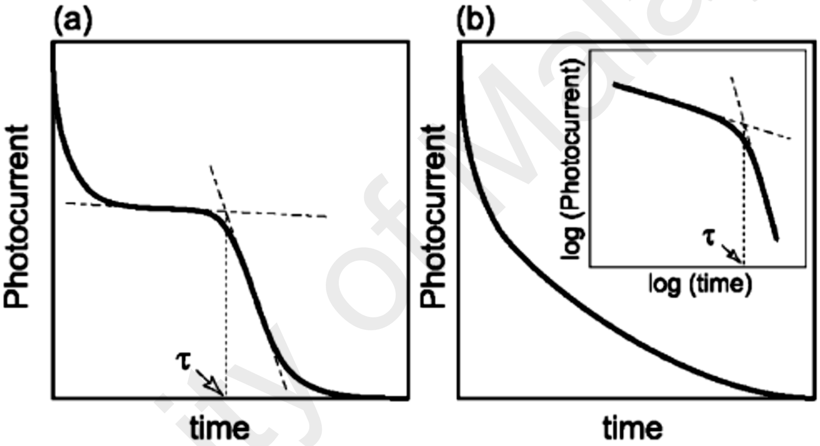

Figure 2.10: (a) Non-dispersive and (b) dispersive transient photocurrents. (Shirota & Kageyama, 2007)

The mean squared displacement of charge carriers in normal diffusion is also linearly proportional to time. Thus, the propagation of charge carriers could be modelled by the Fick's diffusion law which is derived based on the law of conservation of mass (Fick, 1855). Besides, several mathematical frameworks had been demonstrated in modelling the normal diffusion in which these models are generally classified into (i) probabilistic models based on the random walk (Einstein, 1905) and central limit theorem and (ii) stochastic models based on the Brownian motion (Chandrasekhar, 1943), master equation, Langevin equation and Fokker-Planck equation (Coffey et al., 2004; Fokker, 1914; Risken & Frank, 1996).

In contrast, the dispersive transient current, as shown in Figure 2.10(b), possesses a long-tail shape after the initial spike and does not have a plateau region as compared to that of the normal transient current. The transient current could be described by an asymptotic power-law form. The presence of long-tail transient current implies the occurrence of pulse broadening of charge carriers when they are propagating across the device and yields low mobility which limits the performance of the device. The transport dynamic of charge carrier is associated to the hopping-trapping mechanism in localised states instead of charge transport in the conduction band as in the case of semiconductor materials. Hence, charge transport in disordered material deviates from the normal diffusion process which causes the MSD of charge carriers is proportional to the power-law in time.

Figure 2.11 shows the schematic diagram of a SHG system that is used to analyse the channel formation and electric field distribution in the channel region of OFET (Manaka et al., 2005, 2006) and it was originally developed to study the polarisation of amphiphilic monolayer (Iwamoto et al., 2003). This method uses an infrared light which does not cause photo-carrier generation in the channel region and there is no charge injection from the contacts in the off-state condition, thus the channel formation is associated to the destruction of SHG signal which is induced by the second-order nonlinear polarisation of the organic material. The mobility is then indirectly deduced from the variation in the distribution of electric field (due to change in SHG signal) which is related to the space differential of the potential according to

$$J = e\mu n_c(V)\frac{dV}{dx}, \tag{2.3}$$

where e is the electronic charge, μ is the mobility, $n_c(V)$ is the charge carrier density that depends on the electric potential V. Besides, the properties of organic material and its device operation could be studied.

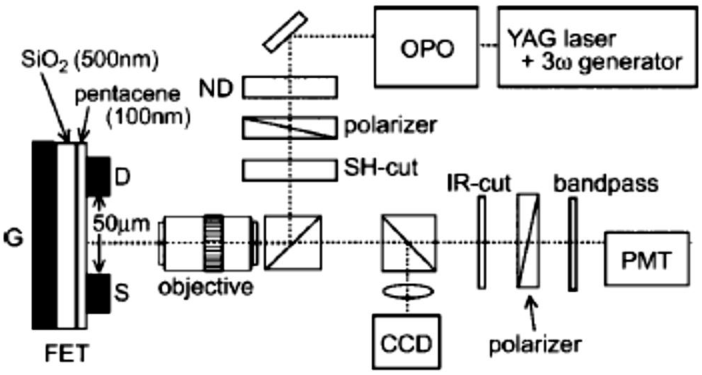

Figure 2.11: Schematic diagram for SHG measurement. (Manaka et al., 2006)

Charge extraction by linearly increasing voltage method has become a popular method for mobility measurement of disordered organic semiconductors or polymer (Mozer et al., 2005; Pivrikas et al., 2005). The applied bias at one of the terminals is linearly increased and then the mobility is deduced from measured transient current using the following formulae,

$$\mu = \frac{2}{3R_V}\left(\frac{L}{t_{\max}}\right)^2, \tag{2.4}$$

for low conductivity sample ($\tau_{de} \gg t_{tr}$) and

$$\mu = \frac{\tau_{de}}{R_V}\frac{L^2}{t_{\max}^3}, \tag{2.5}$$

for high conductivity sample ($\tau_{de} \ll t_{tr}$), where τ_{de} is the dielectric relaxation time, t_{tr} is the transit time, $t_{\max}$ is the peak current time, L is the device length, μ is the mobility and R_V is the voltage rise speed. The measurement can be carried out by using thinner device length as compared to that of the TOF measurement because there is no light absorption involved during the measurement thus electrode does not need to be transparent. This method provides direct mobility measurement and also suitable to be used to measure mobility of solar cells or LEDs at reverse biased condition.

Unfortunately, the mobility for hole and electron of an ambipolar device could not be distinguished and the charge species with lower mobility will determine the mobility of the device. This method also requires sufficient amount of charge carriers to be present in the device for measurable output current. This drawback could be improved by increasing the amount of charge carriers via doping or light illumination (it is called as Photo-CELIV (Mozer et al., 2005)). The mobility measurable range depends on the sample geometry and applied bias range. The extraction time and peak current levels are proportional to the applied bias ramp speed, which determine the lowest measurable mobility of the device down to range of 10^{-5}–10^{-6} cm^2/Vs. In contrast, the upper limit of the measurable mobility is determined by ratio of the peak current level and *RC* time constant. If the ratio is approaching unit, the output current is hard to be distinguished from the capacitive response.

2.4 Charge transport theories for OFET

Charge transport theory for disordered organic semiconductor or polymer materials is developed based on the charge transport theory for amorphous semiconductor. This means that conduction of charge carriers is due to the intermolecular hopping-trapping process between localised states that are subjected to the energy and positional disorders of the material. The hopping of a charge carrier from one place to another place in the device under the influence of an electric field is hypothetically represented by the line in the Figure 2.12(a). Along the hopping path, the charge carrier has undergone several hopping through different localised sites with different energy levels as depicted in Figure 2.12(b). By combining the hopping path in space and energy level, the hopping of charge transport in two-dimensional energy map is resulted and depicted in Figure 2.12(c). The surface energy is rough due to the material disorder.

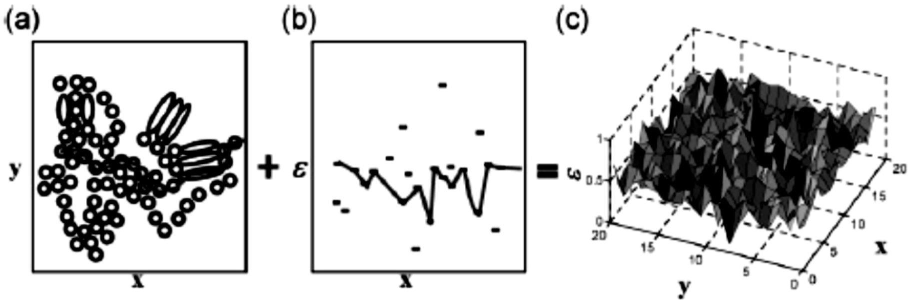

Figure 2.12: Schematic diagram showing the distribution of transport sites in (a) space, (b) energy and (c) two dimensional map of energy surface. (Tessler et al., 2009)

The presence of energy disorder is induced by the variation in molecular interaction energies that results in a broad energy density of states. The positional disorder is caused by the structural defects such as kinks and twists which are generated in the polymer chains during fabrication processes. These defects induce variation in the conjugation lengths and interaction energies. In view of the broad and steep energy distribution caused by the energy and positional disorder, charge carriers are expected to be hopping between the localised states that are located near to the transport energy level or mobility edge. Both exponential and Gaussian distributions are commonly used in the derivation of the energy DOS in disordered material.

The propagation of charge carrier could be described by a probability evolution equation, namely master equation, which is given by (Mott & Twose, 1961),

$$\frac{\partial Pt_i}{\partial t} = \sum_j \left[TR_{ij} Pt_i \left(1 - Pt_j\right) - TR_{ji} Pt_j \left(1 - Pt_i\right) \right] - \lambda_{ME-i} Pt_i \,, \tag{2.6}$$

where $j \neq i$, $Pt_i(t)$ is the probability that site i at location R_i and energy E_i is occupied by a charge carrier or excitation at time t, $1 - Pt_j(t)$ is the probability that site j is empty, TR_{ij} is the transition rate from site i to site j and $\lambda_{ME\text{-}i}$ is the decay rate of the excitation at site i. The hopping rate from one site to another empty site could be represented either by the Miller-Abrahams transition rate, Mott variable range hopping model, Marcus transition rate or Gaussian disorder model.

Miller-Abraham transition rate is derived based on the phonon tunnelling mechanism in semiconductor materials (Miller & Abrahams, 1960). The hopping of charge carriers is assumed to be near the Fermi level, empty sites are randomly distributed in energy and no polaron effect. The MATR is given by (Stafström, 2010; Tessler et al., 2009),

$$TR_{ij} = \omega_{pho} \exp\left(-\frac{2\left|R_{ij}\right|}{l_a} \right) \begin{cases} \exp\left(-\Delta E / k_B T\right) & \text{if } E_j > E_i \\ 1 & \text{if } E_j < E_i \end{cases}, \tag{2.7}$$

where ω_{pho} is the phonon vibration frequency or jump-escape rate, l_a is the localisation radius, $\Delta E = E_j - E_i$, E_i and E_j are the energy levels at site i and site j.

Mott variable range hopping model is also derived based on the phonon tunnelling mechanism incorporated with polaron effect for disordered material (Mott & Twose, 1961). The hopping of charge carriers could have happened through resonance and empty sites are randomly distributed in terms of energy and position. The transition rate is given by (Dunlap & Kenkre, 1993; Holstein, 1959),

$$TR_{ij} = \frac{{}^{MH}\Theta_{ij}^{2}}{\hbar} \sqrt{\frac{\pi}{2E_p k_B T}} \exp\left(-\frac{\Delta E}{2k_B T} - \frac{E_p}{2k_B T} - \frac{\left(\Delta E\right)^2}{8k_B T E_p} \right) \tag{2.8}$$

where E_p is the polaron binding energy, $E_a = E_p/2$ is the polaron activation energy and ${}^{MH}\Theta_{ij}$ is the transfer matrix element given by

$${}^{MH}\Theta_{ij} = {}^{MH}\Theta_0 \exp\left(-\frac{2\left|R_{ij}\right|}{l_a} \right), \tag{2.9}$$

and ${}^{MH}\Theta_0$ is calculated from the crossing point between the reactant (initial state) and product (final state) energy curves. Equation (2.9) is resulted by assuming that the electronic coupling between the two energy states decays exponentially with the distance between the two localised sites.

In the Marcus theory, the initial state, final state and ground state are represented by identical parabolic energy dispersive curve and shifted relative to each other based on the Gibbs free energy of the system. Transition of charge carrier occurs through the minimum energy at the intersecting of the potential surfaces of the initial and final states. The Marcus transition rate is given by (Likhtenshtein, 2012; Stafström, 2010),

$$TR_{ij} = \frac{2\pi \, {}^{MC}\Theta_{ij}^{2}}{\hbar\sqrt{4\pi E_{\lambda} k_B T}} \exp\left(-\frac{\left(\Delta G^0 + E_{\lambda}\right)^2}{4E_{\lambda} k_B T} \right), \tag{2.10}$$

where $E_{\lambda} = 4E_a$ is the reorganisation energy (energy needed for vertical charge carrier transfer without the ground state of the charge carrier is being refilled), ΔG is the Gibbs free energy between the initial and final states, and the ${}^{MC}\Theta_{ij}$ is the transfer matrix element given by

$${}^{MC}\Theta_{ij} = {}^{MC}\Theta_0 \exp\left(-\frac{\left|R_{ij}\right|}{l_a} \right), \tag{2.11}$$

or Equation (2.11) can be rewritten in terms of the polaron activation energy E_a as

$$TR_{ij} = \frac{{}^{MC}\Theta_{ij}^{2}}{\hbar} \sqrt{\frac{\pi}{4E_a k_B T}} \exp\left(-\frac{\left(\Delta G^0 + E_a\right)^2}{16E_a k_B T} \right). \tag{2.12}$$

Gaussian disorder model had been proposed by Bässler to model charge transport in disordered organic photoconductor (Bässler, 1993) and later on this model had been widely used in charge transport study of doped polymers and disordered materials (Borsenberger et al., 1993; Hartenstein et al., 1995). This model assumes that the energies of hopping sites for either electron or hole are subjected to a Gaussian distribution, thus the Gaussian DOS is given by,

$$\rho(E) = \frac{1}{\sqrt{2\pi\sigma_E^2}} \exp\left(-\frac{E^2}{2\sigma_E^2}\right), \tag{2.13}$$

where energy E is measured relative to the centre of the DOS. The relationship between the standard deviation σ_E of the Gaussian DOS and the reduced energy disorder parameter is given by

$$\hat{\sigma}_E = \frac{\sigma_E}{k_B T}, \tag{2.14}$$

and it is related to the dispersive parameter α in the time-fractional drift-diffusion equation (see Equation (3.8)) as $\alpha = 1/\hat{\sigma}$. The topological defects that occur in the polymer chain result in the space localisation of energy states and energies of neighbouring sites are uncorrelated. The motion of charge carriers is highly random and the hopping from site i to j is expressed by the MATR as given in Equation (2.7). Monte Carlo method is then used to simulate the charge carrier transport and the material disorder is implemented by (i) choosing the reduced energy disorder parameter from the Gaussian DOS in Equation (2.13), (ii) the distances between the intersites is randomly chosen from a uniform distribution and (iii) the intersite overlap or coupling parameter $\Gamma_c = 2a/l_a$ is taken from a Gaussian distribution, a is lattice constant and Γ_c is fixed at 10 as an experiment fitting parameter. The mobility is deduced from the average arrival time of charge carriers to exceed the device. It should be equal to the transit time of the plateau region of a non-dispersive current which is obtained from the TOF measurement. The diffusion coefficient is calculated from the variance of the charge carrier packet or the MSD as

$$D = \frac{\left\langle \left(x - \langle x \rangle \right)^2 \right\rangle}{2t}. \tag{2.15}$$

Besides the charge transport models presented in the preceding paragraphs, random walk and central limit theorem used in normal diffusion are respectively generalised to the continuous-time random walks and generalised central limit theorems for modelling of charge transport in disordered material (Metzler & Klafter, 2000a; Metzler et al., 1999; Scher & Montroll, 1975). Several works have attempted to unify both normal and anomalous transports in a single theoretical framework by means of the generalisation of normal transport equation using fractional calculus approach. The anomalous transport models based on fractional calculus have been demonstrated in various forms such as the fractional diffusion equation (Balakrishnan, 1985; Bisquert, 2005; Hilfer, 2000b; Schneider & Wyss, 1989; Wyss, 1986), fractional Fokker-Planck equation (Barkai, 2001; Barkai et al., 2000; Metzler et al., 1999), fractional drift-diffusion equations (Metzler & Klafter, 2004; Sibatov & Uchaikin, 2009), fractional Langevin equation (Bazzani et al., 2003; Lim & Muniandy, 2002; Lutz, 2001; Metzler & Klafter, 2000b), fractional Brownian motion (Mandelbrot & Van Ness, 1968) and fractional Klein-Kramer equation (Gajda & Magdziarz, 2011).

Barkai (2001) has developed a FFPE, which is compatible with the CTRW model that was developed by Scher and Montroll (1975), to describe the anomalous behaviour of the transient current of amorphous material. Since the probability density of the FFPE developed by Barkai (2001) is normalised, thus the total charge carriers are conserved and equivalent to the total charge carriers that are generated during the photo-absorption process, particularly valid for the case in TOF measurement. Besides, Hilfer had proposed a non-conserved version of the FDE based on the RL fractional derivative to study anomalous diffusion by replacing the integer order time derivative of the standard diffusion equation with a fractional order time derivative (Hilfer, 2000b). It was also suggested that the fractional time derivative with order ranges from 0 to 1 may be interpreted as infinitesimal generator of time evolution of free charge carriers in disordered media. Bisquert (2005) had proved that the non-conserved FDE reported in (Hilfer, 2000b) is capable of providing physical insight of the anomalous diffusion of free charge carriers in disordered material with dissipation process such as trapping or recombination mechanism. Sibatov and Uchaikin (2009) has also demonstrated various versions of conserved TFDDE, incorporated with multiple-trapping mechanism and recombination of charge carrier, to describe the anomalous diffusion of photo-generated charge carriers under the influence of external electrical force in amorphous semiconductors.

2.5 Fractal theory

The term 'fractal' is coined by Benoît Mandelbrot in 1975 based on the Latin word '*frangere*' which means broken (Mandelbrot, 1982). A fractal possesses a few characteristics such as (i) self similarity in which an object or geometric shape could be infinitely subdivided into small parts and each of them has a similar shape but reduced size of the original, (ii) scale-invariant which demonstrates the object has fine structure across different scales, (iii) a fractal dimension D_f which can take a non-integer value and strictly greater than its topological dimension D_T. Fractal dimension is considered as a measure of the space-filling capacity of the fractal object within the environment where it is contained, and (iv) the relationship between the number of rescaled copies N_f to cover the original object and the scaling factor r_f takes a power law form in which the fractal dimension D_f is being the scaling exponent.

One of the methods used to obtain the fractal dimension of an object is called Box counting method. A square box with size W_B is used to cover the fractal object and the number of box N_B with size W_B is needed to cover the whole object of area A is recorded. The relationship between N_B and W_B is given by

$$N_B \propto \frac{1}{W_B^{D_B}}, \tag{2.16}$$

where D_B is the box dimension (Minkowski-Bouligand dimension). The measurement process is repeated with different box sizes. The box dimension is then obtained from the slope of the linear least square line that passing through all the points in the log(N_B) versus log(1/W_B) plot. The box dimension is also defined as

$$D_B = \lim_{W_B \to 0} \frac{\log N_B}{\log\left(1/W_B\right)}. \tag{2.17}$$

Similarly, the Hausdorff dimension D_H can be obtained using the similar procedures as that of the box counting method but the fractal object is covered with varying box sizes. Besides, PSD method (see subsection 3.3.1) and DFA (see subsection 3.3.2) could also be used to estimate the scaling exponent and fractal dimension of fractal objects.

Fractal object can be classified, based on its similarity property, as (i) exact self-similarity, (ii) quasi-self-similar and (iii) self-affinity. Exact self-similarity is defined as the set which has the same pattern at all scales. The Sierpinski triangle and von Koch curve are the examples of exact self-similarity geometry as depicted in Figure 2.13 and Figure 2.14, respectively. A Sierpinski triangle could be generated by first taking the midpoints of each side of a triangle (represented by the black triangle in stage 0 as shown in Figure 2.13) to form the vertices of a new triangle (represented by the white triangle in stage 1) which is then removed from the original triangle. Three black similar shape triangles are formed in the original triangle but each of them has only one-fourth the original area and half the original dimension. The same procedure is repeated at each of the black triangle in stage 1, thus nine smaller black triangles are resulted in stage 2. Each of them has only one-fourth the original area and half the original dimension of the triangle in stage 1. After *n* iteration, the number of triangles produced is $N_f = 3^n$, the dimension is $(1/2)^n$ and the area is $(1/4)^n$. The fractal dimension of the Sierpinski triangle is calculated as $D_f = -\log 3/\log(1/2) = 1.585$.

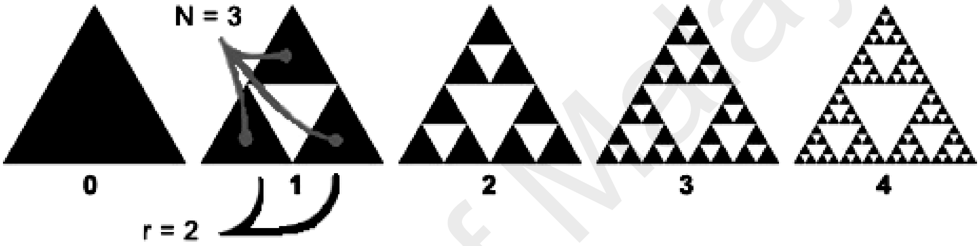

Figure 2.13: Sierpinski triangle. (Fractal organisation)

Von Koch curve, which was developed by Niels Fabian Helge von Koch, can be formed by first removing and replacing the 1/3 middle part of a linear line (initiator, E_0) with the two other sides of an equilateral triangle to arrive at stage E_1, as shown in Figure 2.14. After that, this rule is generated for infinite subsequent levels to ultimately form the von Koch curve (Falconer, 1990). The length of the von Koch curve becomes infinite due to an additional 1/3 length is added onto the curve at every stage. The fractal dimension of the von Koch curve can be calculated as, $D_f = \log 4/\log 3 = 1.26$. Besides, three von Koch curves can be connected together to form a von Koch snowflake.

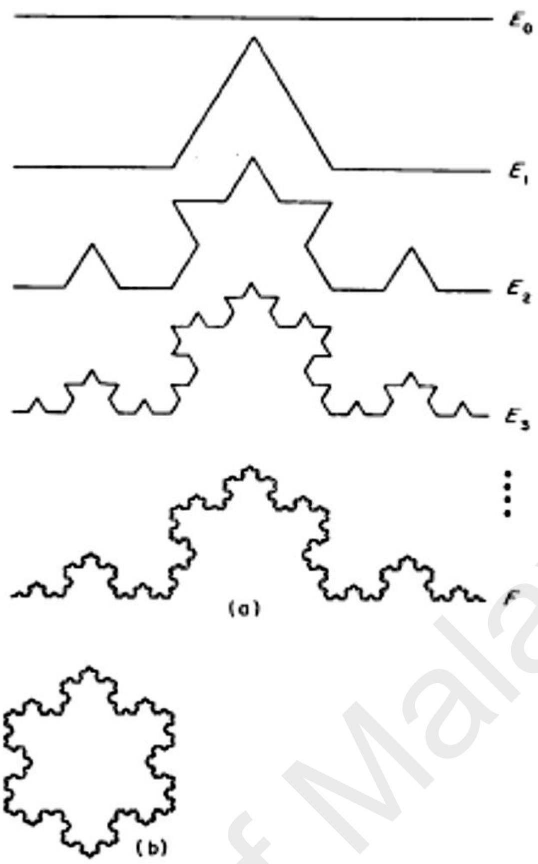

Figure 2.14: (a) von Koch curve at different level of magnification and (b) von Koch snowflake. (Falconer, 1990)

Quasi self-similarity is defined as the set which has arbitrarily small parts of the set that can be magnified and altered smoothly to coincide with a large part of the set. Examples of quasi self-similarity objects are the star-like branching structure of polystyrene and Julia set as shown in Figure 2.15 and Figure 2.16, respectively. As shown in Figure 2.15, the structure of a group of polymer branches takes on a star-shaped structure and the structure of a smaller branch partially bears a resemblance to the whole structure. Star-shaped macro-initiators are first synthesised from the polystyrene initiators using the convergence technique and the star-shaped macro-initiators will then be converged to form the radially linked star-block-linear Polystyrene polymer as showed in Figure 2.15 (Knauss & Huang, 2003).

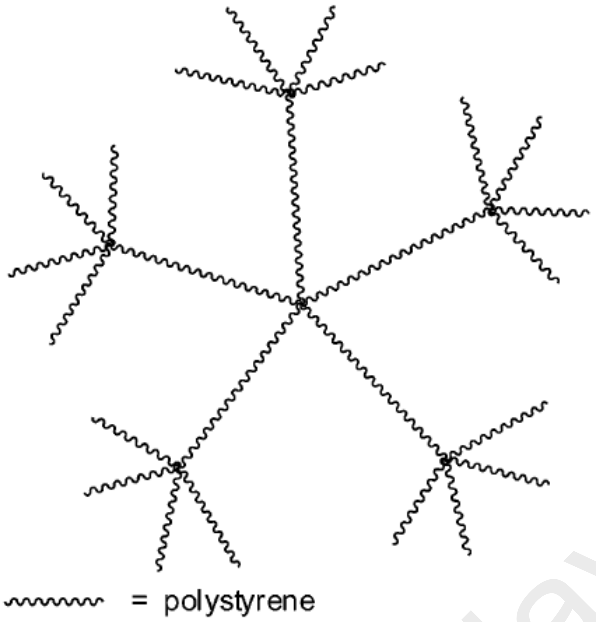

Figure 2.15: Radially linked star-block-linear polystyrene polymers. (Knauss & Huang, 2003)

Julia set, named after Gaston Maurice Julia, which can be described by a quadratic function, $f(z) = z^2 + c$, for a constant c and z is the position in space. For a constant value of $c = -1$, the Julia set has a fractal dimension of 1.27 and the pattern is depicted in Figure 2.16 (McMullen, 1998).

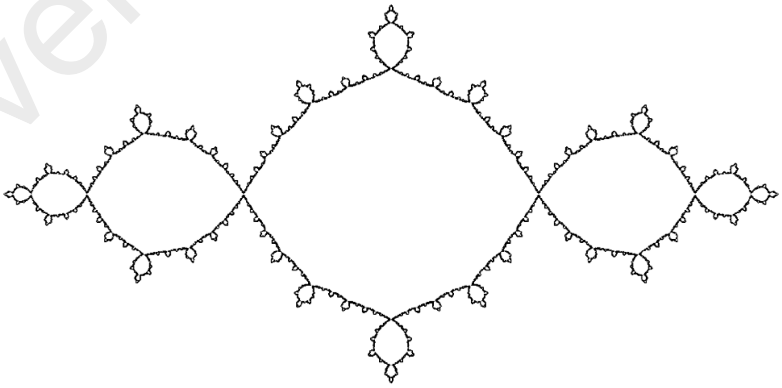

Figure 2.16: Julia set. (McMullen, 1998)

Self-affinity is defined as the set which has pattern possesses same statistical properties at all scales. Romanesco broccoli, fern leaf, morphology of Physarum Polycephalum plasmodium, coastline of Britain and Mandelbrot set are some examples of self-affinity sets. Figure 2.17 shows a Romanesco broccoli and its florets which are disengaged from the original structure at various scales but yet they still resemble the whole structure of the broccoli and demonstrate the present of self-similar property. The arrangements of florets follow certain spiral path where the path begins from the top centre of the broccoli. The spiral path is defined by the Fibonacci spiral (a series of arcs whose radius values are given by the Fibonacci sequence) and the number of spiral paths in a direction is defined by the successive Fibonacci numbers. Besides, the Fibonacci number could also be used to model other fractal nature objects such as the number of branches of tree, arrangement of leafs around tree stem or stump, pattern on the shell of Chambered nautilus and ratio between human fingers and forearm.

Figure 2.17: Romanesco broccoli at different magnification levels. (King, 2016)

Figure 2.18 shows a spleenwort fern which is decomposed into four magnification levels and all the rescaled copies (branches) of the fern look alike the whole structure of the fern. This shows that fern is one of the natural fractal sets that possesses self-similarity property.

Figure 2.18: Fern leaf decomposed to four magnification levels.

Michael Barnsley, a British mathematician, had developed the mathematical formulation and computer algorithm based on the iterated function system, to replicate the pattern of fern (Barnsley, 1993). In the IFS method, the procedures to generate the fern are (i) generating a starting point randomly, (ii) choosing one out of the four sets of coordinate transformations based on its assigned probability, (iii) multiplying the chosen starting point in step (i) by the transformation matrix and then sum with the translation matrix, (iv) the resulting point is then fed as the starting point to generate the next new point and (v) repeating steps (ii) to (iv) for many iterations. Since the whole Barnsley Fern, named after Michael Barnsley, generation process is based on the randomly chosen numbers, thus the Barnsley Fern is considered as a chaotic IFS fractal sets. The computer generated Barnsley Fern is shown in Figure 2.19 and its fractal dimension is estimated to be around 1.45.

Figure 2.19: Barnsley fern generated by IFS method. (Barnsley, 1993)

Figure 2.20 shows the environment dependence of growth morphology of Physarum polycephalum Plasmodium taken after eight hours of cultivation at different concentrations of KCl repellent, oat flake extraction attractant and agar substrate (Takamatsu et al., 2009). The morphology of the plasmodia shows a highly dense round shape network structure with nuclear thin tabular structure. In contrast, the morphology of the plasmodia demonstrated dendrite structure with thick tabular tubes. The tabular structures take the shape of meandering tube and straight tube respectively for low and high concentrations of agar substrate. This is because the attractant KCl softens the cell membrane of the plasmodium and promotes isotropic growth with thin tabular structure. The opposite situation will happen when the plasmodium is grown in the repellent condition that hardens the cell membrane. The fractal dimensions of these morphology patterns are increasing from the repulsive to attraction growth conditions. Nevertheless, all of these morphologies demonstrated self-affine fractal growth patterns.

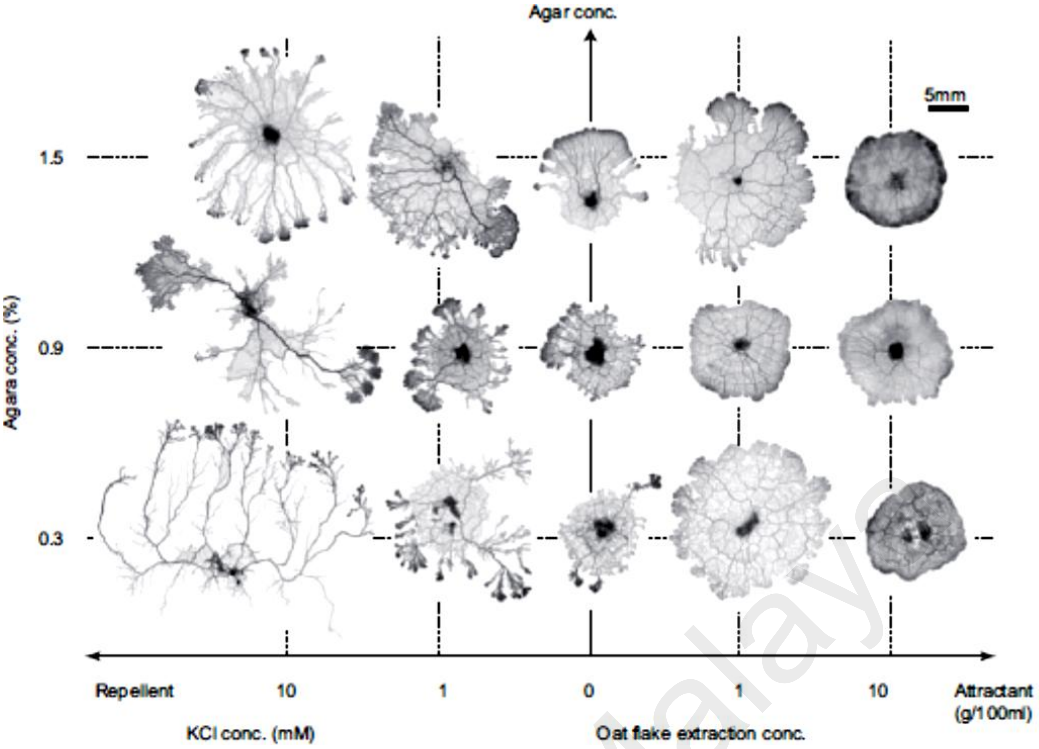

Figure 2.20: The environment dependence of growth morphology of Physarum Polycephalum plasmodium. (Takamatsu et al., 2009)

The Mandelbrot set, as proposed by Benoit B. Mandelbrot, is a set of points z_0 randomly generated in the complex plane via the recursive formula, $z_{n+1} = z_n^2 + z_0$, in which z_0 takes value of complex numbers. The generated points could eventually end up in one of these scenarios, (i) bounded inside the Mandelbrot set and never able to escape from it, (ii) generated close to the boundary of the Mandelbrot set and have the finite chance to escape from the Mandelbrot set via the boundary and (iii) generated outside the boundary of the Mandelbrot set and begin to move towards infinity to form the whiskers line structures, as shown in Figure 2.21.

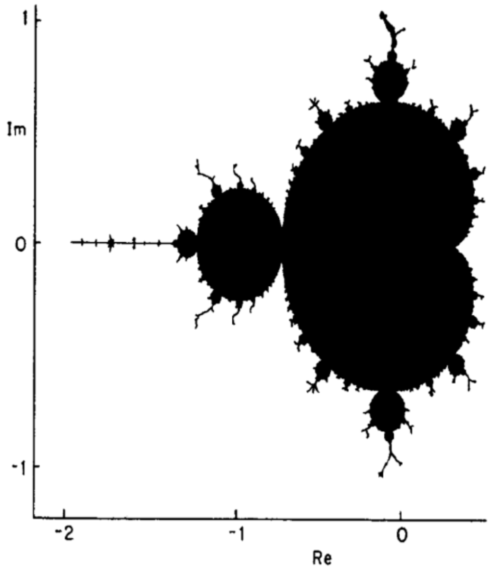

Figure 2.21: Mandelbrot set. (Falconer, 1990)

As shown in Figure 2.22, the coastline of the Great Britain demonstrated high irregularity and winding characteristics in which its total length of coastline varies with the method employed to measure it. The length of the coastline can be measured by first defining the window length W_L of a measuring device and then moving the window along the coastline by sequentially placing the new window on the end point of the previous step. Thus, the total length of the coastline $L(W_L)$ is simply calculated as

$$L(W_L) = N_L W_L \, , \tag{2.18}$$

and it is related to the fractal dimension through

$$L(W_L) \propto \frac{W_L}{{W_L}^{D_f}} \, , \tag{2.19}$$

where N_L is the number of steps covering whole coastline which is given by

$$N_L \propto \frac{1}{{W_L}^{D_f}} \, , \tag{2.20}$$

and D_f is the fractal dimension (Mandelbrot, 1982). As the measurement is repeated with gradually decreasing window length, the actual length of the coastline is expected to be obtained since the coastline is better mapped at very fine scale. However, the measurement shows that the measured length $L(W_L)$ is likely to increase infinitely. This imposes a difficulty to determine the actual length of the coastline as its length varies with the window length used in the measurement. This phenomenon was named as Richardson effect in 1961 after Lewis Fry Richardson. The fractal dimension calculated for the coastline of Britain is $D_f = 1.25$.

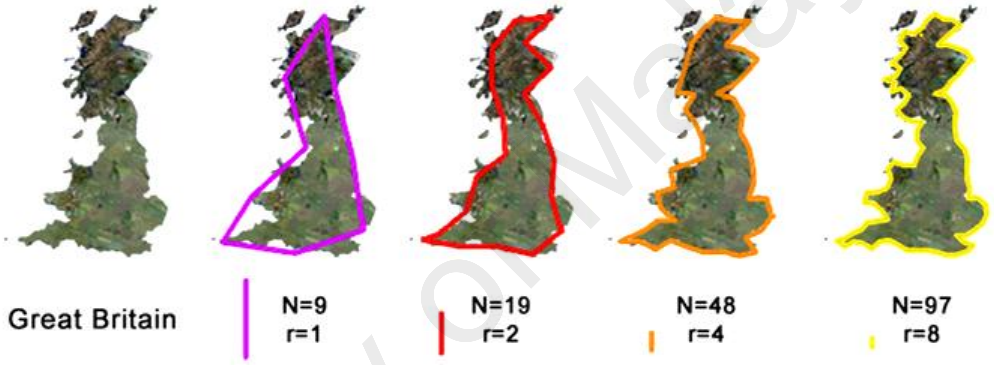

Figure 2.22: Coastline of Great Britain. ("Geometric Fractal - Chapter 2 Fractal Dimension of Coastlines")

The idea of self-similarity is also extended to mathematical function namely the Weierstrass function, proposed by Karl Weierstrass in 1875, which is a continuous function but not differentiable at any point on the function. The Weierstrass function is given by, (Mandelbrot, 1982),

$$f_W(t) = \frac{1}{\sqrt{1-w^2}} \sum_{k=0}^{\infty} w^k \exp\left(2\pi i b^k t\right), \qquad (2.21)$$

where real number $b > 1$, $w = b^H$, the Hölder exponent H has the range of $0 < H < 1$ and the fractal dimension $D_f = 2 - H$ for $1 < D_f < 2$. The Weierstrass function $f_W(t)$ generated for various H values ($H = 0.1$, 0.3, 0.5 and 0.7) are depicted in Figure 2.23. It can be noted that when H value decreases or fractal dimension D_f increases the curve becomes more irregular, space filling and has infinite length.

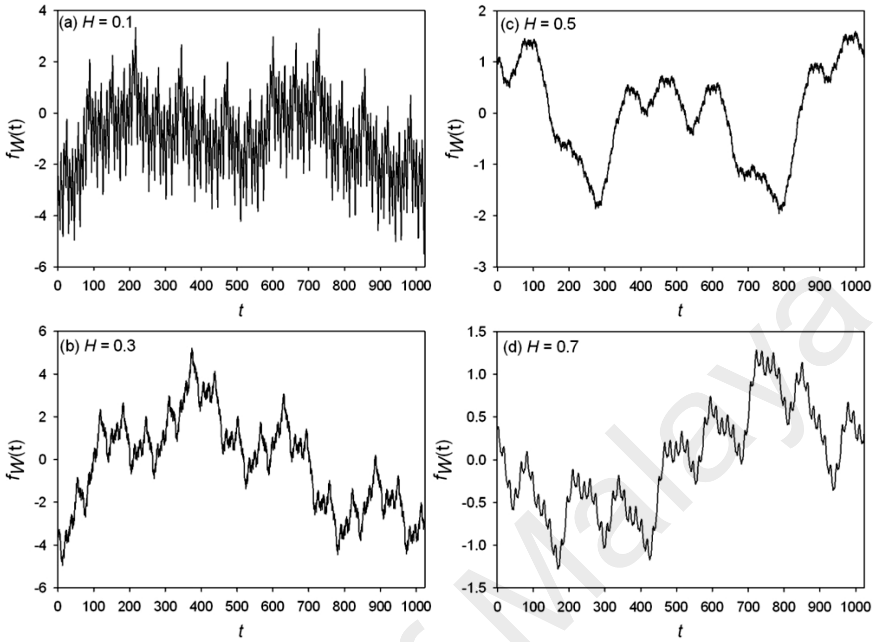

Figure 2.23: Weierstrass function at (a) H = 0.1, (b) H = 0.3, (c) H = 0.5, and (d) H = 0.7. (Canus et al., 2003)

Brownian motion was first discovered by the Scottish botanist, Robert Brown in 1827, through the observation of random movements of pollen particles suspended in the water in which the random moments were caused by the scattering between the particles and water molecules (Brown, 1866). The movement of the Brownian particle presented some fractal properties. However, Brown did not provide the mathematical description of the observed phenomenon. In 1905, Albert Einstein proposed that Brownian motion could be modelled by using the molecular kinetic theory of heat (Einstein, 1905). Albert Einstein deduced that the average distance travelled by a particle was proportional to the square root of travelling time, $x \propto \sqrt{t}$. In 1909, a French physicist, Jean Baptiste Perrin performed an experiment to observe and record the displacement of particles suspended in liquid medium through a microscope and a *camera lucida*. The positions and trajectories of the microscopic movement of particles were recorded at regular time intervals and respectively represented by the dots and lines as shown in Figure 2.24. The recorded trajectories demonstrated the stochastic nature of the movements of particles due to the collisions with water molecules. Perrin concluded that the mean squared distance travelled by particles changes linearly with time and reaffirmed the molecular kinetic theory of heat developed by Albert Einstein (Bigg, 2008; Perrin et al., 1910). He also pointed out that the irregular movements of the particles coincided with non-differentiable continuous functions.

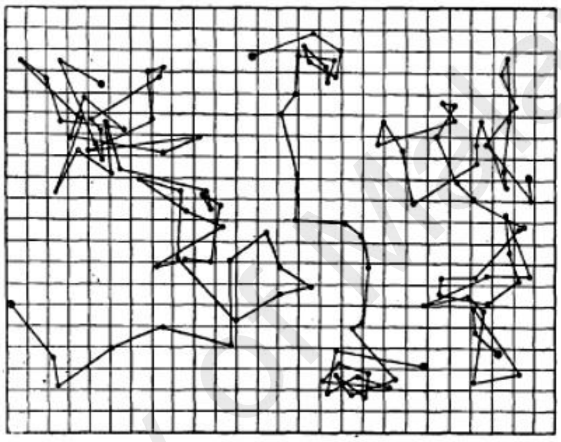

Figure 2.24: Displacement of three particles recorded in the experiment conducted by Perrin. (Perrin et al., 1910)

Almost two decades later, an American Mathematician, Norbert Wiener, had rigorously developed the mathematical framework to describe the trajectory followed by a single particle or Brownian motion based on the continuous non-differentiable function theory (Wiener, 1923). Brownian motion is a random process $B(t)$ which has the following properties (Mandelbrot, 1982):

(i) With probability of 1, $B(0) = 0$, $B(t)$ is continuous, Gaussian distributed and nonstationary.

(ii) $B(t)$ possesses self-affinity which gives $B(t) \equiv s^{-0.5} B(st), s > 0$ and it will be regenerating itself at every time instant which leads to short memory effect.

(iii) The spectral density of $B(t)$ has power law behaviour defined as $S(f) \propto f^{-(1+2H)} \propto f^{-2}$, where $2H + 1 = 2$, thus $H = 0.5$.

(iv) The increments, $dB = B(t+\Delta t) - B(t)$, of $B(t)$ are white Gaussian noise with zero mean, $E\left[B(t)\right] = 0$, variance depends linearly with time, $Var\left[B(t+\Delta t)\,B(t)\right] \propto \Delta t$, independent, uncorrelated and stationary process.

(v) $B(t)$ is the integral of $dB(t)$.

Figure 2.25 demonstrates a simulated Brownian motion at different scales and it is considered as one of the natural self-affinity fractals. The total length of the Brownian motion increases as the step interval is reduced and becomes infinite when the step interval is approaching zero. Thus, the fractal dimensions of the Brownian motions depicted in Figure 2.25 take values between one and two, $1 < D_f < 2$.

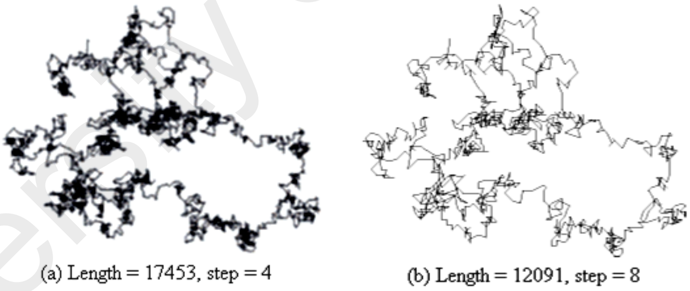

(a) Length = 17453, step = 4 (b) Length = 12091, step = 8

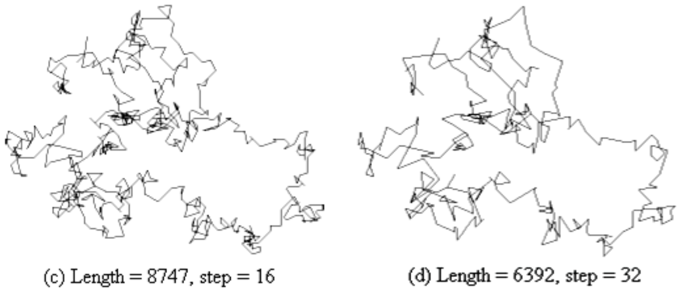

(c) Length = 8747, step = 16 (d) Length = 6392, step = 32

Figure 2.25: Brownian motion simulated at various step intervals. (Turner et al., 1998)

Brownian motion could also be represented in a graph as shown in Figure 2.26. It is obvious that the self-similar property is presented as the curves at different level of magnifications resemble the original curve.

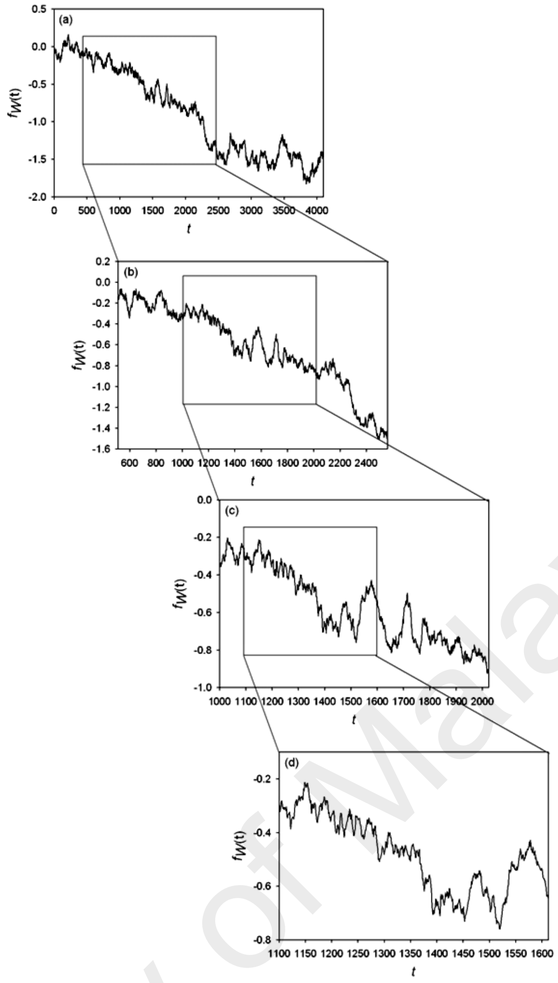

Figure 2.26: Brownian function, *H* = 0.5, at various magnification levels. (Canus et al., 2003)

Besides, fractal set is sometimes classified as monofractal or multifractal. Monofractal is the fractal set which possesses only one fractal dimension. For example, Koch snowflake, Cantor set, coastline of Britain, Brownian motion and fractional Brownian motion. Multifractal is fractal set which possesses a series of fractal dimensions, for instances, multifractal Brownian motion.

2.5.1 Fractal modelling of signals and surfaces

Fractional Brownian motion is another example of a mathematical function that presents self-affinity pattern as depicted in Figure 2.27. The reduction in *H* value decreases the jaggedness and also smoothens the curve. Brownian motion with *H* = 0.5 is a special case of the FBM.

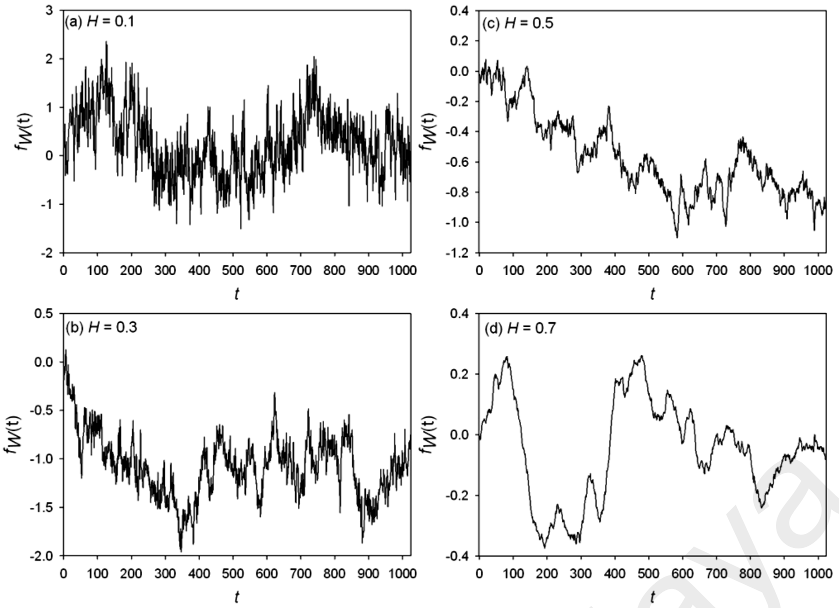

Figure 2.27: Fractional Brownian motion at various *H* values. (Canus et al., 2003)

Fractional Brownian motion is derived by Benoit B. Mandelbrot using the RL fractional integral as (Mandelbrot, 1982; Mandelbrot & Van Ness, 1968):

$$\frac{1}{\Gamma(H+1/2)}\int_0^t |t-s|^{H-1/2}\,dB(s), \tag{2.22}$$

where *dB*(*u*) is the white noise. Equation (2.22) will exit if $s \to t$, *H* should be positive value and achieve stationary increments, thus Equation (2.22) is rewritten using the Weyl's integral as,

$$B_B(t)=\frac{1}{\Gamma(H+1/2)}\int_{-\infty}^t |t-s|^{H-1/2}\,dB(s). \tag{2.23}$$

Since *t* could attain values from both the directions of the coordinate, thus it will be more practical to write the Equation (2.23) in its symmetric form which is defined as,

$$B_H(t)=\frac{1}{\Gamma(H+1/2)}\left[\int_{-\infty}^0\left(|t-s|^{H-1/2}-|-s|^{H-1/2}\right)dB(s)+\int_0^t |t-s|^{H-1/2}\,dB(s)\right]. \tag{2.24}$$

Equation (2.24) is called the FBM and its properties are given below:

(i) With probability of 1, $B_H(0) = 0$, $B_H(t)$ is continuous, random, Gaussian distributed and nonstationary process.

(ii) $B_H(t)$ possesses self-affinity which gives $B_H(t) \equiv s^{-H} B_H(st), s > 0$ and it will be regenerating itself at every time instant which leads to short memory effect.

(iii) The spectral density of $B_H(t)$ has power law behaviour defined as $S(f) \propto f^{-(1+2H)} \propto f^{-\beta_{PS}}$, where $\beta_{PS} = 2H + 1$ is the power spectra scaling exponent. White noise, $1/f$ noise and Brownian noise are respectively represented by $\beta_{PS} = 0$, $\beta_{PS} = 1$ and $\beta_{PS} = 2$.

(iv) The increments, $dB_H = B_H(t+\Delta t) - B_H(t)$, of the FBM $B_H(t)$ are called the fractional Gaussian noise with zero mean, $E\left[B_H(t)\right] = 0$, covariance depends linearly with time, $Var\left[B_H(t+\Delta t) B_H(t)\right] \propto \Delta t^{2H}$, independent, uncorrelated and stationary process.

(v) $B_H(t)$ is the integral of $dB_H(t)$.

(vi) The fractal dimension of the FBM is given by $D_f = 2 - H$.

Since the power spectra scaling exponents β_{PS} could be used to characterise the fractal or scaling behaviour of a time series (either a signal or noise), thus the PSD method and FBM could be used for time series analysis or modelling. Nevertheless, FBM could also be used for surface and terrain analysis and modelling. Figure 2.28 shows typical examples of fractal surfaces which are generated using the fractional Brownian motion in two dimensional spaces for different values of H ranging from 0.1 to 0.7. At small H value, the surface forms many small clusters and spread randomly throughout the whole area. Oppositely, the surface forms few large clusters and contain in a small area at large H value. Thus, the surface is changing from a small size segregated cluster to a large concentrated cluster as H value increases.

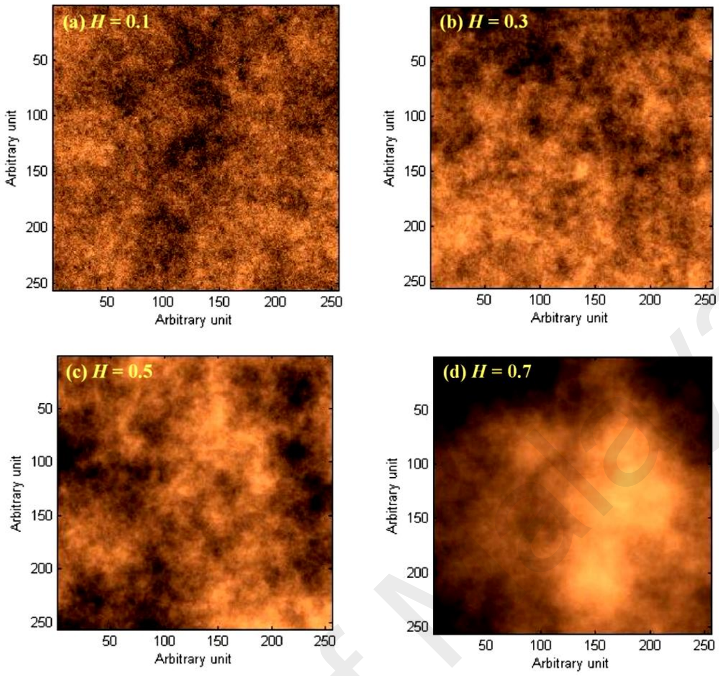

Figure 2.28: Fractional Brownian surfaces for (a) H = 0.1, (b) H = 0.3, (c) H = 0.5 and (d) H = 0.7. (Canus et al., 2003)

Kong and co-workers utilised the generalised Cauchy process, namely semi-variogram, to analyse the fractal and long-range correlation properties of surface morphologies of organic nickel(II) phthalocyanine-tetrasulfonic acid tetrasodium thin film (Kong et al., 2014, 2017). The correlation function of the semi-variogram is defined as

$$C_{vg}\left(h_{vg}\right) = \sigma_{vg}^{2} - \frac{\sigma_{vg}^{2}}{\left(1+\left|h_{vg}/s_{vg}\right|2H\right)^{\beta_{vg}/2H}} \,, \tag{2.25}$$

where H is the Hurst exponent related to the fractal dimension D_f through $D_f = 3 - H$ and β_{vg} is correlation exponent related to the long-range dependence through $1 - \beta_{vg}/2$. The surface roughness is described by the Hurst exponent or fractal dimension and the correlation between two points on the surface is described by the long-range dependence. Conductivity of charge carriers is found to be increasing with the fractal dimension and further enhancement of conductivity is due to the existence of correlated surface morphologies.

Diffusion-limited aggregation was originally developed by Witten and Sander in which the correlations between positions of particles are considered to be scale-invariant objects. These objects are described by the density-density correlation function which is defined as

$$\left\langle P\left(r'+r\right)P\left(r'\right)\right\rangle \sim r^{-\alpha_{DLA}} , \tag{2.26}$$

where the scaling exponent α_{DLA} is related to the Hausdorff dimension via $D_H = D_T - A$, D_T is the topological dimension and A is area (Witten & Sander, 1983). Diffusion-limited aggregation could be used to model surface growth, dust deposition, dendrites growth and also polymer branch (Wang et al., 2011).

Wool and Long (1993) has used the gradient percolation theory (Sapoval et al., 1985) to study the random diffusion of atoms passing through the polymer interfaces where the diffusion front is obeying fractal properties as shown in Figure 2.29. The roughness and width of the diffusion front increase with the diffusion length.

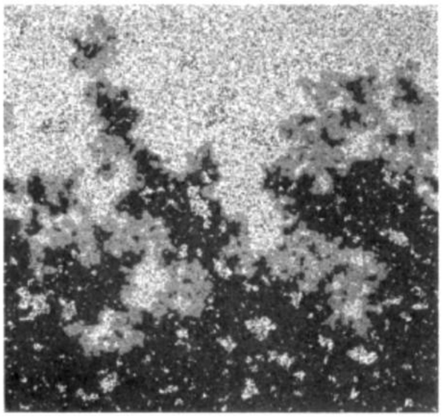

Figure 2.29: Gradient percolation of atoms with diffusion length L_D = 10240 on a 512×512 lattice. (Wool & Long, 1993)

The diffusion front is characterised by the mass-to-radius relation as

$$m_D \propto r_D^{D_f} \, , \tag{2.27}$$

where m_D is the mass, r_D is the radius and D_f is the fractal dimension. The width of the diffusion front σ_f is related to the diffusion length L_D as

$$\sigma_f \approx L_D^{\alpha(\sigma_f)} \, , \tag{2.28}$$

and the scaling exponent of DLA $\alpha(\sigma_f)$ is related to the percolation exponent ς and fractal dimension as

$$\alpha\left(\sigma_f\right) = \frac{\varsigma}{1+\varsigma} = 1/D_f \, . \tag{2.29}$$

2.5.2 Fractal dynamics

Stanley formerly published a work describing how fractal concepts could be applied to polymer and anomalous transport in porous media (Stanley, 1984). An example is the relation between the fractal dimension of backbone of polymer with electric current flow and random walker. In crystalline media, the Fick's diffusion law defines that the r.m.s. displacement $\langle x^2 \rangle^{0.5}$ of a random walker is linearly proportional to the number of steps N_W made by the walker which is given by

$$\left\langle x^2 \right\rangle^{0.5} = N_W \, . \tag{2.30}$$

If a random walker is moving in a porous media, it will only be able to travel a smaller distance away from its origin as compared to the random walker that is moving in a crystalline material. Thus, Equation (2.30) is redefined as

$$\left\langle x^2 \right\rangle^{0.5} \propto \left(N_W \right)^{D_W}, \tag{2.31}$$

where $D_W \leq 1$ (Stanley, 1984). Equation (2.31) is equivalent to the mass-to-radius relation given by Equation (2.27). Let's say that the random walk represents the free flight polymer chain and the walker represents the charge carrier propagating along the backbone of the chain which is characterised by the fractal dimension, thus $1/D_W$ is equivalent to the fractal dimension D_f of the random walker (polymer chain), number of walker steps N_W is equivalent to the mass of the polymer chain m_D and r.m.s. displacement is equivalent to the length of the random walk. Since the electrical current density is proportional to the velocity of charge carriers, thus electrical current density could be calculated by taking the time rate of change of MSD of the random walkers multiplied by the electronic charge and density of charge carriers.

Diffusion is a Markov process which could be considered as a continuous time stochastic process with continuous paths if the changes in time and space are infinitely small. Thus, diffusion process could be represented by Brownian motion or Wiener process through a stochastic differential equation that takes the form of (Øksendal, 2003),

$$dX_t = \alpha\left(t, X_t\right) + \beta\left(t, X_t\right) dW_t \ , \tag{2.32}$$

where dW_t is white noise (time derivative of Wiener process or Brownian motion), $\alpha(t,X_t)$ is a drift coefficient and $\beta(t,X_t)$ is a diffusion coefficient. White noise is a stochastic process with Gaussian distribution and zero mean. Since W_t is a continuous but non-differential function, Equation (2.32) could not be solved directly and usually is written in its integral form as

$$X_t\left(\omega\right) = X_{t_0}\left(\omega\right) + \int_{t_0}^{t} \alpha\left(s, X_s\left(\omega\right)\right) ds + \int_{t_0}^{t} \beta\left(s, X_s\left(\omega\right)\right) dW_s\left(\omega\right), \tag{2.33}$$

and the solution X_t of Equation (2.33) gives the diffusion process.

2.6 Normal diffusion theory for charge transport in ordered material

This subsection provides the introduction to several charge transport theories which are formulated for normal diffusion process adopted in crystalline media. These transport models could be generalised using the fractional calculus to model the anomalous diffusion in disordered material. Thus, the concept of fractional calculus is given before the description of the anomalous transport theories.

(a) ***Diffusion equation based on Fick's law and law of conservation of mass***

In 1885, Adolf Fick published his work entitled "Uber Diffusion" in Annalen der Physik which described diffusion of particles in liquid medium confined by membranes is due to the existence of concentration gradient. The existence of concentration gradient causes particles to begin moving away from the high concentration region to their surrounding regions with lower concentration till the equilibrium of concentration is achieved.

According to Fick’s first law (Fick, 1855), the flow current density of particles is proportional to the concentration gradient which is written as

$$j(x,t) = -D\frac{\partial c(x,t)}{\partial x}, \tag{2.34}$$

where D is the diffusion coefficient with dimension of L^2/T, $c(x,t)$ is the concentration of particle, x is the position in one-dimensional Cartesian-coordinate space and t is time of particle at x. Based on the law of conservation of mass, the continuity equation is defined as

$$\frac{\partial c(x,t)}{\partial t} = -\frac{\partial j(x,t)}{\partial x}. \tag{2.35}$$

By substituting Equation (2.34) in Equation (2.35), Fick’s second law, which is also commonly known as the diffusion equation, is resulted as

$$\frac{\partial c(x,t)}{\partial t} = D\frac{\partial^2 c(x,t)}{\partial x^2}\ . \tag{2.36}$$

The diffusion equation in Equation (2.36) describes the temporal evolution of the concentration.

(b) ***Drift-diffusion equation based on Fick's law***

If the particle is subjected to an external force $F(x)$, the continuity equation is rewritten as

$$j(x,t) = v(x)c(x,t) - D\frac{\partial c(x,t)}{\partial x}, \tag{2.37}$$

where $v(\mathrm{x}) = \mu F(\mathrm{x})$ is the velocity of the particle and μ is the mobility. Thus, the drift-diffusion equation is resulted when Equation (2.37) is substituted into Equation (2.35) and it is written as

$$\frac{\partial c(x,t)}{\partial t} = D\frac{\partial^2 c(x,t)}{\partial x^2} - \frac{\partial}{\partial x}\left[\mu F(x)c(x,t)\right]. \tag{2.38}$$

(c) ***Diffusion equation based on random walk theory***

In 1905, Albert Einstein (1905) derived the diffusion equation for random walker (or Brownian molecular motion) based on the postulates of molecular kinetic theory of heat in which particles move independently subjected to the influence of thermal energy. Let’s say a particle is located at the origin and it has an equal probability of jumping an equal length Δx to the left or to the right empty site at each short time interval Δt. The state probability $P(x,t)$ of the particle will be at position $x = i\Delta x$ and at time $t = k\Delta t$ is given by

$$P(x,t) = \frac{1}{2}P(x-\Delta x, t-\Delta t) + \frac{1}{2}P(x+\Delta x, t-\Delta t). \tag{2.39}$$

By expanding the two probability terms, in the R.H.S. of Equation (2.39), using the Taylor-series expansion, one gets

$$\begin{aligned} P(x-\Delta x, t-\Delta t) \approx\ & P(x,t) - \Delta x \frac{\partial P(x,t)}{\partial x} - \Delta t \frac{\partial P(x,t)}{\partial t} \\ & + \frac{(\Delta x)^2}{2}\frac{\partial^2 P(x,t)}{\partial x^2} + \frac{(\Delta t)^2}{2}\frac{\partial^2 P(x,t)}{\partial t^2} \\ & + \Delta x \Delta t \frac{\partial^2 P(x,t)}{\partial x \partial t} + O\left[(\Delta x)^3\right] + O\left[(\Delta t)^3\right], \end{aligned} \tag{2.40}$$

and

$$\begin{aligned} P(x+\Delta x, t-\Delta t) \approx\ & P(x,t) + \Delta x \frac{\partial P(x,t)}{\partial x} - \Delta t \frac{\partial P(x,t)}{\partial t} \\ & + \frac{(\Delta x)^2}{2}\frac{\partial^2 P(x,t)}{\partial x^2} + \frac{(\Delta t)^2}{2}\frac{\partial^2 P(x,t)}{\partial t^2} \\ & - \Delta x \Delta t \frac{\partial^2 P(x,t)}{\partial x \partial t} + O\left[(\Delta x)^3\right] + O\left[(\Delta t)^3\right]. \end{aligned} \tag{2.41}$$

Retain only the leading order terms in Δx and Δt, and then substitute Equation (2.40) and Equation (2.41) into Equation (2.39), thus one gets the diffusion equation for one-dimensional space as

$$\frac{\partial P(x,t)}{\partial t} = D\nabla^2 P(x,t), \tag{2.42}$$

where $D = (\Delta x)^2 / 2\Delta t$ is the diffusion coefficient and the probability $P(x,t)$ of finding the particle at x and time t is related to the concentration of particle $c(x,t)$ which is given by

$$c(x,t) = NP(x,t), \tag{2.43}$$

and N is the total number of particles in the system. By solving Equation (2.42), the propagation of particle away from the origin of coordinates in one-dimensional space is given by

$$P(x,t) = \frac{1}{(4\pi Dt)^{1/2}} e^{-x^2/4Dt}. \tag{2.44}$$

The mean squared displacement of the particle is then given by

$$\left\langle x^2(t) \right\rangle = \int_{-\infty}^{\infty} x^2 P(x,t)\, d^3x = 2Dt. \tag{2.45}$$

Thus, Equation (2.45) demonstrated that the MSD of the normal diffusion of random walker is linearly proportional to time or $\left\langle x^2(t) \right\rangle \propto t$.

(d) Advection-diffusion equation based on random walk theory

If a particle is located at the origin and subjected to an external force, the probability of the particle to jump a length Δx to the left empty site is not the same as the probability of the particle to jump the same length to the right empty site at each short time interval Δt. Let’s define that r_1 and r_2 are the transition probability of flow to right and left, respectively. The state probability $P(x,t)$ of the particle will be at position $x = i\Delta x$ and at time $t = k\Delta t$ is given by

$$P(x,t) = r_2 P(x - \Delta x, t - \Delta t) + r_1 P(x + \Delta x, t - \Delta t). \tag{2.46}$$

By expanding the two probability terms, in the R.H.S. of Equation (2.46), using the Taylor-series expansion, one gets

$$\begin{aligned} r_1 P\left(x-\Delta x, t-\Delta t\right) \approx r_1 P\left(x,t\right) - r_1 \Delta x \frac{\partial P\left(x,t\right)}{\partial x} - r_1 \Delta t \frac{\partial P\left(x,t\right)}{\partial t} \\ + \frac{r_1 \left(\Delta x\right)^2}{2} \frac{\partial^2 P\left(x,t\right)}{\partial x^2} + \frac{r_1 \left(\Delta t\right)^2}{2} \frac{\partial^2 P\left(x,t\right)}{\partial t^2} \\ + r_1 \Delta x \Delta t \frac{\partial^2 P\left(x,t\right)}{\partial x \partial t} + O\left[\left(\Delta x\right)^3\right] + O\left[\left(\Delta t\right)^3\right], \end{aligned} \tag{2.47}$$

and

$$\begin{aligned} r_2 P\left(x+\Delta x, t-\Delta t\right) \approx r_2 P\left(x,t\right) + r_2 \Delta x \frac{\partial P\left(x,t\right)}{\partial x} - r_2 \Delta t \frac{\partial P\left(x,t\right)}{\partial t} \\ + \frac{r_2 \left(\Delta x\right)^2}{2} \frac{\partial^2 P\left(x,t\right)}{\partial x^2} + \frac{r_2 \left(\Delta t\right)^2}{2} \frac{\partial^2 P\left(x,t\right)}{\partial t^2} \\ - r_2 \Delta x \Delta t \frac{\partial^2 P\left(x,t\right)}{\partial x \partial t} + O\left[\left(\Delta x\right)^3\right] + O\left[\left(\Delta t\right)^3\right]. \end{aligned} \tag{2.48}$$

Retain only the leading order terms in Δx and Δt, and then substitute Equation (2.47) and Equation (2.48) into Equation (2.46), thus one gets the advection-diffusion equation for one-dimensional space as

$$\frac{\partial P\left(x,t\right)}{\partial t} = D \frac{\partial^2 P\left(x,t\right)}{\partial x^2} - v \frac{\partial P\left(x,t\right)}{\partial x}, \tag{2.49}$$

where $D = \left(\Delta x\right)^2 / 2\Delta t$ is the diffusion coefficient and $v = \left(r_1 - r_2\right) \Delta x / \Delta t$ is advection coefficient. The second term on the R.H.S. of Equation (2.49) represents the advection flow of particles due to the external force. Equation (2.49) is considered as the Smoluchowski equation (Smoluchowski, 2010) and similar to drift-diffusion equation (see Equation (2.38)) when the probability $P(x,t)$ is replaced by the concentration of the charge particle as given by Equation (2.43). The resulted partial differential equation represents the time evolution of the concentration profile of particles simultaneously due to diffusion and advection processes.

Let's say the external force is given by $F(x) = -dV(x)/dx$, which is induced by an applied potential $V(x)$, Equation (2.49) can be rewritten as, (Coffey et al., 2004; Fokker, 1914; Risken & Frank, 1996),

$$\frac{\partial P(x,t)}{\partial t} = D\frac{\partial^2 P(x,t)}{\partial x^2} - \frac{\partial}{\partial x}\left[\frac{F(x)}{m\gamma_{LE}}P(x,t)\right], \tag{2.50}$$

where m is the mass of particle, γ_{LE} is the friction constant and the diffusion coefficient D can be given by the Einstein-Stokes-Smoluchowski relation as $D = k_B T/m\gamma_{LE}$ (Einstein, 1905; Hughes, 1995; Kubo, 1966). Equation (2.50) is a specialised form of the Fokker-Planck equation which is known as the Smoluchowski equation (Mazo, 2009).

(e) ***Diffusion equation based on Langevin equation***

When a particle is suspended in a liquid and subjected to an external force, it will experience frictional drag acting against its motion and random collisions with the thermal agitated liquid molecules as it is moving from one place to another place. The motion of the particle can be described by a stochastic differential equation for Brownian motion, namely Langevin equation, given by (Kubo, 1966; Zwanzig, 2001),

$$m\frac{d^2x}{dt^2} = F(x) - m\gamma_{LE}v + \lambda_{LE}(t), \tag{2.51}$$

where m is the mass of the particle, η is the viscosity of the fluid, $\gamma_{LE} = \zeta_{LE}/m$ is the friction constant, $\zeta_{LE} = 6\pi r_a \eta_{LE}$ is the friction coefficient, r_a is the radius of the particle, v is the velocity, $F(x)$ is the external force and $m\gamma_{LE}v$ is the frictional force. The random fluctuating force due to the collisions of particle with liquid molecules $\lambda_{LE}(t)$ is Gaussian distributed and has the following properties as,

$$\left\langle \lambda_{LE}\left(t\right)\right\rangle = 0\,, \tag{2.52}$$

and

$$\left\langle \lambda_{LE}\left(t\right)\lambda_{LE}\left(t'\right)\right\rangle = 2k_B T\zeta_{LE}\delta\left(t-t'\right). \tag{2.53}$$

Equation (2.53) relates the strength of the fluctuating force to the magnitude of the friction or dissipation of the liquid which is characterised by ζ_{LE} . This relation is known as the fluctuation-dissipation theorem (Agarwal, 1972; Kubo, 1966; Zwanzig, 2001). Besides, the friction coefficient is also related to the diffusion of the particle via the Einstein-Stokes-Smoluchowski relation as $D = k_\mathrm{B}T/\zeta_{LE}$. Thus, the frictional coefficient is also referred as inverse mobility.

2.7 Fractional calculus theory

Fractional calculus has been developed since 1695, almost as old as the integer calculus, when Gottfried von Leibnitz replied to Guillaume de l'Hôpital after he had been asked for the meaning of $d^\mathrm{n}y/dx^\mathrm{n}$ if n = 1/2 and wrote, "Thus, it follows that $d^{1/2}x$ will be equal to $x\sqrt{dx:x}$,...from which one day useful consequences will be drawn." (Sokolov et al., 2002). Unlike integer order differential equation which has been widely accepted and used in describing many physical phenomena, but fractional differential equation has received very little attention till few decades ago. The foundation of fractional calculus has been contributed by many great scientist (such as Pierre-Simon Laplace, Bernhard Riemann, Joseph Liouville, Michele Caputo and many more) before it could be readily used in describing physical phenomena. The applications of fractional calculus could be found in science, engineering (Hilfer, 2000a) and financial industry (Scalas et al., 2000).

The fractional derivative is defined as the derivative of arbitrary real order α which is denoted as

$$ {}_aD_t^{\alpha} f(t), \tag{2.54}$$

and the fractional integral is defined as the integral of arbitrary real order α which is denoted as

$$ {}_aD_t^{-\alpha} f(t). \tag{2.55}$$

The negative '–' symbol prior to α in Equation (2.55) indicates that Equation (2.55) is a fractional integral operator. The subscripts *a* and *t* represent the two end limits of the operation of the fractional derivative or integration (Podlubny, 1998; Sokolov et al., 2002).

The *n*-th derivative is the same as an inverse operation of *n*-fold integration, *n* is an integer, which is given as

$$\int_a^t \int_a^{s_1} \ldots \int_a^{s_{n-1}} f(s_n)ds_n \ldots ds_1 = \frac{1}{(n-1)!}\int_a^t (t-s)^{n-1} f(s)ds. \tag{2.56}$$

Equation (2.56) is satisfied at $t = a$ and the derivatives of the R.H.S. and L.H.S. of the equation are the same. By replacing the integer order *n* with an arbitrary order α and the factorial with a Gamma function for real argument, Equation (2.56) is then generalised to the fractional integral of order α as

$$ {}_aD_t^{-\alpha} f(t) = \frac{1}{\Gamma(\alpha)}\int_a^t (t-s)^{\alpha-1} f(s)ds, \qquad t \geq a. \tag{2.57}$$

Thus, fractional derivative of order α is defined via the fractional integration and successive integer differentiation which is mathematically written as

$$ {}_aD_t^{\alpha} f(t) = \frac{d^n}{dt^n}\, {}_aD_t^{\alpha-n} f(t) \,. \tag{2.58}$$

or

$$ {}_aD_t^{\alpha} f(t) = \frac{1}{\Gamma(n-\alpha)} \frac{d^n}{dt^n} \int_a^t (t-s)^{n-\alpha-1} f(s) ds \,. \tag{2.59}$$

The number of differentiations is $n = [\alpha] + 1$ where $[\alpha]$ is the whole part of α. Base on this definition, the lower limit becomes zero. Equation (2.57) is rewritten as

$$ {}_0^{RL}D_t^{-\alpha} f(t) = \frac{1}{\Gamma(\alpha)} \int_0^t (t-s)^{\alpha-1} f(s) ds \,, \tag{2.60}$$

where $n - 1 < \alpha < n \in Z^+$ and called the RL fractional integral of order α. Similarly, Equation (2.58) or Equation (2.59) is called the RL fractional derivative of order α and written as

$$ {}_0^{RL}D_t^{\alpha} f(t) = \frac{1}{\Gamma(n-\alpha)} \frac{d^n}{dt^n} \int_0^t (t-s)^{n-\alpha-1} f(s) ds \,, \tag{2.61}$$

where $n - 1 \leq \alpha < n \in Z^+$. The RL fractional derivative could be viewed as an integral-differentiation equation.

It should be noted that the RL fractional derivative of a constant is not zero but given as

$$ {}_0^{RL}D_t^{\alpha} 1 = \frac{1}{\Gamma(1-\alpha)} t^{-\alpha} \,, \tag{2.62}$$

because $\Gamma(1 - \alpha)$ diverges if the fractional derivative order α takes a non integer value. Besides, the Laplace transform of the RL fractional integral results in a simple form as

$$L\left\{ {}_{0}^{RL}D_{t}^{-\alpha} f\left(t\right) \right\} = u^{-\alpha} L\left\{ f\left(t\right) \right\}. \tag{2.63}$$

If the lower limit of Equation (2.57) becomes $-\infty$, the Weyl fractional derivative of an exponential function yields

$${}_{-\infty}^{W}D_{t}^{\alpha} e^{t} = e^{t}. \tag{2.64}$$

The Fourier transform of the Weyl fractional derivative or integration produces the similar properties of Fourier transform of integer order derivative or integration, respectively. For instance,

$$F\left\{ {}_{-\infty}^{W}D_{t}^{\alpha} f(t) \right\} = \left(i\omega\right)^{2} f\left(\omega\right). \tag{2.65}$$

Caputo fractional derivative is a differentiation-integral equation which is given by,

$${}_{0}^{C}D_{t}^{\alpha} f(t) = \frac{1}{\Gamma\left(n-\alpha\right)} \int_{0}^{t} \left(t-s\right)^{n-\alpha-1} f^{(n)}(s) ds, \tag{2.66}$$

where $n - 1 < \alpha < n \in Z^{+}$. Unlike the RL fractional derivative, the Caputo fractional derivative of a constant is zero.

2.8 Theories of anomalous charge transport

It has been demonstrated that there are many transport processes in physical systems deviate from the normal diffusion process as their MSD values depend non-linearly on time. One typical example is the present of long tail transient photocurrent curves of disordered organic semiconductor measured by the TOF measurement. The following section will describe how the TOF measurement can be used as an important technique to study the anomalous transport of charge carriers in disordered organic semiconductor. The related charge transport theories for anomalous diffusion are then described in the subsequent sub-sections.

2.8.1 Time-of-flight measurement

Time-of-flight measurement is one of the important techniques which can be used to study the mobility of charge carriers, probing on the information about the defects located within the surface, interface or bulk material. A basic setup of a TOF measurement is depicted in Figure 2.30.

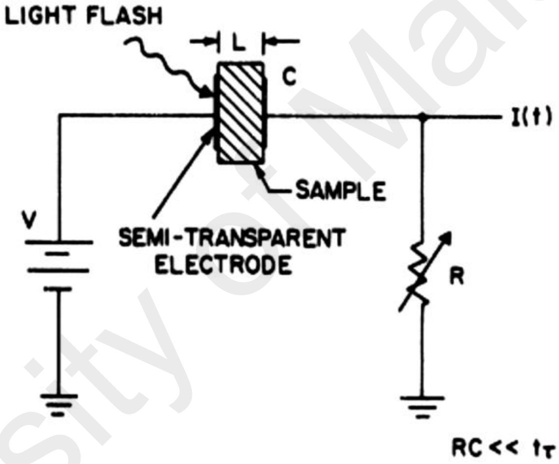

Figure 2.30: A basic setup for a TOF measurement. (Scher & Montroll, 1975)

A light pulse, which is generated by a laser source, is shone on a DUT (or TOF cell) while it is biased. The time taken by a packet of charge carriers to drift across the DUT is measured and then used to determine the charge carrier transit time t_{tr}. The measured transient current is given by

$$I(t) = \frac{1}{L}\int_0^L j(x,t)\,dx, \tag{2.67}$$

where $j(x,t)$ is the conduction current density and L is the length or thickness of the TOF cell.

The measured transient current is affected by a few factors such as (i) RC time constant τ_{rc}, (ii) loss of charge carriers due to deep energy level trapping, (iii) spatial variation of mobility due to material inhomogeneity of the DUT, (iv) spatial variation in electric field due to trapped charge carriers in small signal case, (v) spatial variation in electric field due to space charge effect in large signal case and (vi) spreading of the pulse width of charge carrier packet which is comparable to the length of the DUT. Factors (i) and (ii) impose the practical limit of the TOF measurement and the condition, RC time constant τ_{rc} << transit time t_{tr} << deep trapping lifetime τ_D, must be embraced in order to obtain a reliable and accurate transient current measurement. Factors (iii) to (v) induce spatial variation on the drift velocity which ultimately yields fluctuation in current level that could lead to current noise. Nevertheless, the variation in drift velocity does not necessarily smear out the step-like current level at the transit time. Factor (vi) could be connected to various random processes, such as multiple-trapping, hoping and dispersion of charge carriers due to material inhomogeneity, which could result in the broadening of pulse width of charge carrier packet, reduction in current level and smearing of the step-like transit edge as shown in Figure 2.31.

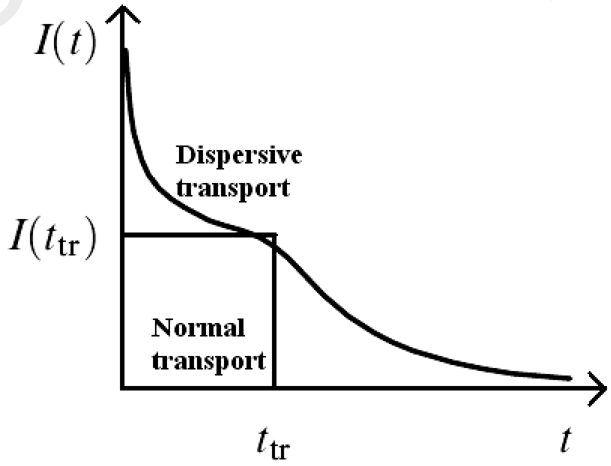

Figure 2.31: Step-like and dispersive current pulses obtained from TOF measurement. The step-like transient current indicates a packet of charge carriers is drifting with a constant velocity until it leaves the DUT at transit time.

Consequently, the transit time of a dispersive current pulse is determined from the intersecting point of the asymptotic currents at the short and long times of the double-log plot of normalised current-time curve as shown in Figure 2.32. Transient current is represented by an asymptotic power-law function which is given by

$$I(t) \propto \begin{cases} t^{-(1-\alpha)}, t < t_{tr} \\ t^{-(1+\alpha)}, t > t_{tr} \end{cases}, \tag{2.68}$$

where α represents the dispersive or disorder parameter of the material, $0 < \alpha \leq 1$. Besides, Scher & Montroll (1975) have developed an anomalous transport model based on the CTRW theory in order to describe the long-tail behaviour of the transient current.

If the measurement is performed on ordered, crystalline or semiconductor material, the mobility is calculated as, (Scher & Montroll, 1975),

$$\mu = \frac{L^2}{t_{tr} V_a}, \tag{2.69}$$

where μ is the mobility of charge carrier, V_a is the applied bias and t_{tr} is the transit time. On the other hand, if the measurement is performed on disordered, amorphous or organic semiconductor material, the mobility is calculated as

$$\mu = \left(\frac{L^2}{t_{tr} V_a} \right)^{\alpha}. \tag{2.70}$$

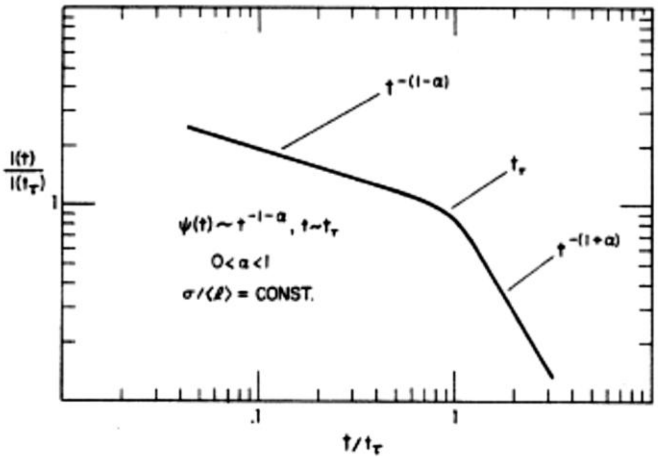

Figure 2.32: A double-log plot of transient photocurrent associated with a packet of charge carriers moving in an electric field, with a hopping-time distribution function $\psi(t) \sim t^{-1-\alpha}$, $0 < \alpha < 1$, towards an absorbing barrier at the sample surface. (Scher & Montroll, 1975)

2.8.2 Continuous-time random walk theory

Scher and Montroll (1975) derived a continuous-time random walk model which could explain the important features of the transient photocurrent measured by TOF measurement in amorphous materials. The CTRW model assumes that (i) the transport dynamic is a series of charge carrier (random walker) hopping from one localised site to another empty site, (ii) each hopping event happens independently, (iii) the hopping time, time interval between two successive hopping events, is an independent and identically distributed (iid) random variable which is characterised by a hopping-time distribution function that takes the form of a board power-law distribution, and (iv) the hopping sites are distributed randomly and thus the structural and energy disorder of the material are incorporated into the board power-law distribution.

CTRW process is described by the generalised master equation for PDF of just arriving at position *x* at time *t* from *x'* and *t'* (Metzler & Klafter, 2000c, 2004),

$$\eta(x,t) = \int_{-\infty}^{\infty} dx' \int_{0}^{\infty} \eta(x',t')\psi(x-x',t-t')dt' + \delta(x)\delta(t), \qquad (2.71)$$

where $n(x',t')$ is the PDF of having just arrived at position x' at time t' and $\delta(x)\delta(t)$ represents the initial condition of random walker. The PDF of being in x at time t, $W(x,t)$, is given by

$$W(x,t)=\int_0^t \eta(x,t')\Psi(t-t')dt, \tag{2.72}$$

which the particle has previously arrived on the site x at time t' and then does not jump away to other site since time t'. The second term in Equation (2.72) is the cumulative jump probability within $(0,t)$ which is given as

$$\Psi(t)=1-\int_0^t w(t')dt', \tag{2.73}$$

where the second term in Equation (2.73) is the probability of no jump event within the time interval $(0, t)$. By taking the Laplace transform on time and the Fourier transform on position, the PDF $W(x,t)$ in the Fourier-Laplace space is written as

$$W(k,u)=\frac{1-w(u)}{u}\frac{W_0(k)}{1-\psi(k,u)}, \tag{2.74}$$

where $W_0(k)$ is the Fourier transform of the initial condition $W_0(x)$.

The decoupled jump PDF could be written as

$$\psi(x,t)=w(t)\lambda(x), \tag{2.75}$$

where $w(t)$ is the waiting time PDF which is defined as

$$w(t)=\int_{-\infty}^{\infty}\psi(x,t)dx, \tag{2.76}$$

and $\lambda(x)$ is the jump length PDF which is defined as

$$\lambda(x) = \int_0^\infty \psi(x,t)\,dt\,. \tag{2.77}$$

Different types of CTRW processes can be obtained via the characteristic waiting time τ_c and jump length variance Σ^2 which are written respectively as

$$\tau_c = \int_0^\infty t w(t)\,dt\,, \tag{2.78}$$

$$\Sigma^2 = \int_{-\infty}^{\infty} x^2 \lambda(x)\,dx\,. \tag{2.79}$$

If both the characteristic waiting time and jump length variance are finite, Brownian motion could be obtained at the long-time limit.

(a) ***Fractional diffusion equation based on CTRW with long rests***

For anomalous diffusion with long rests, one can set the jump length variance to be finite but the characteristic waiting time is diverging, which reflects the existence of deep trap centres. In this particular case, the waiting time PDF takes the form of an asymptotic long-tail distribution and the jump length PDF takes a Gaussian distribution as given by Equation (2.80) and Equation (2.82), respectively. The waiting time PDF takes the form of

$$w(t) \sim A_\alpha \left(\tau/t\right)^{1+\alpha}\,, \tag{2.80}$$

for $0 < \alpha < 1$, $t \geq \tau$, $\tau = \tau_c$ and the characteristic waiting time diverges, $\tau_c \to \infty$. The Laplace transform of $w(t)$ in Equation (2.80) is given by

$$w(u) \sim 1 - (u\tau)^\alpha\,. \tag{2.81}$$

The jump length PDF takes the form of

$$\lambda(x)=\frac{1}{\sqrt{4\pi\sigma^2}}\exp\left(-\frac{x^2}{4\sigma^2}\right), \tag{2.82}$$

where $2\sigma^2 = \Sigma^2$ is the jump length variance and its Fourier transform is given by

$$\lambda(k)\sim 1-\sigma^2k^2+\mathrm{O}\left(k^4\right). \tag{2.83}$$

By using Equation (2.81) and Equation (2.83) in Equation (2.74), thus, the PDF $W(x,t)$ in Fourier-Laplace space is written as

$$W(k,u)=\frac{W_0(k)/u}{1+K_\alpha u^{-\alpha}k^2}, \tag{2.84}$$

where $K_\alpha = \sigma^2/\tau^2$ is the anomalous diffusion coefficient with unit of $\mathrm{cm}^2\mathrm{s}^{-\alpha}$. By using the following identities,

$$L\left\{{}_0D_t^{-\alpha}f(t)\right\}=u^{-\alpha}f(u), \tag{2.85}$$

$$F\left\{d^2f(x)/dx^2\right\}=-k^2f(k), \tag{2.86}$$

and obtaining the inverse Laplace and Fourier transforms of $W(x,t)$, one obtains the integral form of the FDE (Barkai et al., 2000; Metzler & Klafter, 2000c) as

$$W(x,t)-W_0(x)={}_0^{RL}D_t^{-\alpha}K_\alpha\frac{\partial^2}{\partial x^2}W(x,t). \tag{2.87}$$

Differentiate $W(x,t)$ with respect to time, $\partial W(x,t)/\partial t$, the differential form of the FDE (Wyss, 1986) is resulted as

$$\frac{\partial}{\partial t}\left[W(x,t)-W_0(x)\right]={}_0^{RL}D_t^{1-\alpha}K_\alpha\frac{\partial^2}{\partial x^2}W(x,t), \tag{2.88}$$

where the operator ${}_0^{RL}D_t^{1-\alpha}=\left(\partial/\partial t\right){}_0^{RL}D_t^{-\alpha}$ is defined by the RL fractional derivative as

$${}_0^{RL}D_t^{1-\alpha}f(x,t)=\frac{1}{\Gamma(\alpha)}\frac{\partial}{\partial t}\int_0^t\frac{f(x,t')}{\left(t-t'\right)^{1-\alpha}}dt'. \tag{2.89}$$

The Riemann-Liouville fractional derivative of an arbitrary power t^p is defined as

$${}_0^{RL}D_t^{\alpha}t^p=\frac{\Gamma(1+p)}{\Gamma(1+p-\alpha)}t^{p-\alpha}. \tag{2.90}$$

Thus, with Equation (2.90), the integral form of the FDE can be rewritten in its fractional derivative form as

$${}_0^{RL}D_t^{\alpha}W(x,t)-K_\alpha\frac{\partial^2}{\partial x^2}W(x,t)=\frac{t^{-\alpha}}{\Gamma(1-\alpha)}W_0(x). \tag{2.91}$$

The initial value $W_0(x)$ seems to decay in the manner of inverse power-law form and slower than that of the standard diffusion. Besides, if $\alpha \to 1$, the FDE reduces to the standard Fick's diffusion equation. The MSD is obtained through

$$\left\langle x^2(t)\right\rangle=\lim_{k\to 0}\frac{d^2W(k,u)}{dk^2}, \tag{2.92}$$

and then performing the inverse Laplace transform on Equation (2.84). Thus, the mean square displacement of anomalous diffusion with power-law waiting time distribution is resulted as

$$\left\langle x^2(t)\right\rangle=\frac{2K_\alpha}{\Gamma(1+\alpha)}t^\alpha. \tag{2.93}$$

(b) ***Fractional diffusion equation based on CTRW with Lévy flights***

For diffusion with Lévy flights (long jumps), one can set the jump length variance to be diverging but the characteristic waiting time is finite. This diffusion has Markovian behaviour due to the finiteness of the characteristic waiting time. In this case, the waiting time PDF takes a Poisson distribution and the jump length PDF takes a Lévy distribution with the asymptotic behaviour as given by Equation (2.94) and Equation (2.96), respectively. The waiting time PDF is defined as (Metzler & Klafter, 2000c),

$$w(t) = \frac{1}{\tau \exp(t/\tau)}, \tag{2.94}$$

where $\tau = \tau_c$ and its Laplace transform is given by

$$w(u) \sim 1 - u\tau + \mathrm{O}\left(\tau^2\right). \tag{2.95}$$

The jump length PDF takes the asymptotic form of

$$\lambda(x) \sim \frac{A_{\alpha_s}}{\sigma^{\alpha_s} |x|^{1+\alpha_s}}, \tag{2.96}$$

for $1 < \alpha_s < 2$, $|x| \gg \sigma$ and its Fourier transform is given by

$$\lambda(k) = \frac{1}{\exp\left(\sigma^{\alpha_s} |k|^{\alpha_s}\right)} \sim 1 - \sigma^{\alpha_s} |k|^{\alpha_s}. \tag{2.97}$$

By using Equation (2.95) and Equation (2.96) in Equation (2.74), thus, the PDF $W(x,t)$ in Fourier-Laplace space is written as

$$W(k,u) = \frac{1}{u + K^{\alpha_s} |k|^{\alpha_s}}, \tag{2.98}$$

where $K^{\alpha_s} \equiv \sigma^{\alpha_s} / \mu$ is the anomalous diffusion coefficient with unit of $\mathrm{cm}^{\alpha_s}\mathrm{s}^{-1}$. By performing inverse Fourier transform and then Laplace transform, the space-fractional diffusion equation due to Lévy flight is obtained as

$$\frac{\partial W}{\partial t} = K^{\alpha_s}\, {}_{-\infty}^{W}D_x^{\alpha_s} W(x,t), \tag{2.99}$$

where ${}_{-\infty}^{W}D_x^{\alpha_s}$ is the Weyl fractional differential operator in one dimension which is same as the Riesz fractional differential operator. Equation (2.99) could be solved using the Fox function. Figure 2.33 shows the comparison of the trajectories of a Brownian motion and Lévy flight with fractal dimension $D_f = 1.5$ for about 7000 steps. The Lévy flight can be viewed as a local motion sporadically interrupted by a long break on all length scales which leads to the formation of clustering of trajectory before a long jump occurs. The trajectory of Lévy flight could also be characterised by the fractal dimension.

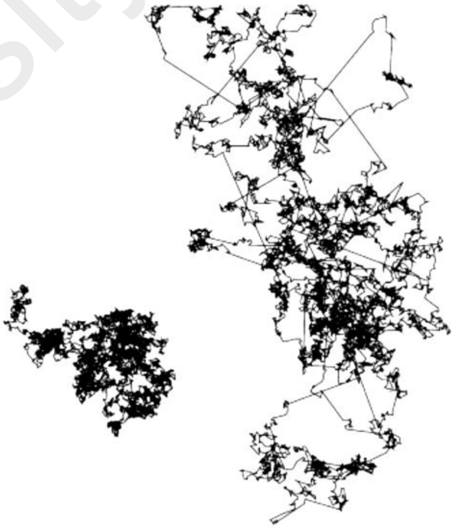

Figure 2.33: Comparison between the trajectories of Brownian motion (left) and Lévy flight at $D_f = 1.5$ (right) for about 7000 steps. (Metzler & Klafter, 2000c)

(c) Fractional diffusion equation based on CTRW with long rests and Lévy flights

When both the characteristic waiting time and jump length variance become infinite, the propagation of a random walker is characterised through broad PDFs and the space-time fractional diffusion equation would be resulted as (Metzler & Klafter, 2000c),

$$\frac{\partial W}{\partial t} = {}_{0}^{RL}D_t^{1-\alpha} K_\alpha^{\alpha_s} \, {}_{-\infty}^{W}D_x^{\alpha_s} W\left(x,t\right), \tag{2.100}$$

where $K_\alpha^{\alpha_s} = \sigma^{\alpha_s} / \tau^\alpha$, ${}_{-\infty}^{W}D_x^{\alpha_s}$ is the RL time-fractional differential operator and ${}_{-\infty}^{W}D_x^{\alpha_s}$ is the Weyl space-fractional differential operator. The pseudo MSD is defined as

$$\left\langle x^2\left(t\right)\right\rangle_L \sim t^{2\alpha/\alpha_s}, \tag{2.101}$$

which indicates that particle spreads finitely in a space in a given time interval.

(d) Fractional Langevin equation

Fractional Langevin equation is generalised from the LE to take into account for the damping effect due to an additional frictional force, which depends on the memory of the particle acceleration, to the Stokes drag force. The additional frictional force is called the Basset force (Basset, 1888; Mainardi & Pironi, 1996) and is given by

$$F_\upsilon = -\frac{9}{2\chi_{FLE}} m \left[\frac{1}{\tau_{0-FLE}} \nu\left(t\right) + \frac{1}{\sqrt{\tau_{0-FLE}}} B\left(t\right) \right], \tag{2.102}$$

where $\nu(t)$ is velocity of particle, m is the mass of particle,

$$\tau_{0-FLE} = \frac{r_a^2}{\eta}, \quad \chi_{FLE} = \frac{\rho_p}{\rho_f}, \tag{2.103}$$

η is the viscosity of the liquid, r_a is the radius of the particle, ρ_p is the density of particle, ρ_f is the density of liquid and $B(t)$ is given as

$$B(t) := \frac{1}{\sqrt{\pi}} \int_{-\infty}^{t} \frac{d\nu(t)/ds}{\sqrt{t-s}}\, ds = \frac{1}{\Gamma(1/2)} \int_{0^-}^{t} \frac{d\nu(t)/ds}{\sqrt{t-s}}\, ds \,. \tag{2.104}$$

By using the RL fractional derivative of order ½, Equation (2.104) can be rewritten as

$$B(t) = {}_{0}^{RL}D_t^{1/2}\nu(t) = -\frac{t^{-3/2}}{2\sqrt{\pi}}\nu(t)\,. \tag{2.105}$$

Thus, the FLE is resulted as

$$\frac{d\nu(t)}{dt} = -\frac{1}{\sigma_e}\left[1 + \sqrt{\tau_{0-FLE}}\; {}_{0}^{RL}D_t^{1/2}\right]\nu(t) + \frac{1}{m_e}R(t)\,, \tag{2.106}$$

where $R(t)$ is the random fluctuating force and the damping effect of the frictional force is given by the new friction coefficient as

$$\zeta_{FLE}(t) = \frac{1}{\sigma_e}\left[\delta(t) - \sqrt{\tau_{0-FLE}}\,\frac{t^{-3/2}}{2\sqrt{\pi}}\right], \tag{2.107}$$

with an additional fractional noise associated to the term $t^{-3/2}$ in addition to the white noise in the standard LE. The mobility of the particle is written as

$$\mu = \frac{\sigma_{FLE}}{m} = \frac{\sigma_e}{m_e}\,, \tag{2.108}$$

where

$$\frac{1}{\mu} = 6\pi r_a \rho_f \eta = \frac{9m}{2\chi_{FLE}\tau_{0-FLE}}\,, \qquad \sigma_{FLE} = \frac{2}{9}\chi_{FLE}\tau_{0-FLE}\,, \tag{2.109}$$

and $1/\sigma_{FLE} = \zeta_{LE}/m$ is the friction coefficient per unit mass.

The FLE in Equation (2.106) is a special case of the generalised Langevin equation reported in (Kubo 1966), in which the GLE is written as

$$\frac{d\upsilon(t)}{dt} = -\int_0^t \zeta_{GLE}(t-s)\upsilon(t)ds + \frac{R(t)}{m}, \qquad (2.110)$$

where the memory effect of the particle acceleration is incorporated.

(e) Fractional diffusion equation based on fractional calculus

The fractional diffusion equation could be generalised from the standard diffusion equation (Section 2.6(a)) using the fractional calculus as reported in several studies (Balakrishnan, 1985; Schneider & Wyss, 1989; Wyss, 1986). It is done by replacing the first order time derivative of the standard diffusion equation with the α-order fractional time integral. The FDE is given by

$$\frac{\partial^{1-\alpha}P(x,t)}{\partial t^{1-\alpha}} = D_\alpha \frac{\partial^2 P(x,t)}{\partial x^2}, \qquad (2.111)$$

where $\partial^{1-\alpha}/\partial t^{1-\alpha}$ is the fractional integral operator and $0 < \alpha \leq 1$.

(f) Fractional Fokker-Planck equation based on fractional calculus

Under the influence of external force, for instance electric field, the transport of charge carriers in disordered material is now subjected to the external force and described by the FFPE. The fractional Fokker-Planck equation uses the probability, instead of using the charge carrier density as in the FDDE, to represent the position x of charge carrier at time t. The probability current $j_{FP}(x,t)$ density incorporated with an external electric field $F(x,t)$ is given by (Sokolov et al., 2002),

$$j_{FP}(x,t) = D\frac{\partial p(x,t)}{\partial x} - \mu F(x,t)\, p(x,t), \qquad (2.112)$$

where $P(x,t)$ is the probability of finding charge carrier at x and time t, D is the diffusion coefficient and μ is the mobility. Substitute Equation (2.112) in the continuity equation, one gets the FPE as

$$\frac{\partial p(x,t)}{\partial t} = D\frac{\partial^2 p(x,t)}{\partial x^2} - \mu\frac{\partial}{\partial x}\left[F(x,t)\,p(x,t)\right]. \qquad (2.113)$$

By using the RL fractional derivative, one can generalise the FPE equation to the FKKE as

$$\frac{\partial p(x,t)}{\partial t} + \frac{\partial^{1-\alpha}}{\partial t^{1-\alpha}}\left\{\frac{\partial}{\partial x}\left[\mu_\alpha F(x,t)\,p(x,t)\right] - D_\alpha\frac{\partial^2 p(x,t)}{\partial x^2}\right\} = 0, \qquad (2.114)$$

where D_α and μ_α are the fractional diffusion coefficient and fractional mobility, respectively. The ratio of $D_\alpha/\mu_\alpha = k_BT$ gives the generalised Einstein's relationship.

CHAPTER 3: RESEARCH METHODOLOGY

Organic field-effect transistors based on P3HT are fabricated in order to obtain the transient current noise for scaling analysis. Hence, this chapter provides some details on the fabrication and electrical characterisations of OFET. The fractal analysis methods which will be used to analyse the transient current noise are documented herein. Anomalous charge transport theory incorporated with multiple-trapping which is deduced using the fractional calculus and the numerical methods used to solve the transport equations are demonstrated in this chapter. Lastly, transient current calculation and simulation procedures of charge transport are presented.

3.1 Fabrication of organic field-effect transistor and current-voltage measurement

Top-contact and bottom-gate OFETs were fabricated in order to study charge carrier transport dynamics through their behaviour of noise. A 100 nm thick SiO_2 layer is grown on top of an *n*-type silicon substrate to serve as the dielectric layer. The active layer of the device is made of P3HT. P3HT is dissolved in chloroform and is spin-coated on top of the dielectric layer. The structure of the P3HT OFET is depicted in Figure 3.1. P3HT is chosen in this study simply due to its high charge carrier mobility and commercial availability. The P3HT active layer is thermally treated at 120 °C for ten minutes. The source and drain electrodes are deposited with a 50 nm thick gold on top of the P3HT active layer. The channel width (arranged in interdigitated design) and length are 11.2 mm and 40 µm, respectively.

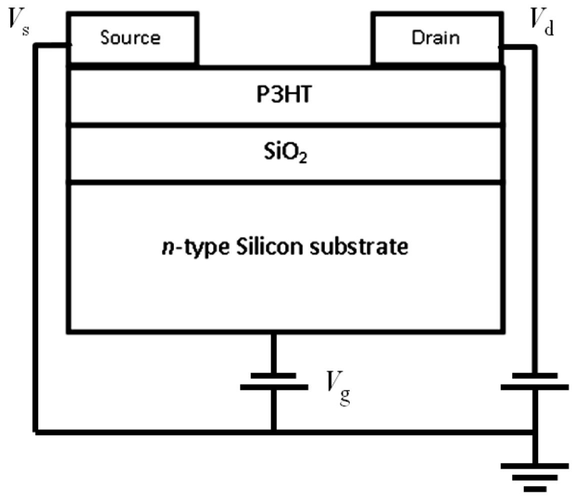

Figure 3.1: Top-contact and bottom-gate P3HT OFET structure and setup of current-voltage measurement.

Two Keithley SMUs are connected to the source, drain and gate contacts of the OFET as shown in Figure 3.1. The drain currents are then measured for source-drain voltage ranging from 0 to −60 V with respect to different gate voltages in order to obtain the current-voltage characteristic of the OFET. Low noise coaxial cable is used to minimise the triboelectric noise which is induced from the relative movement between the dielectric and shielding layers of the cable. The measurement setup is placed in a grounded metal box so that it is shielded from the electromagnetic interference radiating from open space. Since the device is biased and measured using SMUs, thus power line noise is superimposed on the noise of the SMUs which yields a sub-nanoampere noise floor. Nevertheless, the current measured from the devices are ranging from microamperes to sub-miliamperes, hence the noise floor of SMUs is insignificant as compared to the currents resulted from devices. Activation energy of P3HT organic semiconductor with low mobility (~10^{-4} cm^2/Vs) is around 300 meV (Craciun, 2011), thus thermal noise generation at room temperature could be negligible during the measurement.

3.2 Low-frequency noise measurement

Low-frequency noise measurement is a common technique used to characterise the noise behaviour and reliability of a device. This is because this technique is sensitive enough to probe the microscopic properties, such as the surface defects, interface defects, bulk defects and generation-recombination centres, of a device. Figure 3.2 shows a setup for the low-frequency noise measurement which consists of a current amplifier, a dynamic signal analyser or a power spectrum analyser, a digital multimeter, an oscilloscope and one or two source-measurement unit(s). The current amplifier is used to amplify the current noise resulted from the DUT and then feeds it into the DSA. Power spectral density of the current noise is computed in the DSA and then recorded in a personal computer. The current noise is also measured with a DMM and monitored by an OSK during the measurement. For very low current level measurement, a pre-amplifier is connected between the DUT and the current amplifier to sense and pre-amplify the low current which is resulted from the DUT before it is fed into the current amplifier.

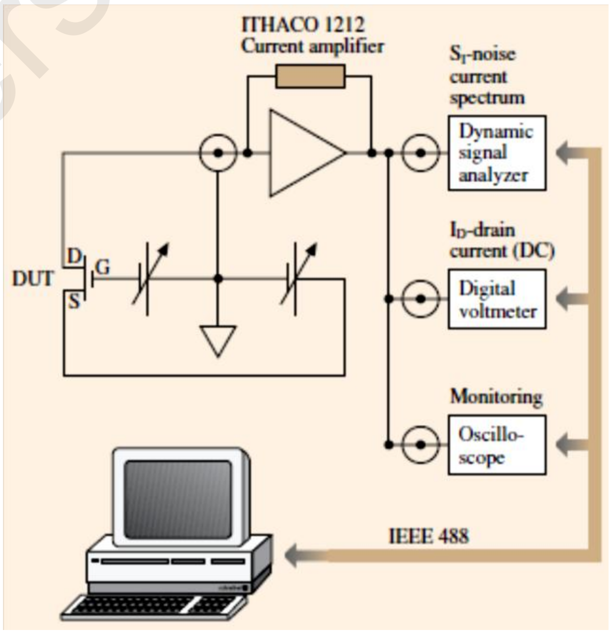

Figure 3.2: System for measuring low-frequency noise. (Kasap & Capper, 2006)

All instruments used in the setup must have very low-noise level so that the current resulted from the DUT could be easily measured. Proper grounding and shielding of the setup are required to reduce the noise generated from the power-line and electromagnetic waves coming from surrounding environment that might interfere with the DUT. Besides, the impedances between the DUT, probes, connectors, cables and measurement instruments must be matched to avoid any lost or degradation of the measured current noise. In view of all the stringent requirements needed for the setup, thus the low-frequency noise measurement is expensive to be implemented and experienced personnel is required in order to obtain an accurate measurement.

When charge carriers are moving in a small device, they will encounter smaller amount of trap centres as compared to that of large device. The trapping and releasing of charge carrier from a trap centre causes random fluctuation of charge carriers which eventually results a current that behaves like a random telegraph signal. A RTS produces a single generation-recombination spectrum (represented by the dash lines in Figure 3.3) and also serves as the fundamental component of the 1/*f* noise. In contrast, charge carriers are encountering larger amount of trap centres while they are moving in a large device. Thus, charge carriers are experiencing a greater amount of trapping and releasing events, eventually, a 1/*f* current noise is resulted as shown in Figure 3.3.

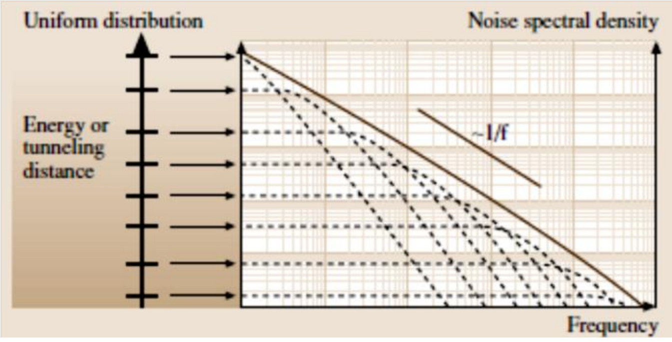

Figure 3.3: 1/*f* noise spectra due to cumulative sum of generation-recombination noise. (Kasap & Capper, 2006)

An alternative method is proposed in this work to analyse the current noise using its time domain which requires much simple and cheaper measurement setup. Two Keithley 236 SMUs, represented by the battery symbol as shown in Figure 3.4, are used to bias the device and measure the current resulted from the device, where one unit of the SMUs is used to establish the source-drain voltage V_{ds} and measure the drain current I_{ds} while another unit of SMU is used to supply the gate voltage V_g and measure the gate current I_g. In order to obtain the temporal evolution of (transient) currents, devices are repetitively biased using the sweep function of the SMU while the resulted currents are measured during a fast integration time of 416 μs. The measured currents in time domain are then stored in the buffer (maximum of 1000 readings) of the SMUs before they are recorded in a desktop computer for subsequent noise analysis using the conventional PSD method and the more robust DFA approach. Power spectral density of the transient current is numerically computed by taking the squared modulus of fast-Fourier transform of the transient current. This can be effortlessly done with the FFT subroutine available in the MATLAB program.

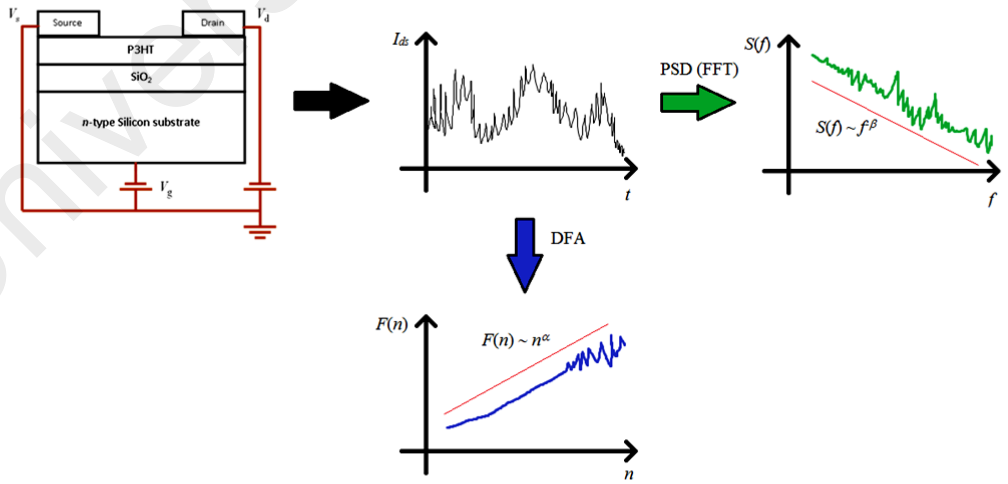

Figure 3.4: Current noise analysis based on PSD method and DFA.

3.3 Fractal analysis of current noise

This section provides the description of the fractal analysis method, namely power spectral density method and detrended fluctuation analysis, used to analyse the current noises of OFET measured at various source-drain voltages.

3.3.1 Power spectral density method

The low frequency noise analysis using the power spectra density method is implemented by computing the squared modulus of Fourier transformed of the measured transient current noise. If a time series exhibits power-law scaling the PSD would take the following form

$$S(f) \sim \frac{1}{f^{\beta_{PS}}}, \tag{3.1}$$

where $S(f)$ is the power spectral density and f is the frequency.

The slope of the log-log plot of the PSD yields the scaling exponent β_{PS}. One can link the scaling exponent β_{PS} to the Hurst exponent H if the underlying transport mechanism is described by the FBM. The scaling exponent β_{PS} gives useful information of the transport dynamics of the charge carriers hopping in the organic or polymer material of OFETs and also information on trap centres and defects. The presence of trap centres and defects could induce generation-recombination noise and $1/f$ noise in the devices that sets a maximum limit on the performance of the devices (Jurchescu et al., 2008; Ke et al., 2006, 2008; Xu et al., 2010). The occurrence of $1/f$ noise in a device could be observed at the low frequency region of the current noise PSD in which the PSD is inversely proportional to the frequency. In addition, it has been demonstrated in (Brophy, 1968, 1969; Huo et al., 2003; Nelkin & Harrison, 1982) that the nonstationary effect is naturally present in the current noise despite of the influence of the finite sampling size effect of the time series. Huo et al. (2003) has also shown that the power spectrum of the current noise follows a fractal power-law scaling or 1/*f* type behaviour in which the scaling exponent of the power spectrum varies in the range of $1 < \beta_{PS} < 2$. This is associated to the density of trap centres and the probability distribution of release rates that varies slowly with frequency (Nelkin & Harrison, 1982). The relationship of the scaling exponent β_{PS} and the Hurst exponent is given as $\beta_{PS} = 2H + 1$.The current noise can also be classified as uncorrelated white noise when $\beta_{PS} = 0$ ($H = -0.5$), 1/*f* noise ($H = 0$) and Brownian noise when $\beta_{PS} = 2$ ($H = 0.5$).

3.3.2 Detrended fluctuation analysis

The detrended fluctuation analysis is a statistical method that has been developed to study the existence of short-rage or long-range correlation of time series. This method was first used to study DNA sequences (Peng et al., 1994) and progressively found its applications in other time series analysis such as that of the electrocardiogram analysis (Huikuri et al., 2009; Meyer & Stiedl, 2003; Peng et al., 1995), electroencephalogram analysis (Ignaccolo et al., 2010; Lee et al., 2004; Penzel et al., 2003), weather forecasting (Matsushita et al., 2007) and electrical noise study in semiconductor devices (Houssa et al., 1998; Shiau, 2011). Detrended fluctuation analysis has been proven to be a robust technique in time series analysis due to the capability of detecting whether a trend is superimposed on a time series (Hu et al., 2001) and the capability of differentiating stationary and nonstationary properties inherent in a time series (Chen et al., 2002). This method contains few important steps (Peng et al., 1994, 1995; Penzel et al., 2003) as outlined in the following paragraphs. As shown in the Figure 3.5, the time series $x(i)$ is first subtracted from the mean value $<x>$ and then integrated as given by,

$$Y(j) = \sum_{i=1}^{j} x(i) - \langle x \rangle \,. \tag{3.2}$$

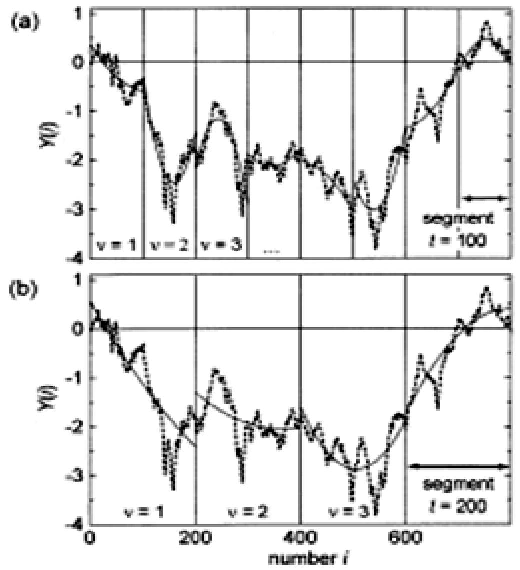

Figure 3.5: Detrending procedure of DFA at different window sizes. (Penzel et al., 2003)

The integrated time series $Y(j)$ is then divided into boxes of equal length n_{DFA}. The next step involves fitting a linear least-squares line in each box of length n_{DFA} in which it reflects the local trend in that box and its y-coordinate of the local trend is represented by $Y_{fit}(j)$. The integrated time series $Y(j)$ is then detrended via subtracting it from the local trend $Y_{fit}(j)$ of each box. The average fluctuation $F(n_{DFA})$ or the root-mean square of the difference between $Y(j)$ and $Y_{fit}(j)$ is computed as

$$F\left(n_{DFA}\right)=\sqrt{\frac{1}{N}\sum_{j=1}^{N}\left[Y\left(j\right)-Y_{fit}\left(j\right)\right]^{2}}\ , \tag{3.3}$$

where N is the length of the time series. The average fluctuation $F(n_{DFA})$ is then re-calculated for all box sizes leading to the power-law behaviour, $F\left(n_{DFA}\right)\sim n_{DFA}^{\alpha_{DFA}}$, if $x(i)$ is a fractal noise. As shown in Figure 3.6, the slope of linear scaling regime of the log-log plot of $F(n_{DFA})$ versus n_{DFA} gives the scaling exponents α_{DFA} which can then be used to deduce the correlation behaviour of fractal noises.

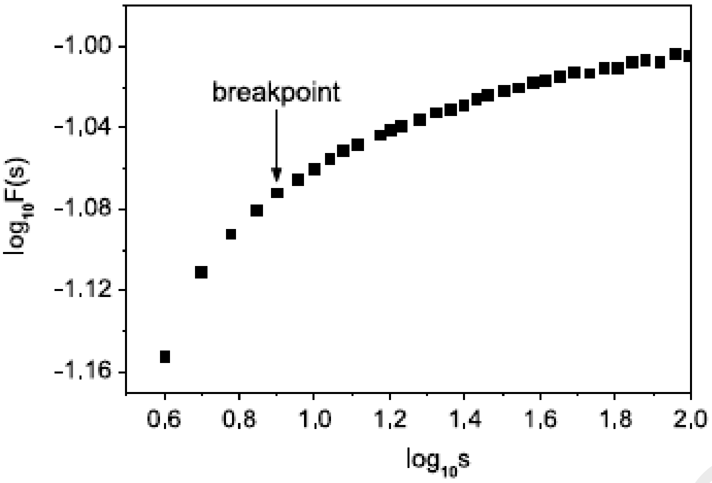

Figure 3.6: Double-log plot for r.m.s. fluctuation *F* versus box size. (Penzel et al., 2003)

One can link the scaling exponent α_{DFA} to the anomalous diffusion process such as the fractional Brownian motion where $\alpha_{DFA} = H + 1$. When $\alpha_{DFA} = 0.5$, the integrated time series is associated with random walk whose original time series does not present any correlation between two events. This is the standard characteristic of white noise. The time series is said to be persistent with long memory effect when $0.5 < \alpha_{DFA} < 1$. On the other hand, anti-persistent time series exhibits short memory effect and in this case, $0 < \alpha_{DFA} < 0.5$. If $\alpha_{DFA} = 1$ ($H = 0$), time series is identified as having the characteristic of $1/f$ noise. Finally, when $\alpha = 1.5$ ($H = 0.5$), the integrated time series is considered as a Brownian noise.

3.4 Transport equation based on fractional calculus

This section provides the description of the transport equation used in this work to model the anomalous transport in disordered organic semiconductor and the numerical techniques used to obtain the solutions of the transport equation.

3.4.1 Fractional kinetic equation with multiple-trapping mechanism

Based on multiple-trapping model, photo-generated charge carriers in disordered material are classified into trap (localised) and free (delocalised) charge carriers. Trap charge carrier is the charge carrier which is captured in localised state and free charge carrier is the charge carrier which is freely hopping from one trap centre (localised state) to another trap centre. The movement of free charge carriers is subjected to phonon scatterings and external electric field that cause the charge carriers to drift with a finite average velocity. The capture rate of charge carrier into the localised state is linearly proportional to the number of free charge carrier density. Trap charge carrier density is assumed to be higher than the free charge carrier density and the average time of delocalisation is approaching zero, $\tau_0 \to 0$. The total charge carrier density, $p(x,t)$ is the sum of the trap, $p_t(x,t)$, and free, $p_f(x,t)$, charge carrier densities at x and t which is given as

$$p(x,t) = p_t(x,t) + p_f(x,t). \qquad (3.4)$$

As demonstrated in (Sibatov & Uchaikin, 2007, 2009), the relationship between the time rate of change of trap and free charge carrier densities, derived based on an asymptotically power-law distribution function for the random residence time in the localised states, is given as

$$\frac{\partial p_t(x,t)}{\partial t} = \left(\tau_0 c^{\alpha}\right)^{-1} \frac{1}{\Gamma(1-\alpha)} \frac{\partial}{\partial t} \int_0^t \frac{p_f(x,s)}{(t-s)^{\alpha}} ds$$

$$\frac{\partial p_t(x,t)}{\partial t} = \left(\tau_0 c^{\alpha}\right)^{-1} \frac{\partial^{\alpha} p_f(x,t)}{\partial t^{\alpha}}, \qquad (3.5)$$

where $\partial^{\alpha}/\partial t^{\alpha}$ is the RL fractional derivative of order $0 < \alpha < 1$ which is an integral-differential operator (Podlubny, 1998).

In the present of an applied electric field, the one-dimensional continuity equation of the free charge carrier is given as

$$\begin{aligned}&\frac{\partial p_f\left(x,t\right)}{\partial t}+\frac{1}{c^{\alpha}\tau_0}\frac{\partial^{\alpha} p_f\left(x,t\right)}{\partial t^{\alpha}}+\frac{\partial}{\partial x}\left[\mu F\left(x,t\right)p_f\left(x,t\right)\right]-\\&D\frac{\partial^2 p_f\left(x,t\right)}{\partial x^2}=p\left(x,0\right)\delta\left(t\right),\end{aligned}\tag{3.6}$$

where $p(x,0)\delta(t)$ is the initial photo-generated charge carriers. By assuming that most of the charge carriers are trapped in the localised states, $p(x,t) \approx p_t(x,t)$, and substituting Equation (3.5) into Equation (3.6), one could rewrite Equation (3.6) for the continuity equation of the total charge carrier density as

$$\frac{\partial p\left(x,t\right)}{\partial t}+\frac{\partial^{1-\alpha}}{\partial t^{1-\alpha}}\left\{c^{\alpha}\tau_0\frac{\partial}{\partial x}\left[\mu F\left(x,t\right)p\left(x,t\right)\right]-c^{\alpha}\tau_0 D\frac{\partial^2 p\left(x,t\right)}{\partial x^2}\right\}=p\left(x,0\right)\delta\left(t\right).\tag{3.7}$$

By applying RL fractional integral operator of order $1-\alpha$ to Equation (3.7), the continuity equation of the total charge carrier density can be written as

$$\frac{\partial^{\alpha} p\left(x,t\right)}{\partial t^{\alpha}}+\frac{\partial}{\partial x}\left[K_{\alpha}\left(x,t\right)p\left(x,t\right)\right]-D_{\alpha}\frac{\partial^2 p\left(x,t\right)}{\partial x^2}=p\left(x,0\right)\frac{t^{-\alpha}}{\Gamma\left(1-\alpha\right)},\tag{3.8}$$

where $K_{\alpha}(x,t) = c^{\alpha}l = c^{\alpha}\tau_0\mu F(x,t)$ is the anomalous advection coefficient, $D_{\alpha} = \tau_0 c^{\alpha}D$ is the anomalous diffusion coefficient, τ_0 is the average time of delocalisation (mean free time of a charge carrier moving between two successive entrapments), $l = \tau_0\mu F(x,t)$ is the average length of delocalisation, μ is the mobility and D is the diffusion coefficient that is calculated using the Einstein relationship $D = \mu k_{\mathrm{B}}T/e$ where e is the electronic charge, k_B is the Boltzmann constant and T is the temperature. The velocity of charge carrier is written as $v\left(x,t\right)=\mu F\left(x,t\right)$ where $F(x,t)$ is the localised electric field. The charge carrier capture coefficient $c=\omega_0\left[\sin\left(\pi\alpha\right)/\pi\alpha\right]^{1/\alpha}$ where ω_0 is the capture rate of charge carriers into the localised states and $\alpha = k_BT/E_0$ is the dispersive parameter which depends on the temperature T and the mean value E_0 of the exponential energy density of localised state of charge carrier. The dispersive parameter is also associated to the fractional derivative order α in Equation (3.5). The dispersive parameter, $\alpha(x,t)$, can also be expressed as a function of time, space or both time and space to represent the change of material property (i.e. energy disorder) of inhomogeneous materials. Thus, Equation (3.8) could be generalised to the one-dimensional variable-order time-fractional drift-diffusion equation which is written as

$$\frac{\partial^{\alpha(x,t)} p(x,t)}{\partial t^{\alpha(x,t)}} + \frac{\partial}{\partial x}\left[K_{\alpha(x,t)}(x,t)\, p(x,t)\right] - D_{\alpha(x,t)} \frac{\partial^2 p(x,t)}{\partial x^2} = p(x,0) \frac{t^{-\alpha(x,t)}}{\Gamma\left(1-\alpha(x,t)\right)}, \quad (3.9)$$

and representing the dispersive transport dynamics of charge carriers in organic semiconductors based on the multiple-trapping mechanism. It should be noted that the propagation of charge carriers will resemble the normal transport dynamics when $\alpha(x,t)$ is approaching 1.

It is known that the RL fractional derivative can be approximated using the GL fractional derivative in order to obtain the numerical solutions of the time-fractional diffusion equation as demonstrated in (Podlubny, 1998; Yang et al., 2009). However, the order of accuracy of the GL fractional derivative is below one and shifted version of the GL fractional derivative should be used in order to obtain stable solutions as pointed in (Sousa, 2012). Murio (2008b) also pointed out that the GL fractional derivative might only be consistent at all values of x and coincides with the Caputo fractional derivative if zero initial condition is fulfilled.

Nevertheless, several works (Lin & Xu, 2007; Murio, 2008a; Sun et al., 2012) had demonstrated a finite difference scheme to discretise the Caputo time fractional derivative and able to obtain unconditionally stable solutions for the time-fractional diffusion equation with $(2-\alpha)$ order accuracy in time. Solutions of the Caputo time-fractional diffusion equation are obtained through the integer order derivatives at all previous time steps. Thus, finite difference method used to discretise the integer order derivative could be readily adopted to discretise the Caputo time fractional derivative. This allows the past events of transport dynamics of charge carriers at all previous time steps to be naturally incorporated in the Caputo time fractional derivative. Besides, physical conditions could be represented by the boundary conditions of the Caputo time-fractional drift-diffusion equation. It is also known that the Caputo fractional derivative of a constant is zero but not the case for the RL fractional derivative.

3.4.2 Electric potential and field

The electric potential $V(x,t)$ is obtained via solving the self-consistent Poisson equation as given below,

$$\frac{\partial^2 V\left(x,t\right)}{\partial x^2} = -\frac{\rho\left(x,t\right)}{\varepsilon_r \varepsilon_0}, \tag{3.10}$$

where $\rho(x,t) = ep(x,t)$ is the charge density, ε_r is the relative permittivity of the material and ε_0 is the permittivity of vacuum. The localised electric field is then calculated as,

$$F\left(x,t\right) = -\frac{\partial V\left(x,t\right)}{\partial x}. \tag{3.11}$$

3.4.3 Current density

The average current density $I_T(t)$ is defined as the conduction current density averaged over the thickness of the device or TOF cell,

$$I_T\left(t\right) = \frac{e}{L}\frac{d}{dt}\int_0^L \left(x-L\right) p\left(x,t\right) dx, \tag{3.12}$$

where $p(x,t)$ is the total charge carrier density obtained by solving Equation (3.8) or Equation (3.9). Observe that current density is generally inversely related to the cell thickness *L*. Consequently, Equation (3.12) explicitly accounts for the influence of the film thickness in that the current density level decreases when the thickness of the film increases and vice versa.

3.5 Numerical methods

The anomalous transport dynamics of charge carriers in organic semiconductor materials are studied by using the fractional drift-diffusion equation derived based on the multiple-trapping mechanism (Sibatov & Uchaikin, 2009; Uchaikin & Sibatov, 2008, 2013). The integer order space derivative, integer time derivative and fractional time derivative are approximated by using the finite difference method as described in the subsequent sub-sections.

3.5.1 Finite difference scheme for integer order differential operator

The derivative of a function *f*(*x*) at *x*, based on the First Principle definition, is defined as

$$f^{'}\left(x\right)=\lim_{h\to 0}\frac{f\left(x+h\right)-f\left(x\right)}{h}, \tag{3.13}$$

where $h = \Delta x$ is the interval between x and $x + h$ (Burden & Faires, 2011). Due to the rounding-off error, two-point difference formula has an error of $\left(h/2\right)f^{(2)}\left(\xi\right)$ and ξ lies between x and $x + h$. In general, it is recommended that using more points in the approximation of the derivative of *f*(*x*) could improve the accuracy of the approximation. Thus, the three-point midpoint (central difference) formula for the first derivative, with equally space point, is written as

$$f^{'}\left(x\right)=\frac{1}{2h}\left[f\left(x+h\right)-f\left(x-h\right)\right]-\frac{h^{2}}{6}f^{(3)}\left(\xi\right), \tag{3.14}$$

where ξ lies between $x - h$ and $x + h$. By expanding the function $f(x)$ about a point x to the third Taylor polynomial and evaluate at $x - h$ and $x + h$, the three-point midpoint formula for the second derivative of $f(x)$ can be defined as

$$f''(x) = \frac{1}{h^2}\left[f(x-h) - 2f(x) + f(x+h)\right] - \frac{h^2}{12} f^{(4)}(\xi), \quad (3.15)$$

where ξ lies between $x - h$ and $x + h$. Equation (3.14) and Equation (3.15) can also be used for time variable t.

3.5.2 Finite difference scheme for fractional order differential operator

In view of the advantages offered by the Caputo fractional time derivative, thus the fractional time derivative in Equation (3.9) is expressed by using the Caputo fractional time derivative which is defined, for a function $f(x,t)$, as

$$\frac{\partial^{\alpha(x,t)} f(x,t)}{\partial t^{\alpha(x,t)}} = \frac{1}{\Gamma(1-\alpha(x,t))}\int_0^t \frac{\partial f(x,s)}{\partial s}\frac{ds}{(t-s)^{\alpha(x,t)}}, \quad 0 < \alpha(x,t) \le 1. \quad (3.16)$$

The variable-order Caputo fractional time derivative is discretised by using the implicit difference scheme due to its unconditional stable property. Let's define the position is $x_i = i\Delta x$ for $0 \le i \le N_x$, time is $t_k = k\Delta t$ for $0 \le k \le N_t - 1$, spatial step is $\Delta x = L/N_x$, time step is $\Delta t = T/N_t$, T is the total time, L is the device length, N_t is the total time step and N_x is the total spatial step. We can use the notation of $f(x_i, t_k) \approx f(i\Delta x, k\Delta t) = f_i^k$ to represent the approximation of an arbitrary function and α_i^k is fractional derivative order.

The variable-order fractional time differential operator, Equation (3.16), is approximated as (Lin & Xu, 2007; Sun et al., 2012),

$$\frac{\partial^{\alpha(x_i,t_{k+1})} f\left(x_i,t_{k+1}\right)}{\partial t^{\alpha(x_i,t_{k+1})}} = \frac{1}{\Gamma\left(1-\alpha\left(x_i,t_{k+1}\right)\right)} \sum_{m=0}^{k} \int_{t_m}^{t_{m+1}} \frac{\partial f\left(x_i,s\right)}{\partial s} \frac{ds}{\left(t_{k+1}-s\right)^{\alpha(x_i,t_{k+1})}} \tag{3.17}$$

$$= \frac{1}{\Gamma\left(1-\alpha_i^{k+1}\right)} \sum_{m=0}^{k} \frac{f_i^{m+1}-f_i^{m}}{\Delta t} \int_{t_m}^{t_{m+1}} \frac{ds}{\left(t^{k+1}-s\right)^{\alpha_i^{k+1}}} + O\left(\Delta t\right).$$

$$L^{\alpha_i^{k+1}} f_i^{k+1} = \frac{1}{\Gamma\left(2-\alpha_i^{k+1}\right)} \sum_{m=0}^{k} \frac{f_i^{k+1-m}-f_i^{k-m}}{\Delta t^{\alpha_i^{k+1}}} b_i^{m,k+1} \,. \tag{3.18}$$

where

$$b_i^{m,k+1} = \left(m+1\right)^{1-\alpha_i^{k+1}} - m^{1-\alpha_i^{k+1}} \,, m = 0,1,...,k, \tag{3.19}$$

and $b_i^{0,k+1} = 1$, $b_i^{m,k+1} \to 0$ as $m \to \infty$ and $O(\Delta t)$ is the approximation error. It should be noted that the results of the integer order time derivative of $f(x,t)$ at all the previous time steps are needed in order to implement the Caputo fractional derivative

3.5.3 Numerical integration

The definite integration of a function $f(x)$ in a close interval $[a, b]$ is given by Riemann sum as

$$\int_a^b f\left(x\right)dx \approx \lim_{N\to\infty}\left(\sum_{i=1}^{N} f\left(\frac{x_i+x_{i-1}}{2}\right)\cdot\left(x_i-x_{i-1}\right)\right), \tag{3.20}$$

where $f(x)$ is arbitrary function of x, x_i is the i-th point on the curve, and N is the total number of points. When $N \to \infty$, the R.H.S. of Equation (3.20) approximates the value of the definite integral of $f(x)$ over $[a, b]$.

The most basic numerical integration method is carried out by approximating the area under a curve over an interval $[a, b]$ using a trapezoid as depicted in Figure 3.7.

This method is called as Trapezoid Rule (Cheney & Kincaid, 2008) and its approximation is given as

$$\int_a^b f(x)\,dx \approx \frac{1}{2}(b-a)\left[f(a)+f(b)\right], \tag{3.21}$$

with the error term as

$$-\frac{(b-a)^3}{12} f^{(2)}(\xi), \tag{3.22}$$

for some ξ in (a, b) and $f^{(2)}(\xi)$ is the second derivative of $f(\xi)$ which yields the Trapezoid Rule to be second order accurate.

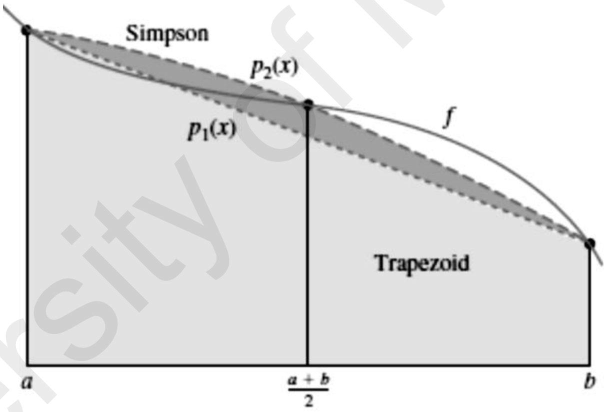

Figure 3.7: Comparison between the Trapezoid Rule and Simpson's Rule. (Cheney & Kincaid, 2008)

Based on Riemann summation rule, it is known that smaller subintervals could be used to improve the approximation of the area under the curve $f(x)$ and reduce the error of the estimation. Besides, a larger number of subintervals or smaller subinterval is required when integrating a function which is highly oscillatory on certain points or subintervals.

When the shaded region in Figure 3.7 is subdivided into two equal subintervals with points a, $a + h$ and $a + 2h = b$, the area under the curve, defined in $[a, b]$, could be better approximated using Equation (3.23). This technique is called the basic Simpson's Rule (Cheney & Kincaid, 2008).

$$\int_a^b f(x)\,dx \approx \frac{h}{3}\left[f(a) + 4f(a+h) + f(b) \right], \tag{3.23}$$

where the subinterval $h = (b - a)/2$ with the error term as

$$-\frac{(b-a)^5}{180} f^{(4)}(\xi), \tag{3.24}$$

for some ξ in (a, b) and $f^{(4)}(\xi)$ is the fourth derivative of $f(\xi)$ which yields the Simpson's Rule to be fourth order accurate.

If the interval $[a, b]$ is further subdivided into N_h subintervals in which N_h is divisible by 2, thus the width of each subinterval is obtained as $h = (b - a)/N_h$ and each point is given as $x_i = a + ih$ for $0 \le i \le N_h$. This gives the Composite Simpson's Rule (Cheney & Kincaid, 2008) as

$$\int_a^b f(x)\,dx \approx \frac{h}{3}\left[f(a) + f(b) + 4\sum_{i=1}^{N_h/2} f\left[a + (2i-1)h\right] + 2\sum_{i=1}^{(N_h-2)/2} f(a + 2ih) \right], \tag{3.25}$$

with the error term as

$$-\frac{(b-a)h^4}{180} f^{(4)}(\xi), \tag{3.26}$$

for some ξ in (a, b) and $f^{(4)}(\xi)$ is the fourth derivative of $f(\xi)$ which yields the Composite Simpson's Rule to be fourth order accurate.

3.5.4 Discretisation for partial differential equation

The anomalous transport dynamic of charge carriers in organic semiconductors is studied by using the time-fractional drift-diffusion equation which is a generalisation form of the normal diffusion equation incorporated with drift term due to the applied electric field. So, it is worthwhile to take a look at the numerical method which can be used to obtain the solution of the normal diffusion equation. Diffusion equation is a parabolic type PDE which is written as (Burden & Faires, 2011; Cheney & Kincaid, 2008),

$$\frac{\partial f\left(x,t\right)}{\partial t}=D\frac{\partial^2 f\left(x,t\right)}{\partial x^2};\qquad 0<x<L,t>0, \tag{3.27}$$

where D is the diffusion coefficient and Equation (3.27) is subjected to the following conditions

$$\begin{aligned} f\left(0,t\right)&=f\left(L,t\right)=0, && t>0;\\ f\left(x,0\right)&=f\left(x\right), && 0\le x\le L. \end{aligned} \tag{3.28}$$

Finite difference method can be simply implemented to obtain the numerical solution of Equation (3.27). It is carried out by replacing the first order time derivative and second order space derivative in Equation (3.27) by Equation (3.14) and Equation (3.15) , respectively. The first order time derivative is approximated by using the backward difference method because the implicit difference scheme is unconditionally stable. Thus, a larger time step could be used to reduce the computation time and memory size as compared to the (smaller) time step required by the forward difference method. The second order space derivative is approximated by using the central difference scheme because smaller error is resulted as compared to that of the two-point midpoint difference schemes.

Let's define that the position is $x_i = i\Delta x$ for $0 \le i \le N_x$, time is $t_k = k\Delta t$ for $0 \le k \le N_t$, spatial step is $\Delta x = L/N_x$, time step is $\Delta t = T/N_t$, T is the total time, L is the device length, N_t is the total time step and N_x is the total spatial step. Thus, the solution at each grid point or node is represented as $f\left(x_i, t_k\right) \approx f\left(i\Delta x, k\Delta t\right) = f_i^k$. Thus, Equation (3.27) is rewritten as

$$\frac{1}{\Delta t}\left[f\left(x_i, t_k\right) - f\left(x_i, t_{k-1}\right)\right] = \frac{D}{\left(\Delta x\right)^2}\left[f\left(x_{i+1}, t_k\right) - 2f\left(x_i, t_k\right) + f\left(x_{i-1}, t_k\right)\right]. \quad (3.29)$$

We may group all the t–terms and (t–Δt)–terms of Equation (3.29) at the L.H.S. and R.H.S. Then, Equation (3.29) is written as

$$-f_{i-1}^k + rf_i^k - f_{i+1}^k = sf_i^{k-1}, \quad (3.30)$$

where $r = 2 + s$ and $s = D(\Delta x)^2/\Delta t$. Figure 3.8 shows the position of the four points in the Equation (3.30).

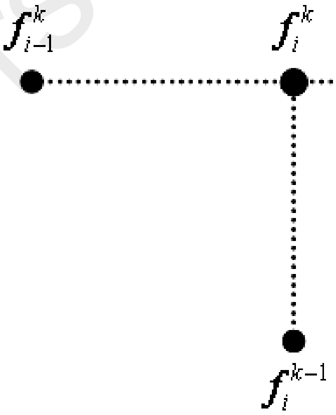

Figure 3.8: Implicit difference scheme for diffusion equation.

It should be noted that all f_i^{k-1} values at time t_{k-1} are known but all f_i^k values at time t_k are unknown. Let's define that $b_i^{k-1} = sf\left(x_i, t_{k-1}\right) = sf_i^{k-1}$, Equation (3.30) can then be written in a tri-diagonal and diagonally dominant matrix as

$$\begin{bmatrix} r & -1 & & & & & & \\ -1 & r & -1 & & & & & \\ & -1 & r & -1 & & & & \\ & & \ddots & \ddots & \ddots & & & \\ & & & -1 & r & -1 & & \\ & & & & \ddots & \ddots & \ddots & \\ & & & & & -1 & r & -1 \\ & & & & & & -1 & r \end{bmatrix} \begin{bmatrix} f_1 \\ f_2 \\ f_3 \\ \vdots \\ f_i \\ \vdots \\ f_{n-2} \\ f_{n-1} \end{bmatrix} = \begin{bmatrix} b_1 \\ b_2 \\ b_3 \\ \vdots \\ b_i \\ \vdots \\ b_{n-2} \\ b_{n-1} \end{bmatrix}, \tag{3.31}$$

or rewritten as

$$\mathbf{Af} = \mathbf{b} \,. \tag{3.32}$$

The unknown vector **f** can be solved because coefficient matrix **A** and R.H.S. vector **b** are known. The linear equation system can be easily solved numerically by using the Gaussian elimination method as described in the following subsection. The similar numerical scheme will be implemented to obtain the solutions of the fractional time drift-diffusion equation that represents the anomalous transport dynamic of charge carriers in disordered organic semiconductors. The numerical procedure is described in the section 3.5.6.

3.5.5 Gaussian elimination for solving linear equation systems

Many problems in science and engineering can be represented by a linear equation system. Typically, the approximation of a parabolic PDE by algebraic equation often produces a linear equation system which can be represented in a matrix form that has a tri-diagonal structure,

$$\begin{bmatrix} d_1 & c_1 & & & & & & \\ a_1 & d_2 & c_2 & & & & & \\ & a_2 & d_3 & c_3 & & & & \\ & & \ddots & \ddots & \ddots & & & \\ & & & a_{i-1} & d_i & c_i & & \\ & & & & \ddots & \ddots & \ddots & \\ & & & & & a_{n-2} & d_{n-1} & c_{n-1} \\ & & & & & & a_{n-1} & d_n \end{bmatrix} \begin{bmatrix} x_1 \\ x_2 \\ x_3 \\ \vdots \\ x_i \\ \vdots \\ x_{n-1} \\ x_n \end{bmatrix} = \begin{bmatrix} b_1 \\ b_2 \\ b_3 \\ \vdots \\ b_i \\ \vdots \\ b_{n-1} \\ b_n \end{bmatrix}, \qquad (3.33)$$

where all the other elements in the coefficient matrix are zero, coefficients a_i, b_i, c_i and d_i are known variables and x_j are unknown variables which will be determined.

Gauss elimination factorises the linear equation system (**Ax** = **b**) into an upper triangular matrix **U** and a lower triangular matrix **L**, thus the coefficient matrix **A** is rewritten as **A** = **LU**. The solution of the unknown vector **x** can be obtained from the upper triangular matrix **U** after completing the procedures in the Gauss elimination method. If the coefficient matrix **A** has specific form such as tri-diagonal, banded, or symmetric structure, lesser amount of memory is required to store the elements of the matrix. The conditions for the Gaussian elimination to be implemented and work effectively are the matrix coefficient **A** is a matrix with size $n \times n$ and do not have zero triangular elements in matrix coefficient **A**.

The first phase in solving the unknown vector **x** is called the forward elimination process where all the elements a of the matrix coefficient **A** will become zero (except a_1 term), elements b and d will be replaced by new values and element c is unchanged.

$$d_i \leftarrow d_i - \left(\frac{a_{i-1}}{d_{i-1}}\right) c_{i-1}; \qquad 2 \le i \le n. \qquad (3.34)$$

$$b_i \leftarrow b_i - \left(\frac{a_{i-1}}{d_{i-1}}\right) b_{i-1}; \qquad 2 \le i \le n. \qquad (3.35)$$

Thus, the matrix in (3.33) is reduced to a non-zero upper triangular matrix and written as

$$\begin{bmatrix} d_1 & c_1 & & & & & & \\ & d_2 & c_2 & & & & & \\ & & d_3 & c_3 & & & & \\ & & & \ddots & \ddots & & & \\ & & & & d_i & c_i & & \\ & & & & & \ddots & \ddots & \\ & & & & & & d_{n-1} & c_{n-1} \\ & & & & & & & d_n \end{bmatrix} \begin{bmatrix} x_1 \\ x_2 \\ x_3 \\ \vdots \\ x_i \\ \vdots \\ x_{n-1} \\ x_n \end{bmatrix} = \begin{bmatrix} b_1 \\ b_2 \\ b_3 \\ \vdots \\ b_i \\ \vdots \\ b_{n-1} \\ b_n \end{bmatrix}, \tag{3.36}$$

The second phase of the Gauss elimination is called the backward substitution process. In this phase, the solution of x_n in Equation (3.36) is obtained as

$$x_n = \frac{b_n}{d_n}. \tag{3.37}$$

After that, the i^{th}–element of vector **x** is obtained as

$$x_i \leftarrow \frac{1}{d_i}\left(b_i - c_i x_{i+1}\right); \qquad i = n-1, n-2, ..., 1. \tag{3.38}$$

3.5.6 Discretisation for fractional drift-diffusion equation

Approximate the space derivative and fractional time derivative in Equation (3.9) respectively by using the central difference scheme and Equation (3.18), thus the VO-TFDDE can be rewritten as

$$\begin{aligned} \frac{\partial^{\alpha(x_i,t_{k+1})} p\left(x_i,t_{k+1}\right)}{\partial t^{\alpha(x_i,t_{k+1})}} = D_\alpha \frac{\partial^2 p\left(x_i,t_{k+1}\right)}{\partial x^2} - \\ K_\alpha\left(x_i,t_{k+1}\right)\frac{\partial p\left(x_i,t_{k+1}\right)}{\partial x} - p\left(x_i,t_{k+1}\right)\frac{\partial K_\alpha\left(x_i,t_{k+1}\right)}{\partial x}. \end{aligned} \tag{3.39}$$

$$L^{\alpha_i^{k+1}} p_i^{k+1} = \tau_0 c^{\alpha_i^{k+1}} D\left[\frac{p_{i+1}^{k+1} - 2p_i^{k+1} + p_{i-1}^{k+1}}{(\Delta x)^2}\right] - \tau_0 c^{\alpha_i^{k+1}} v_i^{k+1}\left[\frac{p_{i+1}^{k+1} - p_{i-1}^{k+1}}{2\Delta x}\right] - \tau_0 c^{\alpha_i^{k+1}} \mu p_i^{k+1}\left[\frac{F_{i+1}^{k+1} - F_{i-1}^{k+1}}{2\Delta x}\right]. \tag{3.40}$$

The notations of $p_i^k, v_i^k, F_i^k, V_i^k, \alpha_i^k$ represent the approximations for the charge carrier density, velocity, electric field, electric potential and disorder parameter (fractional derivative order). Substitute Equation (3.18) into Equation (3.40) and group all the t_{k+1} and t_k terms on the L.H.S. and R.H.S. of Equation (3.40), respectively. Equation (3.40) is then written as

$$\begin{aligned} & p_i^{k+1} - \frac{\tau_0 c^{\alpha_i^{k+1}} D\Gamma\left(2-\alpha_i^{k+1}\right)\Delta t^{\alpha_i^{k+1}}}{(\Delta x)^2}\left(p_{i+1}^{k+1} - 2p_i^{k+1} + p_{i-1}^{k+1}\right) + \\ & \frac{\tau_0 c^{\alpha_i^{k+1}} \Gamma\left(2-\alpha_i^{k+1}\right)\Delta t^{\alpha_i^{k+1}} v_i^{k+1}}{2\Delta x}\left(p_{i+1}^{k+1} - p_{i-1}^{k+1}\right) + \\ & \frac{\tau_0 c^{\alpha_i^{k+1}} \Gamma\left(2-\alpha_i^{k+1}\right)\Delta t^{\alpha_i^{k+1}} \mu\left(F_{i+1}^{k+1} - F_{i-1}^{k+1}\right)}{2\Delta x} p_i^{k+1} \\ & = \left(1 - b_i^{1,k+1}\right) p_i^k + \sum_{m=1}^{k-1}\left(b_i^{m,k+1} - b_i^{m+1,k+1}\right) p_i^{k-m} + b_i^{k,k+1} p_i^0. \end{aligned} \tag{3.41}$$

By defining $C_{D,i}^{k+1} = \dfrac{\tau_0 c^{\alpha_i^{k+1}} D\Gamma\left(2-\alpha_i^{k+1}\right)\Delta t^{\alpha_i^{k+1}}}{(\Delta x)^2}$, $C_{v,i}^{k+1} = \dfrac{\tau_0 c^{\alpha_i^{k+1}} \Gamma\left(2-\alpha_i^{k+1}\right)\Delta t^{\alpha_i^{k+1}} v_i^{k+1}}{2\Delta x}$ and $C_{F,i}^{k+1} = \dfrac{\tau_0 c^{\alpha_i^{k+1}} \Gamma\left(2-\alpha_i^{k+1}\right)\Delta t^{\alpha_i^{k+1}} \mu\left(F_{i+1}^{k+1} - F_{i-1}^{k+1}\right)}{2\Delta x}$. The VOTFDDE is rewritten as

$$\begin{aligned} & \left(-C_{D,i}^{k+1} - C_{v,i}^{k+1}\right) p_{i-1}^{k+1} + \left(1 + 2C_{D,i}^{k+1} + C_{F,i}^{k+1}\right) p_i^{k+1} + \left(-C_{D,i}^{k+1} + C_{v,i}^{k+1}\right) p_{i+1}^{k+1} \\ & = \left(1 - b_i^{1,k+1}\right) p_i^k + \sum_{m=1}^{k-1}\left(b_i^{m,k+1} - b_i^{m+1,k+1}\right) p_i^{k-m} + b_i^{k,k+1} p_i^0, \qquad k \geq 1. \end{aligned} \tag{3.42}$$

When $k = 0$ and $\alpha_i^{k+1} = 1$, Equation (3.42) resembles the standard drift-diffusion equation.

$$\left(-C^{1}_{D,i} - C^{1}_{v,i}\right)p^{1}_{i-1} + \left(1+2C^{1}_{D,i} + C^{1}_{F,i}\right)p^{1}_{i} + \left(-C^{1}_{D,i} + C^{1}_{v,i}\right)p^{1}_{i+1} = p^{0}_{i}, \quad b^{0,1}_{i} = 1. \tag{3.43}$$

Let's define that $P^{k+1}_{i-1} = -C^{k+1}_{D,i} - C^{k+1}_{v,i}$, $R^{k+1}_{i} = -C^{k+1}_{D,i} + C^{k+1}_{v,i}$, $S^{k+1}_{i} = 1 + 2C^{k+1}_{D,i} + C^{k+1}_{F,i}$ and $Q^{k+1}_{i} = \left(1 - b^{1,k+1}_{i}\right)p^{k}_{i} + \sum_{m=1}^{k-1}\left(b^{m,k+1}_{i} - b^{m+1,k+1}_{i}\right)p^{k-m}_{i} + b^{k,k+1}_{i}p^{0}_{i}$. For $k \geq 1$ and $1 \leq i \leq N_{\text{x}} - 1$, Equation (3.43) is a set of linear equations for p^{k+1}_{i} that can be written in a matrix as

$$\begin{bmatrix} S^{k+1}_{1} & R^{k+1}_{1} & 0 & & \cdots & & 0 \\ P^{k+1}_{1} & S^{k+1}_{2} & R^{k+1}_{2} & & & & \\ 0 & \ddots & \ddots & \ddots & \ddots & & \vdots \\ & & P^{k+1}_{i-1} & S^{k+1}_{i} & R^{k+1}_{i} & & \\ \vdots & & \ddots & \ddots & \ddots & \ddots & 0 \\ & & & & P^{k+1}_{N_x-3} & S^{k+1}_{N_x-2} & R^{k+1}_{N_x-2} \\ 0 & & \cdots & & 0 & P^{k+1}_{N_x-2} & S^{k+1}_{N_x-1} \end{bmatrix} \begin{bmatrix} p^{k+1}_{1} \\ p^{k+1}_{2} \\ \vdots \\ p^{k+1}_{i} \\ \vdots \\ p^{k+1}_{N_x-2} \\ p^{k+1}_{N_x-1} \end{bmatrix} = \begin{bmatrix} Q^{k+1}_{1} \\ Q^{k+1}_{2} \\ \vdots \\ Q^{k+1}_{i} \\ \vdots \\ Q^{k+1}_{N_x-2} \\ Q^{k+1}_{N_x-1} \end{bmatrix}, \tag{3.44}$$

with the boundary conditions defined as $p(0,t) = p(L,t) = 0$.

The matrix in Equation (3.44) is a tri-diagonal matrix since the central three diagonal elements on the L.H.S. of the matrix are non-zero. Forward elimination and backward substitution method is adopted in order to solve the matrix in Equation (3.44) so that the solutions p^{k+1}_{i} of the VO-TFDDE can be obtained. After the forward elimination procedure, all the coefficient *P* are eliminated, all the coefficient *R* are remained and all the new values of the i^{th}–element of coefficient *Q* and *S* are calculated as:

$$S^{k+1}_{i} \leftarrow S^{k+1}_{i} - \left(\frac{P^{k+1}_{i-1}}{S^{k+1}_{i-1}}\right)R^{k+1}_{i-1}; \qquad 2 \leq i \leq N_x - 1. \tag{3.45}$$

$$Q^{k+1}_{i} \leftarrow Q^{k+1}_{i} - \left(\frac{P^{k+1}_{i-1}}{S^{k+1}_{i-1}}\right)Q^{k+1}_{i-1}; \qquad 2 \leq i \leq N_x - 1. \tag{3.46}$$

The matrix in Equation (3.44) is rewritten as

$$\begin{bmatrix} S_1^{k+1} & R_1^{k+1} & 0 & & \cdots & & 0 \\ 0 & S_2^{k+1} & R_2^{k+1} & & & & \\ & & \ddots & \ddots & & & \vdots \\ & & \ddots & S_i^{k+1} & R_i^{k+1} & \ddots & \\ \vdots & & & & \ddots & \ddots & 0 \\ & & & & & S_{N_x-2}^{k+1} & R_{N_x-2}^{k+1} \\ 0 & & \cdots & & & 0 & S_{N_x-1}^{k+1} \end{bmatrix} \begin{bmatrix} p_1^{k+1} \\ p_2^{k+1} \\ \vdots \\ p_i^{k+1} \\ \vdots \\ p_{N_x-2}^{k+1} \\ p_{N_x-1}^{k+1} \end{bmatrix} = \begin{bmatrix} Q_1^{k+1} \\ Q_2^{k+1} \\ \vdots \\ Q_i^{k+1} \\ \vdots \\ Q_{N_x-2}^{k+1} \\ Q_{N_x-1}^{k+1} \end{bmatrix}. \qquad (3.47)$$

In the backward substitution procedure, the first step is to obtain the solution $p_{N_x-1}^{k+1}$ from Equation (3.47) by

$$p_{N_x-1}^{k+1} = \frac{Q_{N_x-1}^{k+1}}{S_{N_x-1}^{k+1}}. \qquad (3.48)$$

After that, the i^{th}–element of p_i^{k+1} is obtained as

$$p_i^{k+1} = \frac{1}{S_i^{k+1}}\left(Q_i^{k+1} - R_i^{k+1} p_{i+1}^{k+1}\right); \qquad 1 \le i \le N_x - 2. \qquad (3.49)$$

3.5.7 Discretisation for electric potential and Poisson equation

Electric field established within the device due to the present of charge carriers and the external electric field could be calculated when the electric potential is obtained through solving the Poisson equation which is an elliptical partial differential equation. Thus, the numerical method used to solve the elliptic partial differential equation based on finite difference method will be employed. It is done by replacing the second order space derivative of the Poisson equation with the central difference scheme, thus Equation (3.10) is written as

$$\frac{V_{i-1}^{k+1}-2V_{i}^{k+1}+V_{i+1}^{k+1}}{\left(\Delta x\right)^{2}}=-\frac{e}{\varepsilon_{r}\varepsilon_{0}}\,p_{i}^{k+1}. \tag{3.50}$$

At k, for $k \geq 1$ and $1 \leq i \leq N_\mathrm{x} - 1$, Equation (3.50) is a set of linear equations for V_{i}^{k+1} and can be written in a matrix as

$$\begin{bmatrix} -2 & 1 & 0 & & \cdots & & 0 \\ 1 & -2 & 1 & & & & \\ 0 & \ddots & \ddots & \ddots & \ddots & & \vdots \\ & & 1 & -2 & 1 & & \\ \vdots & & \ddots & \ddots & \ddots & \ddots & 0 \\ & & & & 1 & -2 & 1 \\ 0 & & \cdots & & 0 & 1 & -2 \end{bmatrix}\begin{bmatrix} V_{1}^{k+1} \\ V_{2}^{k+1} \\ \vdots \\ V_{i}^{k+1} \\ \vdots \\ V_{N_x-2}^{k+1} \\ V_{N_x-1}^{k+1} \end{bmatrix}=-\frac{e\left(\Delta x\right)^{2}}{\varepsilon_{r}\varepsilon_{0}}\begin{bmatrix} p_{1}^{k+1}+\dfrac{\varepsilon_{r}\varepsilon_{0}}{e\left(\Delta x\right)^{2}}V_{0}^{k+1} \\ p_{2}^{k+1} \\ \vdots \\ p_{i}^{k+1} \\ \vdots \\ p_{N_x-2}^{k+1} \\ p_{N_x-1}^{k+1}+\dfrac{\varepsilon_{r}\varepsilon_{0}}{e\left(\Delta x\right)^{2}}V_{N_x}^{k+1} \end{bmatrix}, \tag{3.51}$$

where the boundary conditions are $V(0,t) = V_\mathrm{a}$ (applied bias) and $V(L,t) = 0$. All the values of the charge density ep_{i}^{k+1} on the R.H.S. of the matrix are known for all grid points. The matrix in Equation (3.51) is a tri-diagonal matrix since the central three diagonal elements on the L.H.S. of the matrix are non-zero. Thus, the similar steps used to obtain the solutions for the charge carrier density can also be used to solve for the electric potential. After that, the i^{th}–element of F_{i}^{k+1} is calculated using

$$F_{i}^{k+1}=-\left[\frac{V_{i+1}^{k+1}-V_{i-1}^{k+1}}{2\Delta x}\right]. \tag{3.52}$$

Electric fields at the terminals (boundaries) of the device are obtained as

$$F_{0}^{k+1}=-\left[\frac{V_{1}^{k+1}-V_{0}^{k+1}}{\Delta x}\right], \tag{3.53}$$

and

$$F_{N_x}^{k+1} = -\left[\frac{V_{N_x}^{k+1} - V_{N_x-1}^{k+1}}{\Delta x}\right]. \tag{3.54}$$

3.5.8 Discretisation for current density

By approximating the integration and the integer order time derivative in Equation (3.12) respectively with the composite Simpson's Rule and the forward difference method, the current density I^{k+1} at time t^{k+1} can be written as

$$J^{k+1} = \left(\frac{e}{\Delta t}\right)\left(\frac{\Delta x}{3}\right)\left[\begin{array}{l}\left(\frac{x_0}{L}-1\right)\left(p_0^{k+1}-p_0^k\right)+\left(\frac{x_L}{L}-1\right)\left(p_L^{k+1}-p_L^k\right)+ \\ 2\sum_{i=1}^{N_x/2-1}\left(\frac{x_{2i}^{k+1}}{L}-1\right)\left(p_{2i}^{k+1}-p_{2i}^k\right)+4\sum_{i=1}^{N_x/2}\left(\frac{x_{2i-1}^{k+1}}{L}-1\right)\left(p_{2i-1}^{k+1}-p_{2i-1}^k\right)\end{array}\right] \tag{3.55}$$

3.6 Simulation procedures

The simulation first started with reads in required simulation parameters such as the device structure and material parameters (see Table 5.1 and Table 5.2 for the full list of the required parameters used in the simulation). Secondly, the mesh of the TOF cell (device) is established with equi-distance spacing. Thirdly, the initial and boundary conditions for charge carrier density, electric potential and electric field are defined in the simulation. Fourthly, the propagation of charge carriers is obtained by solving the fractional time drift-diffusion equation. Fifthly, the local electric field is obtained by solving the Poisson equation. Step four and step five are then repeated alternately till the simulation time is fulfilled. Finally, all the output data such as the charge carrier density, electric field, electric potential and current density are recorded in the data files. The flow of the simulation process is summarised in Figure 3.9.

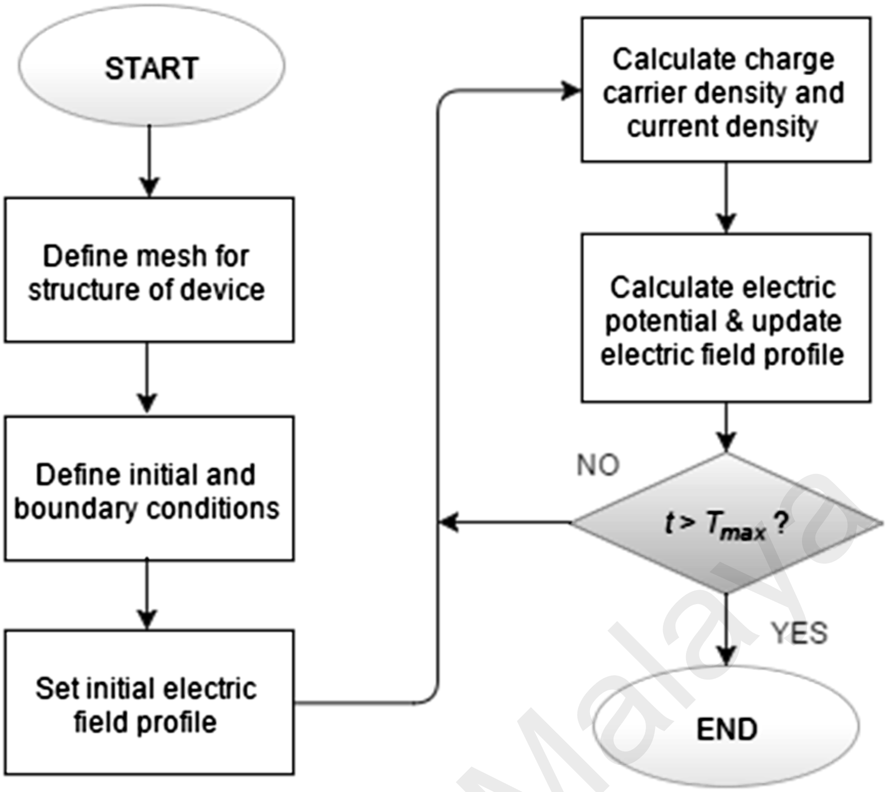

Figure 3.9: Flow chart of transport dynamic simulation of charge carrier

The simulation code is developed and implemented using the FORTRAN programming language. The main programming code representing the simulation procedures is demonstrated below and the details of each subroutine are given in APPENDIX B.

```
Program begin
     call readin      ! Input device and material parameters
     call paras       ! Preprocess input parameters
     call init01      ! Initiate data array
     call mesh        ! Define mesh
     call setic       ! Define initial conditions
     call capcnt      ! Calculate capture rate
     call setbc       ! Define boundary conditions
     call dev1d       ! Perform device simulation
Program end
```

The optimisation of the fitting scheme is carried out by means of the simulation setup is established to replicate the structure of TOF cell and the parameters used in the simulation are chosen based on a range of experiment values for the material studied.

Figure 3.10 shows the transient currents calculated for various mesh sizes. The transient current reduces greatly when the space interval is halved from 1.25 nm to 0.625 nm. However, the transient current reduces slightly when the space interval is further reduced from 0.6325 nm to 0.408 nm which is roughly three times smaller than 1.25 nm. It is obvious that the change in transient current becomes stagnant when the space interval is reduced up to a critical value which depends on material and device parameters. Besides, the effect of time step on the transient current is less significant as compared to that of the space interval. For this reason, the simulation should be carried out at smaller spatial interval in order to obtain more accurate results which will lead to a significant rise in the computation time. Thus, there is a trade-off between the space interval and computation time. The space interval and time step used for RRa-P3HT and RR-P3HT (~94%) are given in Table 5.1 and Table 5.2, respectively.

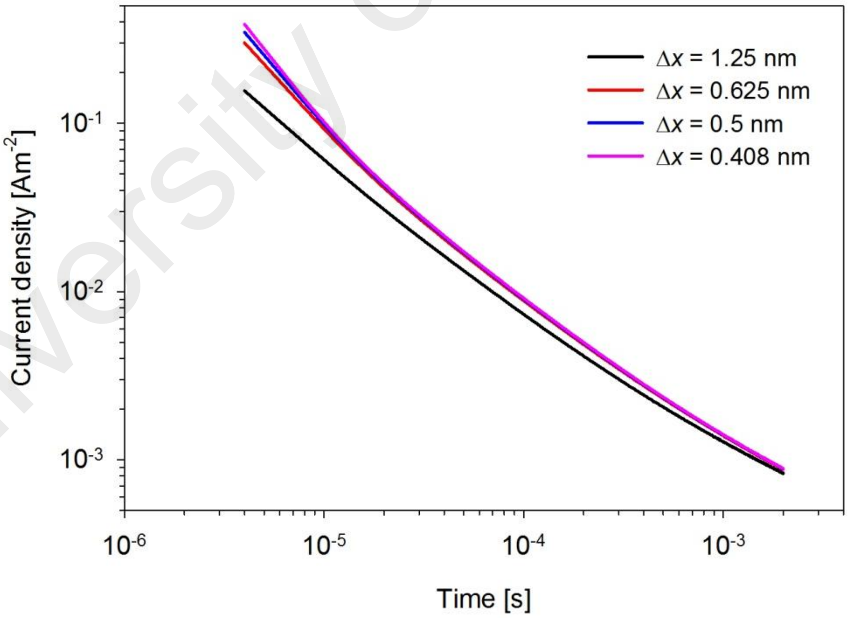

Figure 3.10: Transient currents calculated for various mesh sizes.

CHAPTER 4: OFET NOISE STUDY BASED ON FRACTAL ANALYSIS

This chapter reports the measurement results of output current and transient current noise of P3HT OFET. It is then followed by the fractal noise analysis results of the transient current noise obtained from the power spectral density method and detrended fluctuation analysis. A brief summary is included at the end of this chapter.

4.1 Experiment conditions

Poly(3-hexylthiophene-2,5-diyl) OFETs with top-contact and bottom-gate structure are fabricated (see section 3.1) and the current noises are obtained at various source-drain voltages (see section 3.2) in order to facilitate the current noise analysis which is then implemented by using the PSD method and DFA (see section 3.3). The results and findings of the current noise analysis of P3HT OFET are reported in the following section.

4.2 Results and discussion on OFET noise analysis

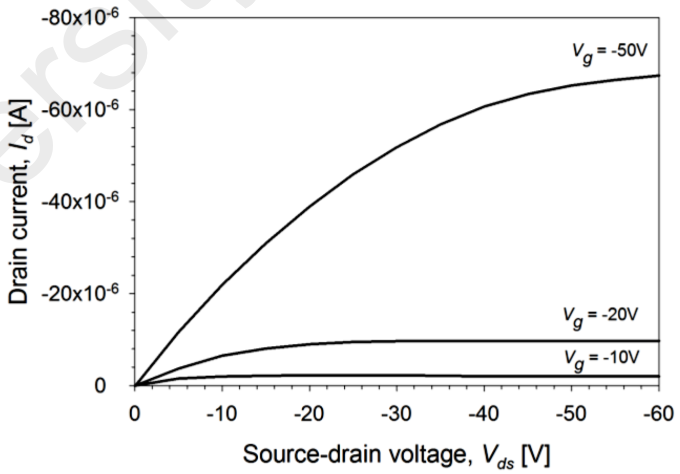

Figure 4.1: Output characteristic of P3HT OFET with channel length of 40 μm. The source-drain voltage is swept from 0 V to –60 V for each gate voltage.

The output characteristic of the P3HT OFET is depicted in Figure 4.1, where solid lines represent the sweeping of source-drain voltage from 0 V to –60 V at various gate voltages ranging from 0 V to −60 V. For all the applied gate voltages, it is clearly seen that the drain currents begin to saturate when the source-drain voltage V_{ds} is swept till close to the applied gate voltage and then saturated if V_{ds} is further increased. This is simply due to the pinch-off condition has been achieved.

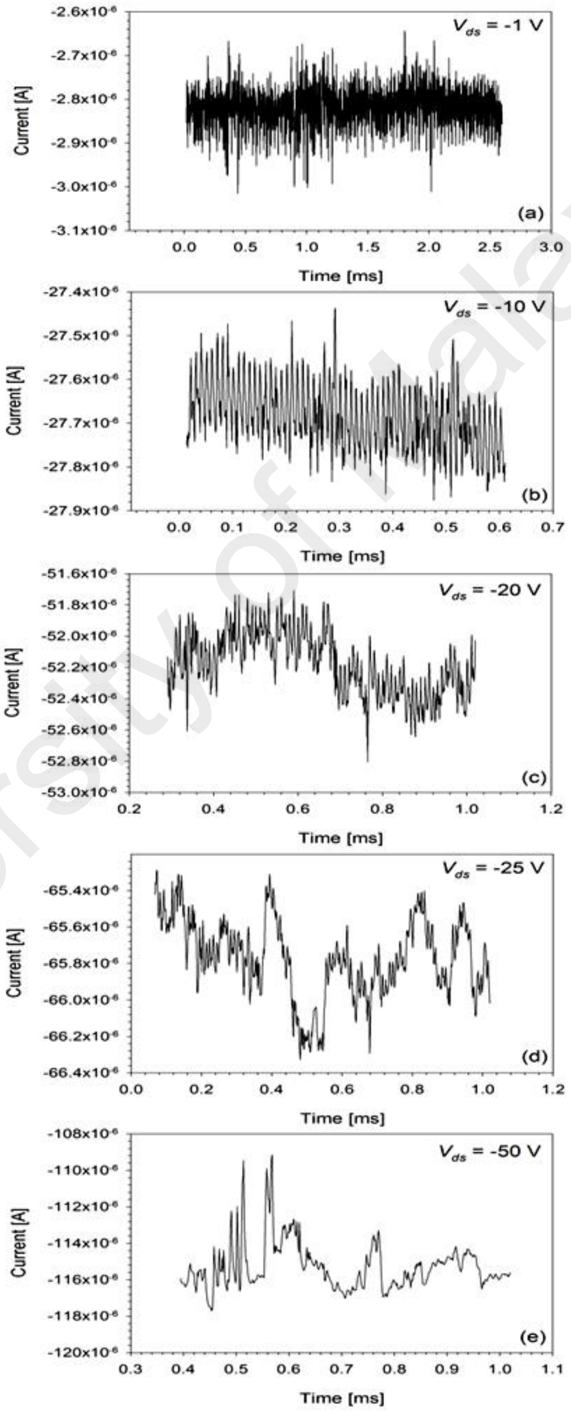

Figure 4.2: Measured transient current noises of OFETs at various V_{ds}: (a) −1 V, (b) −10 V, (c) −20 V, (d) −25 V and (e) −50 V.

The measured current noises of OFETs at various source-drain voltage V_{ds} ranging from −1 V to −50 V while having the gate voltage V_g fixed at −60 V are shown in Figure 4.2(a)-(e). It can be clearly seen that the profile of the current noise is gradually changing from white noise (rough time series) to 1/*f* noise and then to Brownian noise behaviour (smoother time series) as V_{ds} increases. The deviation of behaviour of the transient current noise at different V_{ds} is also observable through the calculated transient current noise PSD obtained at high frequency region in which the scaling exponent β_{PS} of the PSD is ranging from around 0.1 (white noise) to 2.0 (Brownian noise) as shown in Figure 4.3(a)-(e). This observation is further evidenced by the DFA in which the calculated scaling exponent α_{DFA} of the DFA obtained at a short time window is changing from around 0.5 (white noise) to 1.5 (Brownian noise) as shown in Figure 4.4(a)-(e).

At $V_{ds} = -1$ V, 1/*f* noise and shot noise are observed respectively at the low and high frequency regions of the PSD as shown in Figure 4.3(a). The presence of 1/*f* noise at the low frequency region of the PSD is due to the summation of the generation-recombination noise spectral (Kasap & Capper, 2006). Generation-recombination noise is due to the random capturing and releasing of charge carries at trap centres. This also leads to the fluctuation of the number of free charge carriers occurring in the device. When the device is operated at low voltage (below −2.5 V), free charge carries are injected from the source contact, undergo trapping and then being released from the trap centres as they drift across the channel region of the OFET. Hence, each charge carrier arrives at the drain contact at a purely uncorrelated time. This transport mechanism causes the occurrence of shot noise in the device. The calculated scaling exponent α_{DFA} of the DFA confirmed that the measured current noise at $V_{ds} = -1$ V is having the white noise behaviour as shown in Figure 4.4(a).

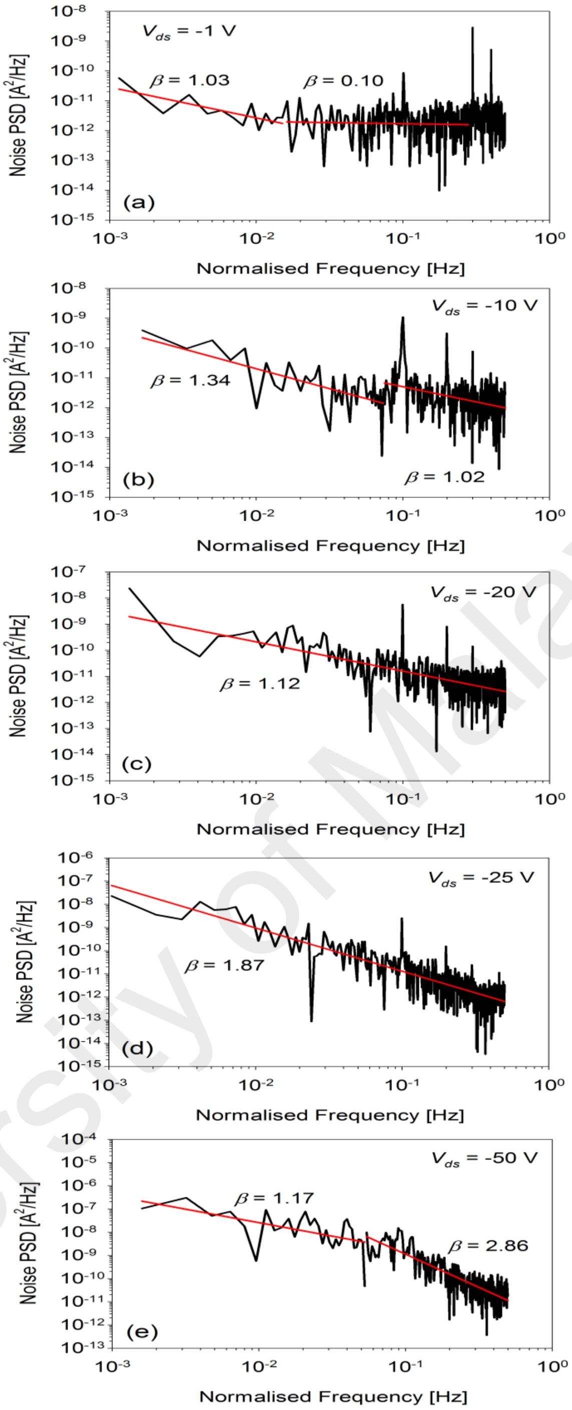

Figure 4.3: PSDs of transient current noises of OFETs obtained at various V_{ds}: (a) −1 V, (b) −10 V, (c) −20 V, (d) −25 V and (e) −50 V. The straight line indicates the least-squares line of the PSD.

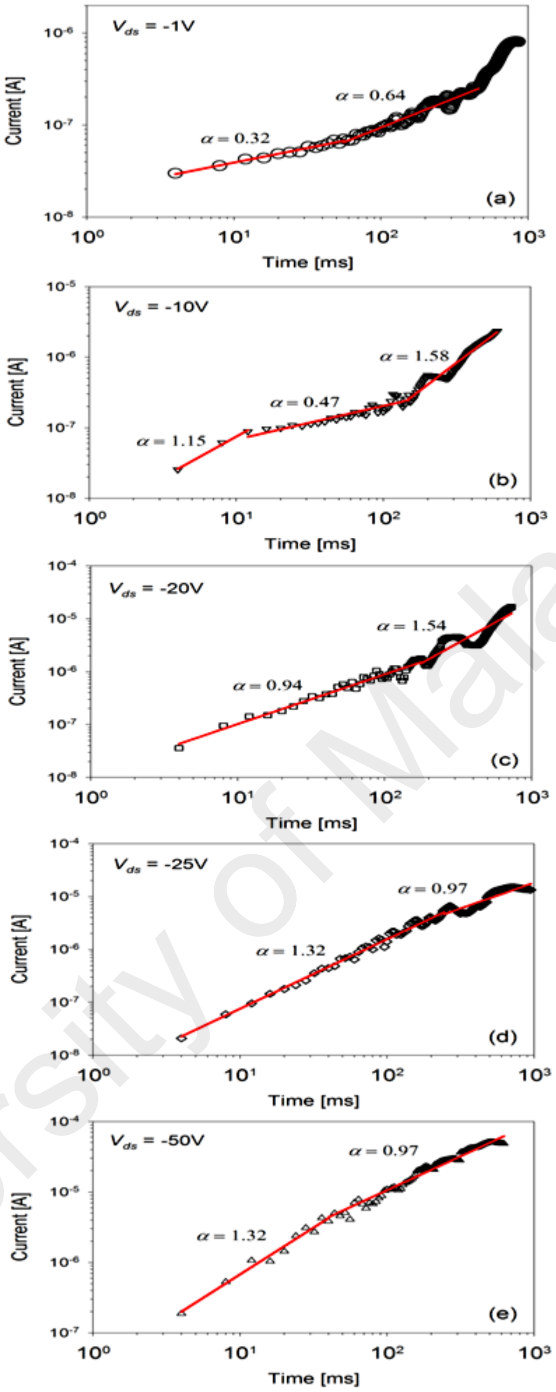

Figure 4.4: DFA of transient current noises of OFETs obtained at various V_{ds}: (a) −1 V, (b) −10 V, (c) −20 V, (d) −25 V and (e) −50 V. The straight line indicates the least-squares line of the DFA.

As V_{ds} increases to −10 V, both the PSD method and DFA indicate that the current noise presents with 1/*f* noise at the high frequency region of the PSD (Figure 4.3(b)) and corresponds to a short time window of the DFA (Figure 4.4(b)). On the other hand, Brownian noise is detected at low frequency region of the PSD and corresponds to a large time window of DFA. It is also interesting to see that the white noise behaviour of the current noise is detected by the DFA using a medium time window. When the device is biased at moderate V_{ds}, free charge carriers are injected from the source contact into the channel region and all trap centres will be immediately filled first while the remaining large amount of free charge carries are continuously hopping towards the drain contact to produce current. Since electric field established at the channel region extends and covers relatively a larger area as compared to that of the threshold voltage, thus it contains a larger amount of trap centres that enhances the occurrence of generation-recombination noise. The summation of the generation-recombination noise spectral of a larger channel region eventually resulted in $1/f$ noise that happened at a very short time period (Kasap & Capper, 2006). After a very short time, all trap centres have been filled and the remaining free charge carriers are hopping towards the drain contact in which each hopping is not correlated with each other. Meanwhile, trapped charge carriers can be released from the trap centres and continue to hop towards the drain contact. On the other hand, free charge carries can be captured by trap centres again. Releasing of trapped charge carriers and re-trapping of free charge carriers are also occurring in an uncorrelated manner. Based on these reasons, the resulted current is fluctuating randomly like a white noise. In addition, a Brownian noise-like current fluctuation is detected by both the PSD method and DFA (Figure 4.4(b)). This could be attributed to the collective effect of hopping, capturing and releasing of charge carriers over a long time period.

At $V_{ds} = -20$ V, both the PSD method and DFA indicate that the current noise presents with $1/f$ noise for the entire frequency region of the PSD (Figure 4.3(c)) and at medium time window of DFA (Figure 4.4(c)). This is simply due to the summation of generation-recombination noise spectra that lead to the $1/f$ noise when the electric field extended to cover a larger area of the channel region that contains a relatively huge amount of trap centres as compared to that of the number of trap centres at $V_{ds} = -10$ V. Besides that, Brownian noise is detected when the current noise is analysed by DFA using large time window. This could be attributed to the collective effect of hopping, capturing and releasing of charge carriers over a long time period as observed at $V_{ds} = -10$ V. As shown in Figure 4.2(c), it can be seen that the profile of current noise reveals a slight Brownian noise behaviour that is detectable by DFA. This demonstrates that DFA is a more sensitive method as compared to PSD method in detecting the nonstationary properties of the current noise.

At $V_{ds} = -25$ V, both the PSD method and DFA indicate that the current noise presents with Brownian noise for the entire frequency region of the PSD (Figure 4.3(d)) and at medium time window of DFA (Figure 4.4(d)). It is interesting to see that charge carriers are now having an opposite transport dynamics as compared to the transport dynamics that occurred at lower V_{ds} (< -20 V). This suggests that correlation is induced between each charge carrier hopping and causes charge carriers hopping like Brownian particles in the device when the device is operated at high electric field. Besides that, $1/f$ noise is observed when the current noise is analysed by DFA method using large time window in which PSD method is not sensitive enough to reveal this behaviour. The occurrence of $1/f$ noise is simply due to the fact that a large amount of trap centres is provoked by the electrically induced stress on the active material which causes larger generation-recombination noises. The summation of generation-recombination noise spectra eventually yields the $1/f$ noise in the current noise that weakens the existence of Brownian noise.

Transport dynamics that happened at $V_{ds} = -25$ V is also reproducible when device was operated at even higher bias, $V_{ds} = -50$ V. The scaling exponent α_{DFA} of DFA indicates that charge carriers are hopping like Brownian particles. However, PSD method failed to analyse a highly non-stationery current noise since it calculated an unrealistic value of scaling exponent, $\beta_{PS} > 2$ for Brownian noise. In addition, both PSD method and DFA indicate that the current noise presents with 1/*f* noise for the low frequency region of the PSD (Figure 4.3(e)) and corresponds to large time window of DFA (Figure 4.4(e)). Since the total number of trap centres occurred at −50 V is relatively larger than the total number of trap centres at −25 V, thus the PSD method is able to sense the presence of 1/*f* noise. The increment of the total number of trap centres when the device is operating at high applied voltage also signifies the degradation of the performance of device.

4.3 Summary

Current noises of P3HT-based OFETs were measured at various source-drain voltages for a fixed gate voltage and analysed using PSD method and DFA. Detrended fluctuation analysis is found to be a more accurate and sensitive method to detect the change in the transport dynamics of charge carriers in which it is characterised by the scaling behaviour of the current noise as compared to that of the PSD method. This is owing to the fact that PSD method becomes an unreliable tool when the current noise becomes a highly non-stationery time series. White noise is observed for the current noise measured at low V_{ds}, 1/*f* noise occurs at intermediate V_{ds}, and Brownian noise occurs at high V_{ds}. It is observed that a large number of trap centres was induced when the device was operated at high applied V_{ds} where these trap centres resulted in 1/*f* noise that could diminish the existence of Brownian noise in a very short time at high V_{ds}. It should be noted that if various fluctuation dynamics could produce generic characteristics and each dynamic is not being singled out from the experiment setup, this could result in ambiguity to identify the transport dynamics involved and hence imposes the limitation on how much information one could gain from the analysis.

CHAPTER 5: TRANSPORT STUDY OF RRa-P3HT AND RR-P3HT

Chapter 5 provides the conditions which are needed in the charge transport simulations for RRa-P3HT at different electric field and RR-P3HT at different light intensities. The simulated results are then plotted together with the measurement results extracted from publish works for comparison (Mauer et al., 2010). It is then followed by the discussions on the anomalous charge transport in these materials and a summary of the results is provided at the end of this chapter.

5.1 Simulation conditions

A simple one-dimensional structure with equidistance mesh is adopted to represent the cell of the TOF measurement as depicted in Figure 5.1. Two types of materials are considered in the simulation so that the simulated results could be compared with the experiment data that are digitised from Figure 2 and Figure 6 in (Mauer et al., 2010) for RRa-P3HT and RR-P3HT (~94%), respectively. A light pulse is initially shone on the top surface of the cell ($x = 0$) so that free charge carriers are generated just beneath the surface of the cell and exponentially decaying into the cell according to $N(x) = N_0 \, \mathrm{e}^{-\alpha_a x}$, where α_a is the absorption coefficient, N_0 is the photo-generated charge carrier density and x is the depth beneath the surface of the cell. Charge carriers are then diffusing and drifting towards the other end of the cell due to the external electric field.

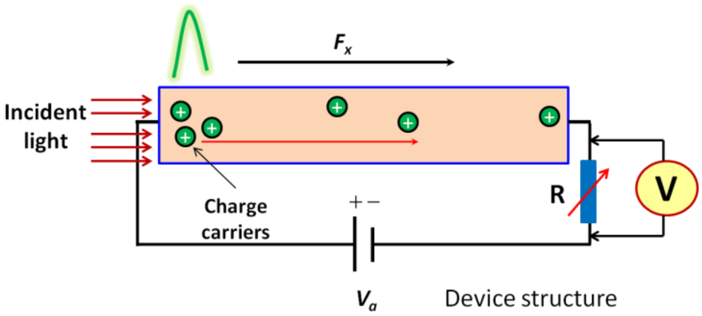

Figure 5.1: Schematic diagram represents the cell in TOF measurement.

The transport dynamic of charge carrier is modelled by the VO-TFDDE. The dielectric constant of the material is taken to be 3.4. The parameters used in the simulations are tabulated in Table 5.1 and Table 5.2 respectively for the RRa-P3HT and RR-P3HT (~94%) materials.

Table 5.1: Simulation parameters for RRa-P3HT.

Parameter	**Value**
Length of TOF cell, L	1.02 μm
Temperature, T	21 °C
Absorption coefficient, α_a	1.6×10^{-5} cm^{-1}
Space interval, Δx [nm]	0.425
Time step, Δt [μs]	4

Parameter	**Electric field, F [V/μm]**			
	10	20	35	50
Dispersive parameter, α	0.50	0.50	0.50	0.50
Mobility, μ [cm^2/Vs]	2.6×10^{-6}	2.6×10^{-6}	2.6×10^{-6}	2.6×10^{-6}
Average time of delocalisation, τ_0 [s]	5.0×10^{-13}	5.0×10^{-13}	5.0×10^{-12}	5.0×10^{-11}
Capture rate, ω_0 [s^{-1}]	2.0×10^{12}	2.0×10^{12}	2.0×10^{11}	2.0×10^{10}
Charge density, N_0 (t = 0 s) [cm^{-3}]	7.0×10^{14}	4.8×10^{15}	1.4×10^{16}	3.0×10^{16}
Average length of delocalisation, $l_d = \mu\tau_0 F$ [m]	1.3×10^{-15}	2.6×10^{-15}	4.6×10^{-14}	6.5×10^{-13}

Table 5.2: Simulation parameters for RR-P3HT (~94%).

Parameter	**Value**	
Applied bias, V	40 V	
Length of TOF cell, L	2 μm	
Temperature, T	50 °C	
Absorption coefficient, α_a	2×10^{-5} cm^{-1}	
Space interval, Δx [nm]	0.8	
Time step, Δt [μs]	0.2	
Parameter	**Light intensity, I_0 [%]**	
	4	10
Dispersive parameter, α	0.90	0.99
Mobility, μ [cm^2/Vs]	1.9×10^{-5}	7.9×10^{-5}
Average time of delocalisation, τ_0 [s]	1.43×10^{-13}	1.43×10^{-12}
Capture rate, ω_0 [s^{-1}]	7.0×10^{12}	7.0×10^{11}
Charge density, N_0 (t = 0 s) [cm^{-3}]	1.5×10^{17}	2.0×10^{17}
Average length of delocalisation, $l_d = \mu\tau_0 F$ [m]	5.4×10^{-15}	2.3×10^{-13}

5.2 Results and discussion on transport dynamics of RRa-P3HT and RR-P3HT

Figure 5.2 shows the transient current curves of RRa-P3HT which were digitised from Figure 6 in (Mauer et al., 2010) and measured using the TOF measurement at different electric fields. The transient current curves, represented by different lines in Figure 5.2, were calculated by the VO-TFDDE and reproduced the experimental results very well. It can be seen that all the current curves at different electric fields did not show a plateau or a transition region before they ended with a long-tail on the double-log current-time plot. This indicates that charge carriers are propagating very slowly across the TOF cell.

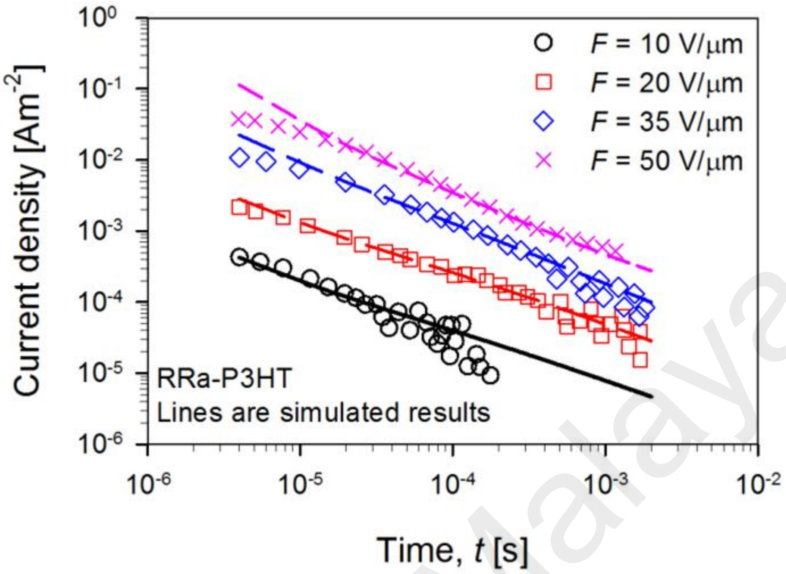

Figure 5.2: Transient current curves: symbols (digitised from Figure 6 in (Mauer et al., 2010)) - TOF measurement data for RRa-P3HT at different electric fields; lines: simulated results using the VO-TFDDE at different electric fields.

This is because charge carriers are frequently captured into the trap centres and hopping with very low velocity which causes them to only be able to jump for a short distance between successive hopping events. This causes charge carries are not propagating far away from the location where they are photo-generated as shown in Figure 5.3. Thus, charge carriers require extremely long time to move out from the TOF cell. This situation is clearly observed in the measurement performed at low electric field as compared to that of the high electric field.

However, it is noticeable that a larger number of charge carriers are generated as the electric field increases and then resulted in higher current level. This is because charge carriers residing in deeper energy levels are able to acquire additional energy from higher electric field and escape from the trap centres. They then hop with higher velocity in the direction parallel to the direction of electric field and jump with a longer average delocalisation length before they are trapped into another empty trap centre which is located at further distance as compared to that of the low electric field. Thus, this leads to the reduction of the average time taken by a charge carrier to be released from a trap centre and then hop to another empty site as the electric field increases.

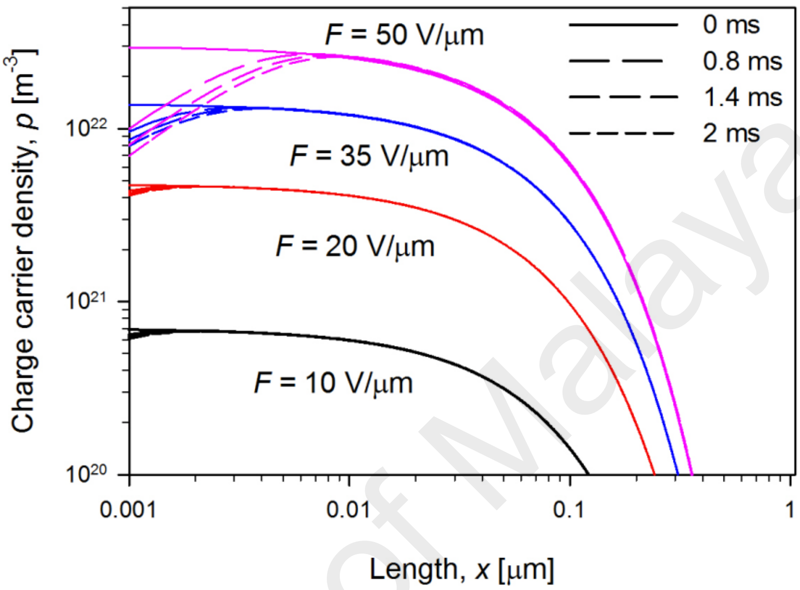

Figure 5.3: Charge carrier density profile for RRa-P3HT at various electric fields and times.

Figure 5.4 shows the transient current curves of RR-P3HT (~94%) that are digitised from Figure 2 in (Mauer et al., 2010) and measured using the TOF measurement at different light intensities. The transient current curves, represented by different lines in Figure 5.4, are calculated by the VO-TFDDE and they reproduce reasonably well the experimental results. At low light intensity, the transient current shows a vague plateau region, followed by a soft transition region and then decaying to a long-tail eventually. This demonstrates that the propagation of charge carriers is due to slow charge carriers that move with low mobility.

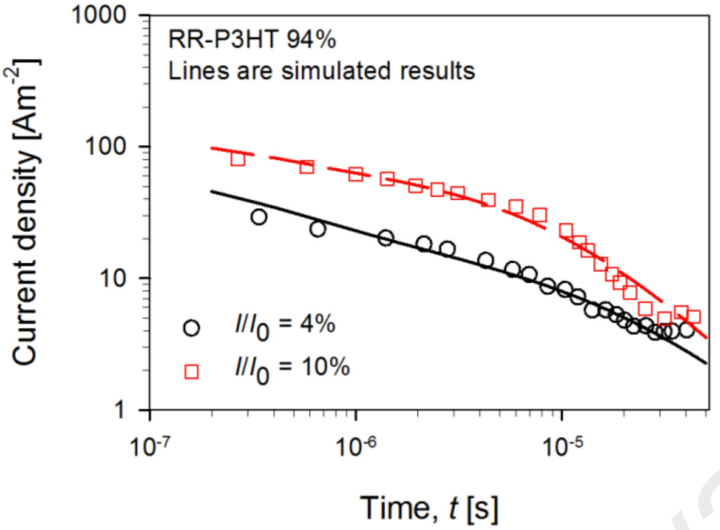

Figure 5.4: Transient current curves: symbols (digitised from Figure 2 in (Mauer et al., 2010)) - TOF measurement data for RR-P3HT (~94%) at different light intensities; lines - simulated results using the VO-TFDDE at different electric fields.

While the TOF cell is shone with low light level, there is only a small amount of charge carriers generated during the photo-absorption process and populates at the deep energy levels which are located far below the mobility edge as shown in Figure 5.5. When the TOF cell is biased, these charge carriers will begin to hop, in the direction of electric field, from one trap centre to another empty trap centre which is located within the deep energy levels.

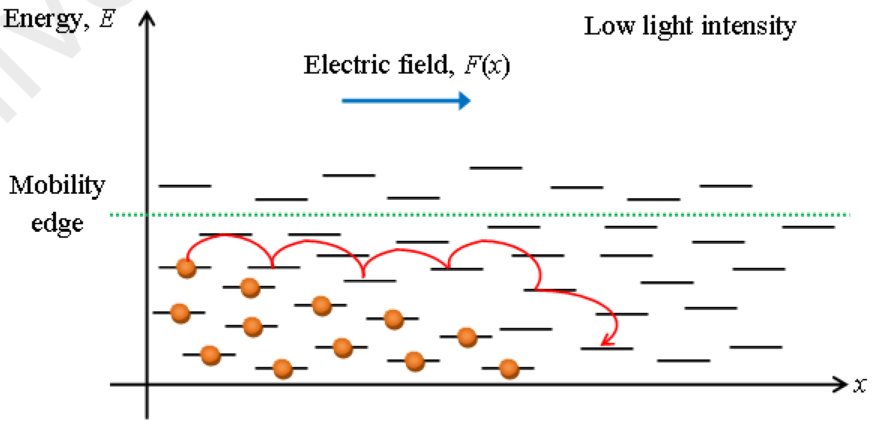

Figure 5.5: Generation and propagation of charge carries at low light intensity.

During the hopping process, charge carriers will be encountering a large number of trapping events since they are hopping in an environment present with many unfilled trap centres and yield higher capture rate at low light intensity than that of the high light intensity. This causes most of the charge carriers to still be located near to the vicinity where they are photo-generated as shown in Figure 5.6. Based on these facts, the transport behaviour of charge carriers at low light intensity becomes dispersive and causes the charge carriers to take considerable amount of time to drift out from the TOF cell which results in a long-tail transient current curve.

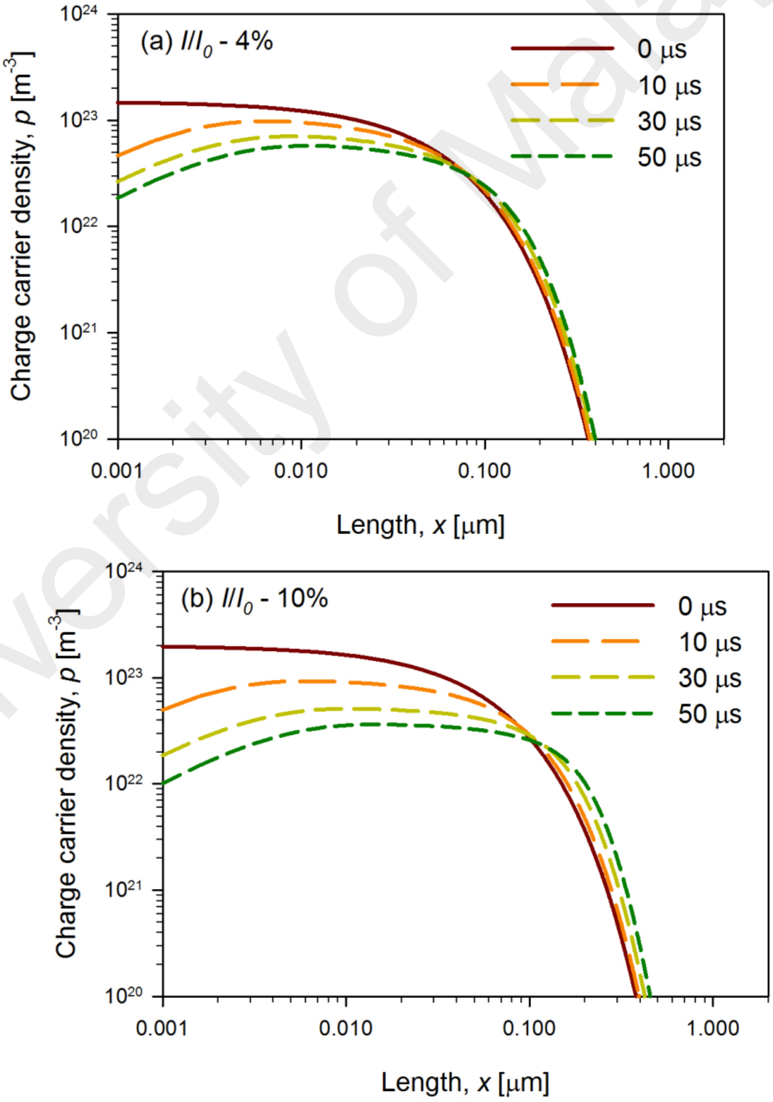

Figure 5.6: Charge carrier density profile for RR-P3HT (~94%) at various times for (a) low-light intensity and (b) high-light intensity.

In contrast to low light intensity, the transient current measured at higher light intensity shows a clearer plateau, a transition region and then eventually followed by a long-tail as shown in Figure 5.4. This indicates that the transport dynamics of charge carriers is becoming slightly less dispersive as the light intensity increases. At higher light intensity, a huge number of charge carriers is generated during the photo-absorption process. These charge carries will be first populating within the deep energy levels and then the excessive charge carriers will be stacking up to higher energy levels which are located nearer to the mobility edge as shown in Figure 5.7.

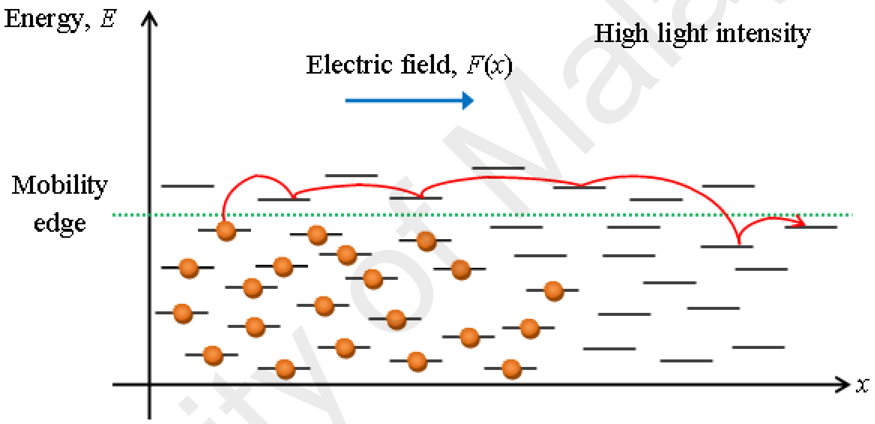

Figure 5.7: Generation and propagation of charge carries at high light intensity.

Charge carrier can now hop at higher velocity from one trap centre to another empty trap centre which is located close to the mobility edge. They will encounter lesser capturing event and able to hop at a longer average delocalisation length as compared to that of the low light intensity. Therefore, the propagation of charge carriers at high light intensity requires lesser time to leave the TOF cell as shown in Figure 5.6. In view of the facts that the RR-P3HT has lower capture rate and larger average length of delocalisation, thus the transport dynamic of charge carriers in RR-P3HT is less dispersive and much faster than that of the RRa-P3HT.

5.3 Summary

The dispersive transport dynamic of charge carriers in organic semiconductors is modelled using the time-fractional drift-diffusion equation which is approximated using the finite difference method. Numerical solutions of charge carrier density are obtained which enables the calculation of transient current density. When electric field is increased, charge carriers are able to acquire additional energy from the field which promotes them to be released much easier from the trap centres and then propagating at higher velocity before leaving the TOF cell that eventually results in higher transient current. When light intensity is increased, a huge number of charge carriers can be generated and occupying energy levels close to the mobility edge where charge carriers will encounter lesser capturing event and hop at a longer average delocalisation length in each successive hopping. This causes charge carriers to move less depressively for a short time interval before the occurrence of long-tail behaviour. Besides, the transport dynamic of charge carriers in RR-P3HT is relatively less dispersive and has higher mobility than that of the RRa-P3HT since RR-P3HT has lower capturing rate and is less energy disordered.

CHAPTER 6: CONCLUSIONS

Chapter 6 summarises the findings of this work and provides the recommendations and suggestions for future works.

6.1 Summary

Noise analysis in disordered organic semiconductor devices is frequently overlooked regardless of the importance of this approach which can be used to explore the transport dynamics of charge carriers, bulk or interface defects, trap density and structural properties of disordered organic semiconductors. Besides, the current noise of organic semiconductor device deviates from the common 1/*f* noise behaviour which could not be simply analysed by power spectra method. This work began on the study of transport dynamics of charge carriers in disordered material by using fractal noise analysis. Therefore, top-contact and bottom-gate P3HT-based OFETs had been fabricated with thermal treatment condition. Transient current noises of the OFETs were measured at various V_{ds} ranging from 0 V to −60 V with respect to a fixed gate voltage of −60 V. The results from conventional PSD method were compared with the DFA. The latter has been proven to be a more reliable method for fractal signal analysis particularly in the presence of nonstationary effects.

Interesting transitions between multiscaling to monoscaling behaviours were observed in the PSD as well as the DFA plots for different applied V_{ds}. Uncorrelated white noise characteristics are observed for current noise measured at low V_{ds}, meanwhile 1/*f* noise-like scaling behaviours are observed at intermediate V_{ds}. At higher V_{ds}, the noise characteristics appeared to be close to Brownian-like power-law behaviour. The scaling characteristics of the transient current noise can be related to the charge carrier dynamics. It is also found that large numbers of trap centres are induced when the device is stressed at high applied V_{ds}. The existence of these trap centres would disperse charge carriers, leading to 1/*f* type noise that could diminish the presence of Brownian noise in a very short time.

Owing to the fact that anomalous transport has dispersive and non-Gaussian transport dynamics, thus anomalous transport cannot be adequately described by the standard drift-diffusion equation which is a framework commonly used to model normal diffusive transport. Therefore in the second part of this work, the standard drift-diffusion equation was generalised to TFDDE using the fractional calculus approach to model the anomalous transport in the RRa-P3HT and RR-P3HT. Physical elucidation of TFDDE is given by stressing how the influence of the multiple-trapping mechanisms and disorder in energy lead to the long-tail behaviour in the transient photocurrent curves.

Time-fractional drift-diffusion equation is solved numerically using finite difference scheme to obtain the profiles of charge carriers density evolution and hence to reproduce the corresponding transient photocurrents of RRa-P3HT and RR-P3HT. Poisson solver is also included in the model to account for the fluctuation of localised electric field due to the evolution of charge carriers. It is found that charge carriers acquire additional energy from high electric field that helps them to escape from the trap centres more easily and then propagating at higher velocity, which yields higher transient current. Higher concentration of charge carriers can be generated at higher light intensity and they can occupy energy levels close to the mobility edge, where charge carriers will encounter smaller capturing rate and hop at a longer length in each hopping event. Thus, the transport dynamic of charge carriers at high light intensity is less dispersive than that of the low light intensity. Besides, the transport dynamic of charge carriers in RR-P3HT is relatively less dispersive and has higher mobility than that of the RRa-P3HT since RR-P3HT has lower capturing rate and less disorder in energy. It should be noted that the present study employed non-standard method based on fractal theory and fractional calculus to describe power-law scaling noise spectra and dispersive charge carrier transport dynamics in disordered organic semiconductors. At the end of this study, these methods have been proven successfully in describing and reproducing current noise and charge transport dynamics in disordered organic semiconductors.

6.2 Recommendation and future works

A large number of grid points and smaller time intervals are needed in order to detect the rapid change in the transport dynamics of the charge carriers and current density calculation. This causes a high demand on the memory, computation time as well as data storage. The recommendations for overcoming these issues could be:

1. adaptive mesh method could be used to replace the equi-distance mesh so that finer spatial step is used at device region with higher electric field and vice versa.
2. adopt adaptive method on the composite Simpson's rule to reduce the total number of grid points used to define the mesh of the TOF cell.

Since molecular recombination is an important process which could cause fluctuation and reduction in current that leads to performance degradation of device, thus it would be beneficial to include the effect of molecular recombination in the transport simulation. In this work, the anomalous transport is modelled by the multiple-trapping model through the time-fractional drift-diffusion equation. However, the anomalous transport model could be revised to incorporate the spatial disorder of the material through the anomalous hopping which is described based on the Lévy flight dynamics. Thus, anomalous transport produced by the competitiveness between the multiple-trapping and hopping mechanisms could be modelled together. The suggestions for the future works are:

1. charge carrier generation and recombination mechanism could be incorporated in the fractional drift-diffusion equation to account for the molecular recombination of organic semiconductors.
2. the integer order space derivative in the time-fractional drift-diffusion equation could be rewritten in terms of the fractional space derivative to account for the space disorder of the organic semiconductors so that the memory effect embedded in the hopping of charge carrier in space could be modelled by the Lévy flight dynamics.
3. the TFDDE developed in this work is potentially able to be applied to model the transport dynamics of charge carriers and electric field distribution which is produced by the SHG measurement.
4. the TFDDE is not only useful to model the subdiffusive transport dynamics of charge carriers and anomalous current in disordered materials but it could also be used to model the standard transport dynamics of charge carriers in crystalline materials.

REFERENCES

Agarwal, G. S. (1972). Fluctuation-dissipation theorems for systems in non-thermal equilibrium and application to laser light. *Physics Letters A*, *38*(2), 93–95.

Assadi, A., Svensson, C., Willander, M., & Inganäs, O. (1988). Field-effect mobility of poly(3-hexylthiophene). *Applied Physics Letters*, *53*(3), 195–197.

Baeg, K. J., Khim, D. Y., Kim, D. Y., Koo, J. B., You, I. K., Choi, W. S., & Noh, Y. Y. (2010). High mobility top-gated poly(3-hexylthiophene) field-effect transistors with high work-function Pt electrodes. *Thin Solid Films*, *518*(14), 4024–4029.

Balakrishnan, V. (1985). Anomalous diffusion in one dimension. *Physica A: Statistical Mechanics and Its Applications*, *132*(2), 569–580.

Barkai, E. (2001). Fractional Fokker-Planck equation, solution, and application. *Physical Review E*, *63*(4), 46118.

Barkai, E., Metzler, R., & Klafter, J. (2000). From continuous time random walks to the fractional Fokker-Planck equation. *Physical Review E*, *61*(1), 132–138.

Barnsley, M. F. (1993). *Fractals Everywhere* (2nd ed.). Morgan Kaufmann Pub.

Basset, A. B. (1888). *A treatise on hydrodynamics with numerous examples*. University of Michigan Library.

Bässler, H. (1993). Charge transport in disordered organic photoconductors a Monte Carlo simulation study. *Physica Status Solidi (B)*, *175*(1), 15–56.

Bazzani, A., Bassi, G., & Turchetti, G. (2003). Diffusion and memory effects for stochastic processes and fractional Langevin equations. *Physica A: Statistical Mechanics and Its Applications*, *324*(3), 530–550.

Benten, H., Mori, D., Ohkita, H., & Ito, S. (2016). Recent research progress of polymer donor/polymer acceptor blend solar cells. *Journal of Materials Chemistry A*, *4*(15), 5340–5365.

Bhatt, M. P., Magurudeniya, H. D., Rainbolt, E. A., Huang, P., Dissanayake, D. S., Biewer, M. C., & Stefan, M. C. (2014). Poly(3-Hexylthiophene) nanostructured materials for organic electronics applications. *Journal of Nanoscience and Nanotechnology*, *14*(2), 1033–1050.

Bigg, C. (2008). Evident atoms: Visuality in Jean Perrin's Brownian motion research. *Studies in History and Philosophy of Science Part A*, *39*(3), 312–322.

Bisquert, J. (2005). Interpretation of a fractional diffusion equation with nonconserved probability density in terms of experimental systems with trapping or recombination. *Physical Review E*, *72*(1), 11109.

Borsenberger, P. M., Magin, E. H., Van Auweraer, M. Der, & De Schryver, F. C. (1993). The role of disorder on charge transport in molecularly doped polymers and related materials. *Physica Status Solidi (a)*, *140*(1), 9–47.

Brophy, J. J. (1968). Statistics of 1/*f* noise. *Physical Review*, *166*(3), 827–831.

Brophy, J. J. (1969). Variance fluctuations in flicker noise and current noise. *Journal of Applied Physics*, *40*(9), 3551–3553.

Brown, R. (1866). *The miscellaneous botanical works of Robert Brown. Volume 1. I. Geographico-botanical, and, II. Structural and physiological memoirs*. London: The Ray Society.

Burden, L. R., & Faires, J. D. (2011). *Numerical Analysis*. (M. Julet, Ed.) (9e, Intern ed.). Canada: Brooks/Cole, Cengage Learning.

Canus, C., Legrand, P., & Véhel, J. L. (2003). FRACLAB: A Fractal Matlab/Scilab toolbox.

Chandrasekhar, S. (1943). Stochastic problems in physics and astronomy. *Reviews of Modern Physics*, *15*(1), 1–89.

Chen, H., Guo, Y., Yu, G., Zhao, Y., Zhang, J., Gao, D., Liu, H., & Liu, Y. (2012). Highly *π*-extended copolymers with diketopyrrolopyrrole moieties for high-performance field-effect transistors. *Advanced Materials*, *24*(34), 4618–4622.

Chen, Z., Ivanov, P. C., Hu, K., & Stanley, H. E. (2002). Effect of nonstationarities on detrended fluctuation analysis. *Physical Review. E, Statistical, Nonlinear, and Soft Matter Physics*, *65*(4), 41107.

Cheney, W., & Kincaid, D. (2008). *Numerical mathematics and computing* (6th ed.). USA: Thomson Brooks/Cole.

Choi, J., Song, H., Kim, N., & Kim, F. S. (2015). Development of *n*-type polymer semiconductors for organic field-effect transistors. *Semiconductor Science and Technology*, *30*(6), 64002.

Coffey, W. T., Kalmykov, Y. P., & Waldron, J. T. (2004). *The Langevin equation - with applications to stochastic problems in physics, chemistry and electrical engineering (World Scientific series in contemporary chemical physics Vol. 14)* (2nd ed.). World Scientific Publishing Company.

Craciun, N. I. (2011). *Electrical characterization of polymeric charge transport layers*. Groningen.

da Silva Jr., M. P., Lyra, M. L., & Vermelho, M. V. D. (2005). Analog study of the first passage time problem driven by power-law distributed noise. *Physica A: Statistical Mechanics and Its Applications*, *348*, 85–96.

Dang, M. T., Hirsch, L., & Wantz, G. (2011). P3HT:PCBM, best seller in polymer photovoltaic research. *Advanced Materials*, *23*(31), 3597–3602.

Das, R. (2017). *Printed, Organic & Flexible Electronics Forecasts, Players & Opportunities 2017-2027*. USA.

Dong, H., Wang, C., & Hu, W. (2010). High performance organic semiconductors for field-effect transistors. *Chemical Communications*, *46*(29), 5211–5222.

Dong, J., Yu, P., Arabi, S. A., Wang, J., He, J., & Jiang, C. (2016). Enhanced mobility in organic field-effect transistors due to semiconductor/dielectric interface control and very thin single crystal. *Nanotechnology*, *27*(27), 275202.

Dunlap, D. H., & Kenkre, V. M. (1993). Disordered polaron transport: A theoretical description of the motion of photoinjected charges in molecularly doped polymers. *Chemical Physics*, *178*(1–3), 67–75.

Ebata, H., Izawa, T., Miyazaki, E., Takimiya, K., Ikeda, M., Kuwabara, H., & Yui, T. (2007). Highly soluble [1]Benzothieno[3,2-b]benzothiophene (BTBT) derivatives for high-performance, solution-processed organic field-effect transistors. *Journal of the American Chemical Society*, *129*(51), 15732–15733.

Ebisawa, F., Kurokawa, T., & Nara, S. (1983). Electrical properties of polyacetylene/polysiloxane interface. *Journal of Applied Physics*, *54*(6), 3255–3259.

Einstein, A. (1905). Über die von der molekularkinetischen Theorie der Wärme geforderte Bewegung von in ruhenden Flüssigkeiten suspendierten Teilchen. *Annalen Der Physik*, *17*, 549–560.

Falconer, K. (1990). *Fractal geometry: Mathematical foundations and applications*. West Sussex, England: John Wiley & Sons Ltd.

Fick, A. (1855). Ueber Diffusion. *Annalen Der Physik Und Chemie*, *170*(1), 59–86.

Fokker, A. D. (1914). Die mittlere Energie rotierender elektrischer Dipole im Strahlungsfeld. *Annalen Der Physik*, *348*(5), 810–820.

Gajda, J., & Magdziarz, M. (2011). Kramers' escape problem for fractional Klein-Kramers equation with tempered α-stable waiting times. *Physical Review. E, Statistical, Nonlinear, and Soft Matter Physics*, *84*(2), 21137.

Geometric fractals - Chapter 2 fractal dimension. (n.d.). Retrieved December 23, 2016, from http://fractalfoundation.org/OFC/OFC-index.htm

Günther, A. A., Widmer, J., Kasemann, D., & Leo, K. (2015). Hole mobility in thermally evaporated pentacene: Morphological and directional dependence. *Applied Physics Letters*, *106*(23), 233301.

Hartenstein, B., Bässler, H., Heun, S., Borsenberger, P., Van der Auweraer, M., & De Schryver, F. C. (1995). Charge transport in molecularly doped polymers at low dopant concentrations: Simulation and experiment. *Chemical Physics*, *191*(1–3), 321–332.

Hasegawa, T., & Takeya, J. (2009). Organic field-effect transistors using single crystals. *Science and Technology of Advanced Materials*, *10*(2), 24314.

Heeger, A. J., Macdiarmid, A. G., & Shirakawa, H. (2002). Alan J. Heeger, Alan G. MacDiarmid, and Hideki Shirakawa. *Macromolecules*, *35*(4), 1137–1139.

Hilfer, R. (2000a). *Applications of fractional calculus in physics*. Singapore: World Scientific Publishing Co. Pie. Ltd.

Hilfer, R. (2000b). Fractional diffusion based on Riemann-Liouville fractional derivatives. *The Journal of Physical Chemistry B*, *104*(16), 3914–3917.

Ho, S., Liu, S., Chen, Y., & So, F. (2015). Review of recent progress in multilayer solution-processed organic light-emitting diodes. *Journal of Photonics for Energy*, *5*(1), 57611.

Hofmockel, R., Zschieschang, U., Kraft, U., Rödel, R., Hansen, N. H., Stolte, M., Würthner, F., Takimiya, K., Kern, K., Pflaum, J., & Klauk, H. (2013). High-mobility organic thin-film transistors based on a small-molecule semiconductor deposited in vacuum and by solution shearing. *Organic Electronics*, *14*(12), 3213–3221.

Holstein, T. (1959). Studies of polaron motion: Part I. The molecular-crystal model. *Annals of Physics*, *8*(3), 325–342.

Houssa, M., Vandewalle, N., Nigam, T., Ausloos, M., Mertens, P. W., & Heyns, M. M. (1998). Analysis of the gate voltage fluctuations in ultra-thin gate oxides after soft breakdown. In *International Electron Devices Meeting 1998. Technical Digest (Cat. No.98CH36217)* (pp. 909–912).

Hu, K., Ivanov, P. C., Chen, Z., Carpena, P., & Stanley, H. E. (2001). Effect of trends on detrended fluctuation analysis. *Physical Review. E, Statistical, Nonlinear, and Soft Matter Physics*, *64*(1), 11114.

Hughes, B. D. (1995). *Random walks and random environments - Volume 1: Random walks*. Clarendon Press.

Huikuri, H. V, Perkiömäki, J. S., Maestri, R., & Pinna, G. D. (2009). Clinical impact of evaluation of cardiovascular control by novel methods of heart rate dynamics. *Philosophical Transactions of the Royal Society A: Mathematical, Physical and Engineering Sciences*, *367*(1892), 1223–1238.

Huo, Z., Mao, L., Xu, M., & Tan, C. (2003). Low frequency current noise in 2.5 nm MOSFET and fractal dimension of soft breakdown. *Solid-State Electronics*, *47*(9), 1451–1456.

Ignaccolo, M., Jernajczyk, W., Grigolini, P., & West, B. J. (2010). Dynamics of electroencephalogram entropy and pitfalls of scaling detection. *Physical Review. E, Statistical, Nonlinear, and Soft Matter Physics*, *81*(3), 31909.

Irimia-Vladu, M. (2014). "Green" electronics: Biodegradable and biocompatible materials and devices for sustainable future. *Chemical Society Reviews*, *43*(2), 588–610.

Iwamoto, M., Tojima, A., Manaka, T., & Zhong-can, O.-Y. (2003). Compression-shear-induced tilt azimuthal orientation of amphiphilic monolayers at the air-water interface: A $C_\infty \rightarrow C_{2v}$ transition in the flow of a two-dimensional hexatic structure. *Physical Review E*, *67*(4), 41711.

Johanson, R. E., Günes, M., & Kasap, S. O. (2002). Noise in hydrogenated amorphous silicon. *IEE Proceedings - Circuits, Devices and Systems*, *149*(1), 68–74.

Jurchescu, O. D., Hamadani, B. H., Xiong, H. D., Park, S. K., Subramanian, S., Zimmerman, N. M., Anthony, J. E., Jackson, T. N., & Gundlach, D. J. (2008). Correlation between microstructure, electronic properties and flicker noise in organic thin film transistors. *Applied Physics Letters*, *92*(13), 132103.

Juška, G., Arlauskas, K., Viliūnas, M., & Kočka, J. (2000). Extraction current transients: New method of study of charge transport in microcrystalline silicon. *Physical Review Letters*, *84*(21), 4946–4949.

Kalb, W. L., Mathis, T., Haas, S., Stassen, A. F., & Batlogg, B. (2007). Organic small molecule field-effect transistors with Cytop^{TM} gate dielectric: Eliminating gate bias stress effects. *Applied Physics Letters*, *90*(9), 92104.

Kasap, S., & Capper, P. (Eds.). (2006). *Springer Handbook of Electronic and Photonic Materials*. Stürtz GmbH, Würzburg, Germany: Springer Science+Business Media, Inc.

Ke, L., Dolmanan, S., Shen, L., Vijila, C., Chua, S. J., Png, R. Q., Chia, P. J., Chua, L. L., & Ho, P. K. H. (2008). Low frequency noise analysis on organic thin film transistors. *Journal of Applied Physics*, *104*(12), 124502.

Ke, L., Zhao, X. Y., Kumar, R. S., & Chua, S. J. (2006). Low-frequency noise measurement and analysis in organic light-emitting diodes. *IEEE Electron Device Letters*, *27*(7), 555–557.

King, A. (2016). Fractal - A photographic investigation into fractal forms in science and nature. Retrieved January 3, 2017, from http://cargocollective.com/annabelking/Fractal-1

Knauss, D. M., & Huang, T. (2003). ((PS)nPS)m star-shaped polystyrene with star-shaped branches at the terminal chain ends by convergent living anionic polymerization. *Macromolecules*, *36*(16), 6036–6042.

Kong, Y. L., Muniandy, S. V., Fakir, M. S., & Sulaiman, K. (2014). Morphological image interpretation of organic nickel(II) phthalocyanine-tetrasulfonic acid tetrasodium film using fractal analysis. *Applied Surface Science, 301*, 363–368.

Kong, Y. L., Muniandy, S. V., Sulaiman, K., & Fakir, M. S. (2017). Random fractal surface analysis of disordered organic thin films. *Thin Solid Films, 623*, 147–156.

Kubo, R. (1966). The fluctuation-dissipation theorem. *Reports on Progress in Physics*, *29*(1), 255–284.

Lee, J. M., Kim, D. J., Kim, I. Y., Park, K. S., & Kim, S. I. (2004). Nonlinear-analysis of human sleep EEG using detrended fluctuation analysis. *Medical Engineering & Physics*, *26*(9), 773–776.

Likhtenshtein, G. I. (2012). *Solar energy conversion: Chemical aspects*. Wiley-VCH Verlag GmbH.

Lim, S. C., & Muniandy, S. V. (2002). Self-similar Gaussian processes for modeling anomalous diffusion. *Physical Review. E, Statistical, Nonlinear, and Soft Matter Physics*, *66*(2), 21114.

Lin, Y., & Xu, C. (2007). Finite difference/spectral approximations for the time-fractional diffusion equation. *Journal of Computational Physics*, *225*(2), 1533–1552.

Loewe, R. S., Khersonsky, S. M., & McCullough, R. D. (1999). A simple method to prepare head-to-tail coupled, regioregular poly(3-alkylthiophenes) using Grignard metathesis. *Advanced Materials*, *11*(3), 250–253.

Lutz, E. (2001). Fractional Langevin equation. *Physical Review E*, *64*(5), 51106.

Mainardi, F., & Pironi, P. (1996). The fractional Langevin equation Brownian motion revisited. *Extracta Mathematicae*, *11*(1), 140–154.

Manaka, T., Lim, E., Tamura, R., & Iwamoto, M. (2005). Modulation in optical second harmonic generation signal from channel of pentacene field effect transistors during device operation. *Applied Physics Letters*, *87*(22), 222107.

Manaka, T., Lim, E., Tamura, R., Yamada, D., & Iwamoto, M. (2006). Probing of the electric field distribution in organic field effect transistor channel by microscopic second-harmonic generation. *Applied Physics Letters*, *89*(7), 72113.

Mandelbrot, B. B. (1982). *The fractal geometry of nature*. W. H. Freeman and Company.

Mandelbrot, B. B., & Van Ness, J. W. (1968). Fractional Brownian motions, fractional noises and applications. *SIAM Review*, *10*(4), 422–437.

Matsushita, R., Gleria, I., Figueiredo, A., & Da Silva, S. (2007). Are pound and euro the same currency?, *368*(3–4), 173–180.

Mauer, R., Kastler, M., & Laquai, F. (2010). The impact of polymer regioregularity on charge transport and efficiency of P3HT:PCBM photovoltaic devices. *Advanced Functional Materials*, *20*(13), 2085–2092.

Mazo, R. M. (2009). *Brownian motion: Fluctuations, dynamics, and applications*. (International Series of Monographs on Physics (Book 112), Ed.) (1st ed.). Oxford University Press.

Mazzio, K. A., & Luscombe, C. K. (2015). The future of organic photovoltaics. *Chemical Society Reviews*, *44*(1), 78–90.

McMullen, C. T. (1998). Hausdorff dimension and conformal dynamics, III: Computation of dimension. *American Journal of Mathematics*, *120*(4), 691–721.

Metzler, R., Barkai, E., & Klafter, J. (1999). Deriving fractional Fokker-Planck equations from a generalised master equation. *Europhysics Letters*, *46*(4), 431–436.

Metzler, R., & Klafter, J. (2000a). Boundary value problems for fractional diffusion equations. *Physica A: Statistical Mechanics and Its Applications*, *278*(1), 107–125.

Metzler, R., & Klafter, J. (2000b). Subdiffusive transport close to thermal equilibrium: From the Langevin equation to fractional diffusion. *Physical Review E*, *61*(6), 6308–6311.

Metzler, R., & Klafter, J. (2000c). The random walk's guide to anomalous diffusion: A fractional dynamics approach. *Physics Reports*, *339*(1), 1–77.

Metzler, R., & Klafter, J. (2004). The restaurant at the end of the random walk: Recent developments in the description of anomalous transport by fractional dynamics. *Journal of Physics A: Mathematical and General*, *37*(31), R161–R208.

Meyer, M., & Stiedl, O. (2003). Self-affine fractal variability of human heartbeat interval dynamics in health and disease. *European Journal of Applied Physiology*, *90*(3), 305–316.

Milichko, V. A., Shalin, A. S., Mukhin, I. S., Kovrov, A. E., Krasilin, A. A., Vinogradov, A. V., Belov, P. A., & Simovski, C. R. (2016). Solar photovoltaics: Current state and trends. *Physics-Uspekhi*, *59*(8), 727–772.

Miller, A., & Abrahams, E. (1960). Impurity conduction at low concentrations. *Physical Review*, *120*(3), 745–755.

Minemawari, H., Yamada, T., Matsui, H., Tsutsumi, J., Haas, S., Chiba, R., Kumai, R., & Hasegawa, T. (2011). Inkjet printing of single-crystal films. *Nature*, *475*(7356), 364–367.

Mori, T. (2008). Molecular materials for organic field-effect transistors. *Journal of Physics: Condensed Matter*, *20*(18), 184010.

Mott, N. F., & Twose, W. D. (1961). The theory of impurity conduction. *Advances in Physics*, *10*(38), 107–163.

Mozer, A. J., Sariciftci, N. S., Lutsen, L., Vanderzande, D., Österbacka, R., Westerling, M., & Juška, G. (2005). Charge transport and recombination in bulk heterojunction solar cells studied by the photoinduced charge extraction in linearly increasing voltage technique. *Applied Physics Letters*, *86*(11), 112104.

Murio, D. A. (2008a). Implicit finite difference approximation for time fractional diffusion equations. *Computers & Mathematics with Applications*, *56*(4), 1138–1145.

Murio, D. A. (2008b). Time fractional IHCP with Caputo fractional derivatives. *Computers & Mathematics with Applications*, *56*(9), 2371–2381.

Myny, K., van Veenendaal, E., Gelinck, G. H., Genoe, J., Dehaene, W., & Heremans, P. (2012). An 8-bit, 40-instructions-per-second organic microprocessor on plastic foil. *IEEE Journal of Solid-State Circuits*, *47*(1), 284–291.

Nawaz, A., Meruvia, M. S., Tarange, D. L., Gopinathan, S. P., Kumar, A., Kumar, A., Bhunia, H., Pal, A. J., & Hümmelgen, I. A. (2016). High mobility organic field-effect transistors based on defect-free regioregular poly(3-hexylthiophene-2,5-diyl). *Organic Electronics*, *38*, 89–96.

Nelkin, M., & Harrison, A. K. (1982). Random-walk model for the saturation of 1/*f* noise amplitudes. *Physical Review B*, *26*(12), 6696–6705.

Øksendal, B. (2003). *Stochastic differential equations*. Berlin, Heidelberg: Springer Berlin Heidelberg.

Pénarier, A., Jarrix, S. G., Delseny, C., Pascal, F., Vildeuil, J. C., Valenza, M., & Rigaud, D. (2002). Low-frequency noise in III–V high-speed devices. *IEE Proceedings - Circuits, Devices and Systems*, *149*(1), 59–67.

Peng, C. K., Buldyrev, S. V., Havlin, S., Simons, M., Stanley, H. E., & Goldberger, A. L. (1994). Mosaic organization of DNA nucleotides. *Physical Review E*, *49*(2), 1685–1689.

Peng, C. K., Havlin, S., Stanley, H. E., & Goldberger, A. L. (1995). Quantification of scaling exponents and crossover phenomena in nonstationary heartbeat time series. *Chaos (Woodbury, N.Y.)*, *5*(1), 82–87.

Penzel, T., Kantelhardt, J. W., Grote, L., Peter, J. H., & Bunde, A. (2003). Comparison of detrended fluctuation analysis and spectral analysis for heart rate variability in sleep and sleep apnea. *IEEE Transactions on Biomedical Engineering*, *50*(10), 1143–1151.

Perrin, J., Macleod, A. R., & Soddy, F. (1910). *Brownian movement and molecular reality*. London: Taylor and Francis.

Pivrikas, A., Juska, G., Arlauskas, K., Scharber, M., Mozer, A., Sariciftci, N. S., Stubb, H., & Österbacka, R. (2005). Charge carrier transport and recombination in bulk-heterojunction solar-cells. In Z. H. Kafafi & P. A. Lane (Eds.) (p. 59380N).

Podlubny, I. (Ed.). (1998). *Fractional differential equations: An introduction to fractional derivatives, fractional differential equations, to methods of their solution and some of their applications*. USA: Academic Press.

Risken, H., & Frank, T. (1996). *The Fokker-Planck equation: Methods of solution and applications (Springer series in synergetics, book 18)*. (H. Haken, Ed.) (2nd ed.). Berlin Heidelberg: Springer-Verlag.

Sapoval, B., Rosso, M., & Gouyet, J. F. (1985). The fractal nature of a diffusion front and the relation to percolation. *Journal de Physique Lettres*, *46*(4), 149–156.

Scalas, E., Gorenflo, R., & Mainardi, F. (2000). Fractional calculus and continuous-time finance. *Physica A: Statistical Mechanics and Its Applications*, *284*(1–4), 376–384.

Scher, H., & Montroll, E. W. (1975). Anomalous transit-time dispersion in amorphous solids. *Physical Review B*, *12*(6), 2455–2477.

Schmidt, R., Oh, J. H., Sun, Y. Sen, Deppisch, M., Krause, A. M., Radacki, K., Braunschweig, H., Könemann, M., Erk, P., Bao, Z., & Würthner, F. (2009). High-performance air-stable *n*-channel organic thin film transistors based on halogenated perylene bisimide semiconductors. *Journal of the American Chemical Society*, *131*(17), 6215–6228.

Schneider, W. R., & Wyss, W. (1989). Fractional diffusion and wave equations. *Journal of Mathematical Physics*, *30*(1), 134–144.

Sekine, C., Tsubata, Y., Yamada, T., Kitano, M., & Doi, S. (2014). Recent progress of high performance polymer OLED and OPV materials for organic printed electronics. *Science and Technology of Advanced Materials*, *15*(3), 34203.

Shiau, Y. H. (2011). Understanding as well as characterization of erratic interspike dynamics in semiconductor devices, *151*(2), 135–138.

Shirota, Y., & Kageyama, H. (2007). Charge carrier transporting molecular materials and their applications in devices. *Chemical Reviews*, *107*(4), 953–1010.

Shukla, D., Nelson, S. F., Freeman, D. C., Rajeswaran, M., Ahearn, W. G., Meyer, D. M., & Carey, J. T. (2008). Thin-film morphology control in naphthalene-diimide-based semiconductors: High mobility *n*-type semiconductor for organic thin-film transistors. *Chemistry of Materials*, *20*(24), 7486–7491.

Sibatov, R. T., & Uchaikin, V. V. (2007). Fractional differential kinetics of charge transport in unordered semiconductors. *Semiconductors*, *41*(3), 335–340.

Sibatov, R. T., & Uchaikin, V. V. (2009). Fractional differential approach to dispersive transport in semiconductors. *Physics-Uspekhi*, *52*(10), 1019–1043.

Silva, L. B. M., Vermelho, M. V. D., Lyra, M. L., & Viswanathan, G. M. (2009). Multifractal detrended fluctuation analysis of analog random multiplicative processes. *Chaos, Solitons & Fractals*, *41*(5), 2806–2811.

Sirringhaus, H. (2014). 25th anniversary article: Organic field-effect transistors: The path beyond amorphous silicon. *Advanced Materials*, *26*(9), 1319–1335.

Sokolov, I. M., Klafter, J., & Blumen, A. (2002). Fractional kinetics. *Physics Today*, *55*(11), 48–54.

Sousa, E. (2012). How to approximate the fractional derivative of order $1 < \alpha \leq 2$. *International Journal Bifurcation and Chaos*, *22*(4), 1250075.

Stafström, S. (2010). Electron localization and the transition from adiabatic to nonadiabatic charge transport in organic conductors. *Chemical Society Reviews*, *39*(7), 2484–2499.

Stanley, H. E. (1984). Application of fractal concepts to polymer statistics and to anomalous transport in randomly porous media. *Journal of Statistical Physics*, *36*(5), 843–860.

Sun, H., Chen, W., Li, C., & Chen, Y. (2012). Finite difference schemes for variable-order time fractional diffusion eqaution. *International Journal of Bifurcation and Chaos*, *22*(4), 1250085.

Takamatsu, A., Takaba, E., & Takizawa, G. (2009). Environment-dependent morphology in plasmodium of true slime mold Physarum polycephalum and a network growth model. *Journal of Theoretical Biology*, *256*(1), 29–44.

Tanase, C., Meijer, E. J., Blom, P. W. M., & De Leeuw, D. M. (2003). Unification of the hole transport in polymeric field-effect transistors and light-emitting diodes. *Physical Review Letters*, *91*(21), 216601.

Terje, A. S., & Reynolds, J. (Eds.). (2006). *Handbook of conducting polymers - conjugated polymers: Processing and applications* (3rd ed.). U.S.A.: CRC Press.

Tessler, N., Preezant, Y., Rappaport, N., & Roichman, Y. (2009). Charge transport in disordered organic materials and its relevance to thin-film devices: A tutorial review. *Advanced Materials*, *21*(27), 2741–2761.

Tiwari, S., & Greenham, N. C. (2009). Charge mobility measurement techniques in organic semiconductors. *Optical and Quantum Electronics*, *41*(2), 69–89.

Tsumura, A., Koezuka, H., & Ando, T. (1986). Macromolecular electronic device: Field-effect transistor with a polythiophene thin film. *Applied Physics Letters*, *49*(18), 1210–1212.

Turner, M. J., Blackledge, J. M., & Andrews, P. R. (1998). *Fractal geometry in digital imaging*. San Diego, USA: Academic Press.

Uchaikin, V. V., & Sibatov, R. T. (2008). Fractional theory for transport in disordered semiconductors. *Communications in Nonlinear Science and Numerical Simulation*, *13*(4), 715–727.

Uchaikin, V. V., & Sibatov, R. T. (2013). *Fractional kinetics in solids: Anomalous charge transport in semiconductors, dielectrics and nanosystems*. Singapore: World Scientific Publishing Co. Pte. Ltd.

von Smoluchowski, M. (2010). Versuch einer mathematischen Theorie der Koagulationskinetik kolloider Lösungen. *Zeitschrift Fuer Physikalische Chemie*, *92*, 129–168.

Wang, L., He, X., & Chen, Y. (2011). Diffusion-limited hyperbranched polymers with substitution effect. *The Journal of Chemical Physics*, *134*(10), 104901.

Wiener, N. (1923). Differential-space. *Journal of Mathematics and Physics*, *2*(1–4), 131–174.

Witten, T. A., & Sander, L. M. (1983). Diffusion-limited aggregation. *Physical Review B*, *27*(9), 5686–5697.

Wool, R. P., & Long, J. M. (1993). Fractal structure of polymer interfaces. *Macromolecules*, *26*(19), 5227–5239.

Wyss, W. (1986). The fractional diffusion equation. *Journal of Mathematical Physics*, *27*(11), 2782–2785.

Xu, Y., Minari, T., Tsukagoshi, K., Gwoziecki, R., Coppard, R., Balestra, F., Chroboczek, J. A., & Ghibaudo, G. (2010). Extraction of low-frequency noise in contact resistance of organic field-effect transistors. *Applied Physics Letters*, *97*(3), 33503.

Yang, Q., Liu, F., & Turner, I. (2009). Computationally efficient numerical methods for time- and space-fractional Fokker–Planck equations. *Physica Scripta*, *T136*, 14026.

Zhao, Y., Guo, Y., & Liu, Y. (2013). 25th anniversary article: Recent advances in *n*-type and ambipolar organic field-effect transistors. *Advanced Materials*, *25*(38), 5372–5391.

Zwanzig, R. (2001). *Nonequilibrium statistical mechanics*. New York, USA: Oxford University Press.

LIST OF PUBLICATIONS AND PAPERS PRESENTED

Journal papers

1. **Choo**, **K. Y.**, Muniandy, S. V., Chua, C. L. and Woon, K. L. (2012). Scaling behaviors of transient noise current in organic field-effect transistors. *Organic Electronics, 13*(8), 1370-1376.

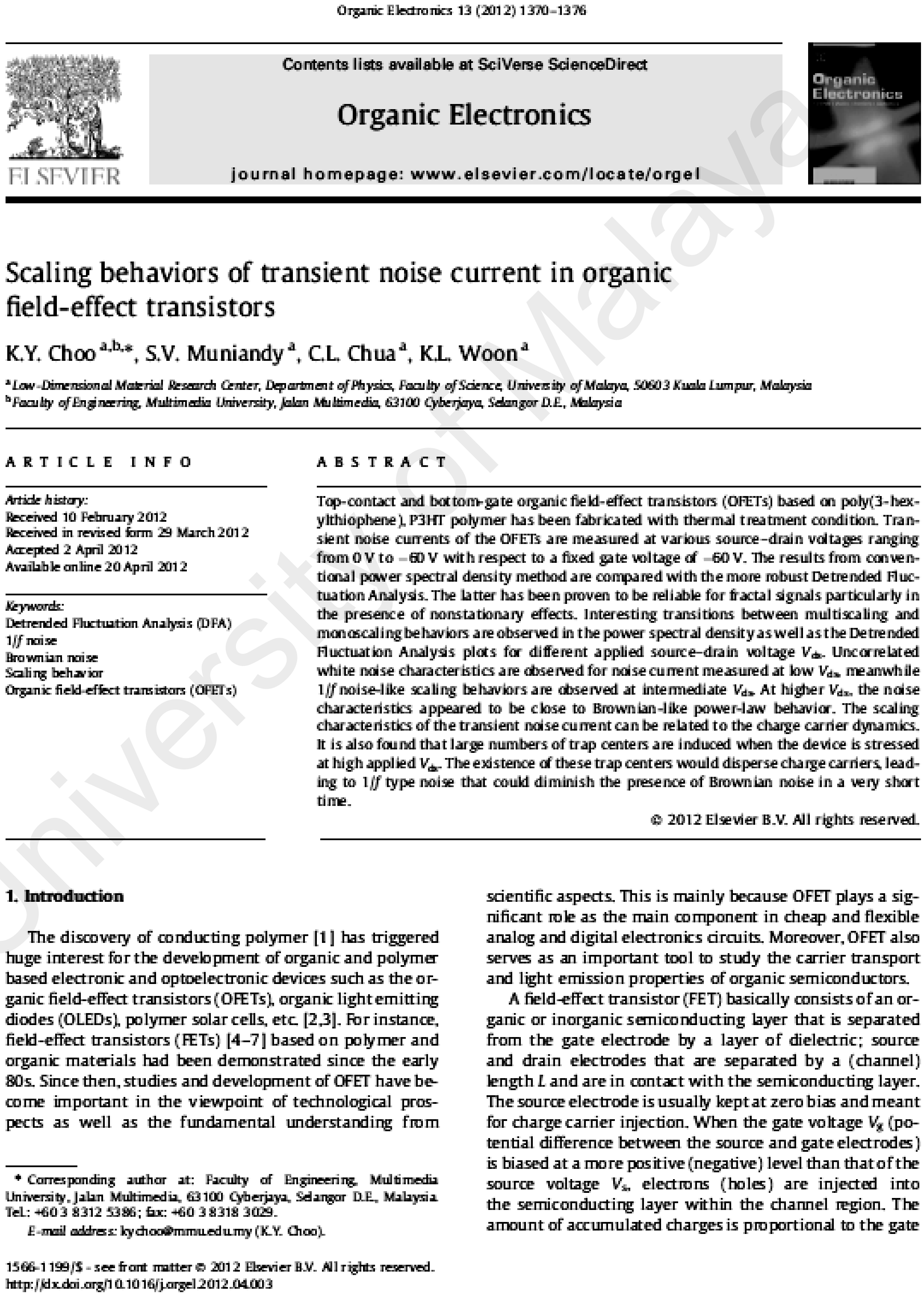

Organic Electronics 13 (2012) 1370–1376

Contents lists available at SciVerse ScienceDirect

Organic Electronics

journal homepage: www.elsevier.com/locate/orgel

Scaling behaviors of transient noise current in organic field-effect transistors

K.Y. Choo [a,b,*], S.V. Muniandy [a], C.L. Chua [a], K.L. Woon [a]

[a] *Low-Dimensional Material Research Center, Department of Physics, Faculty of Science, University of Malaya, 50603 Kuala Lumpur, Malaysia*
[b] *Faculty of Engineering, Multimedia University, Jalan Multimedia, 63100 Cyberjaya, Selangor D.E., Malaysia*

ARTICLE INFO

Article history:
Received 10 February 2012
Received in revised form 29 March 2012
Accepted 2 April 2012
Available online 20 April 2012

Keywords:
Detrended Fluctuation Analysis (DFA)
1/*f* noise
Brownian noise
Scaling behavior
Organic field-effect transistors (OFETs)

ABSTRACT

Top-contact and bottom-gate organic field-effect transistors (OFETs) based on poly(3-hexylthiophene), P3HT polymer has been fabricated with thermal treatment condition. Transient noise currents of the OFETs are measured at various source–drain voltages ranging from 0 V to −60 V with respect to a fixed gate voltage of −60 V. The results from conventional power spectral density method are compared with the more robust Detrended Fluctuation Analysis. The latter has been proven to be reliable for fractal signals particularly in the presence of nonstationary effects. Interesting transitions between multiscaling and monoscaling behaviors are observed in the power spectral density as well as the Detrended Fluctuation Analysis plots for different applied source–drain voltage V_{ds}. Uncorrelated white noise characteristics are observed for noise current measured at low V_{ds}, meanwhile 1/*f* noise-like scaling behaviors are observed at intermediate V_{ds}. At higher V_{ds}, the noise characteristics appeared to be close to Brownian-like power-law behavior. The scaling characteristics of the transient noise current can be related to the charge carrier dynamics. It is also found that large numbers of trap centers are induced when the device is stressed at high applied V_{ds}. The existence of these trap centers would disperse charge carriers, leading to 1/*f* type noise that could diminish the presence of Brownian noise in a very short time.

1. Introduction

The discovery of conducting polymer [1] has triggered huge interest for the development of organic and polymer based electronic and optoelectronic devices such as the organic field-effect transistors (OFETs), organic light emitting diodes (OLEDs), polymer solar cells, etc. [2,3]. For instance, field-effect transistors (FETs) [4–7] based on polymer and organic materials had been demonstrated since the early 80s. Since then, studies and development of OFET have become important in the viewpoint of technological prospects as well as the fundamental understanding from scientific aspects. This is mainly because OFET plays a significant role as the main component in cheap and flexible analog and digital electronics circuits. Moreover, OFET also serves as an important tool to study the carrier transport and light emission properties of organic semiconductors.

A field-effect transistor (FET) basically consists of an organic or inorganic semiconducting layer that is separated from the gate electrode by a layer of dielectric; source and drain electrodes that are separated by a (channel) length *L* and are in contact with the semiconducting layer. The source electrode is usually kept at zero bias and meant for charge carrier injection. When the gate voltage V_g (potential difference between the source and gate electrodes) is biased at a more positive (negative) level than that of the source voltage V_s, electrons (holes) are injected into the semiconducting layer within the channel region. The amount of accumulated charges is proportional to the gate

---

[*] Corresponding author at: Faculty of Engineering, Multimedia University, Jalan Multimedia, 63100 Cyberjaya, Selangor D.E., Malaysia. Tel.: +60 3 8312 5386; fax: +60 3 8318 3029.
E-mail address: kychoo@mmu.edu.my (K.Y. Choo).

1566-1199/$ - see front matter © 2012 Elsevier B.V. All rights reserved.
http://dx.doi.org/10.1016/j.orgel.2012.04.003

2. **Choo**, **K. Y.**, Muniandy, S. V., Woon, K. L., Gan, M. T. and Ong, D. S. (2017). Modeling anomalous charge carrier transport in disordered organic semiconductors using the fractional drift-diffusion equation. *Organic Electronics*, *41*, 157-165.

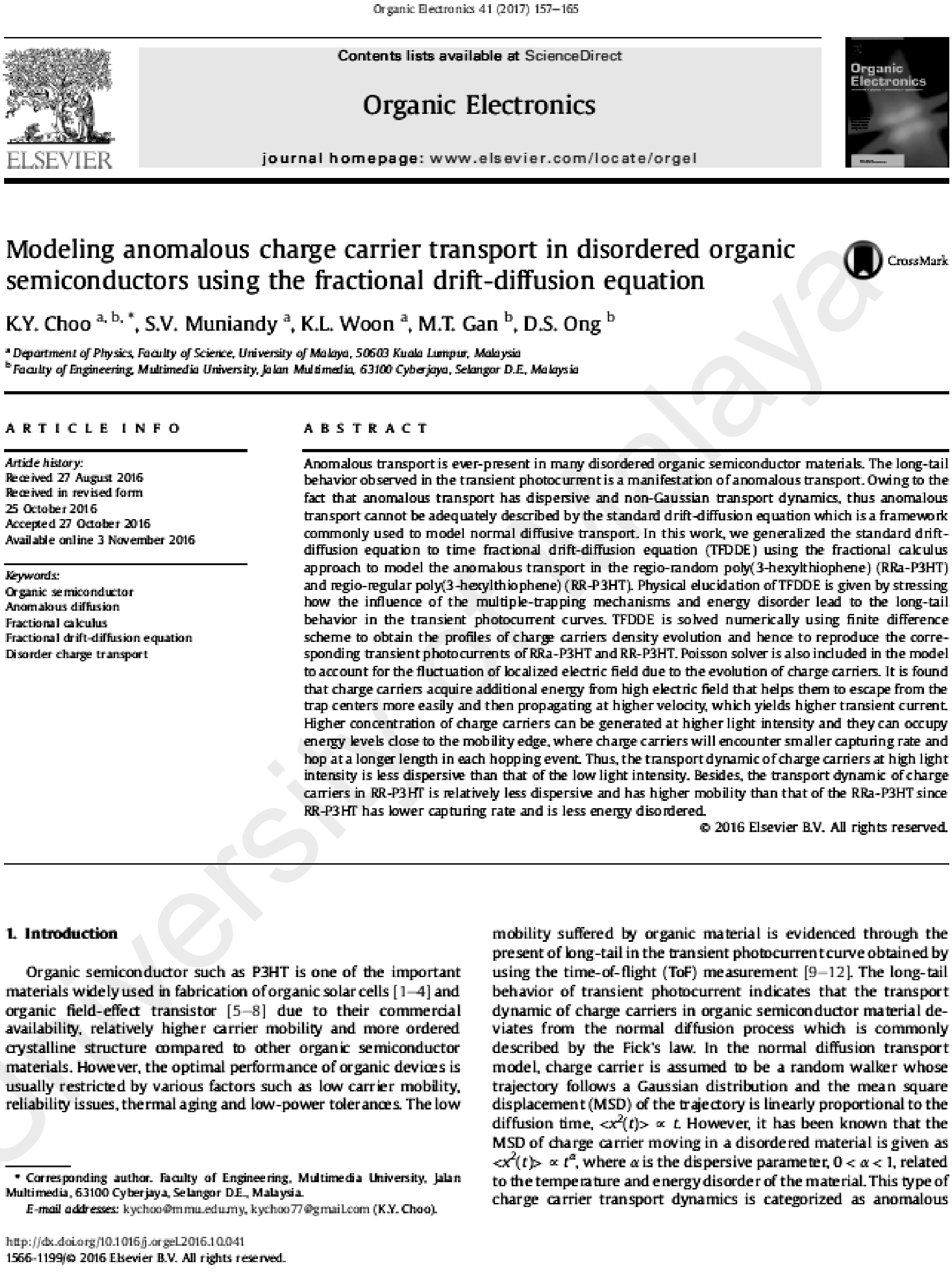

Organic Electronics 41 (2017) 157–165

Contents lists available at ScienceDirect

Organic Electronics

journal homepage: www.elsevier.com/locate/orgel

Modeling anomalous charge carrier transport in disordered organic semiconductors using the fractional drift-diffusion equation

K.Y. Choo [a, b, *], S.V. Muniandy [a], K.L. Woon [a], M.T. Gan [b], D.S. Ong [b]

[a] *Department of Physics, Faculty of Science, University of Malaya, 50603 Kuala Lumpur, Malaysia*
[b] *Faculty of Engineering, Multimedia University, Jalan Multimedia, 63100 Cyberjaya, Selangor D.E., Malaysia*

A R T I C L E I N F O

Article history:
Received 27 August 2016
Received in revised form
25 October 2016
Accepted 27 October 2016
Available online 3 November 2016

Keywords:
Organic semiconductor
Anomalous diffusion
Fractional calculus
Fractional drift-diffusion equation
Disorder charge transport

A B S T R A C T

Anomalous transport is ever-present in many disordered organic semiconductor materials. The long-tail behavior observed in the transient photocurrent is a manifestation of anomalous transport. Owing to the fact that anomalous transport has dispersive and non-Gaussian transport dynamics, thus anomalous transport cannot be adequately described by the standard drift-diffusion equation which is a framework commonly used to model normal diffusive transport. In this work, we generalized the standard drift-diffusion equation to time fractional drift-diffusion equation (TFDDE) using the fractional calculus approach to model the anomalous transport in the regio-random poly(3-hexylthiophene) (RRa-P3HT) and regio-regular poly(3-hexylthiophene) (RR-P3HT). Physical elucidation of TFDDE is given by stressing how the influence of the multiple-trapping mechanisms and energy disorder lead to the long-tail behavior in the transient photocurrent curves. TFDDE is solved numerically using finite difference scheme to obtain the profiles of charge carriers density evolution and hence to reproduce the corresponding transient photocurrents of RRa-P3HT and RR-P3HT. Poisson solver is also included in the model to account for the fluctuation of localized electric field due to the evolution of charge carriers. It is found that charge carriers acquire additional energy from high electric field that helps them to escape from the trap centers more easily and then propagating at higher velocity, which yields higher transient current. Higher concentration of charge carriers can be generated at higher light intensity and they can occupy energy levels close to the mobility edge, where charge carriers will encounter smaller capturing rate and hop at a longer length in each hopping event. Thus, the transport dynamic of charge carriers at high light intensity is less dispersive than that of the low light intensity. Besides, the transport dynamic of charge carriers in RR-P3HT is relatively less dispersive and has higher mobility than that of the RRa-P3HT since RR-P3HT has lower capturing rate and is less energy disordered.

1. Introduction

Organic semiconductor such as P3HT is one of the important materials widely used in fabrication of organic solar cells [1–4] and organic field-effect transistor [5–8] due to their commercial availability, relatively higher carrier mobility and more ordered crystalline structure compared to other organic semiconductor materials. However, the optimal performance of organic devices is usually restricted by various factors such as low carrier mobility, reliability issues, thermal aging and low-power tolerances. The low mobility suffered by organic material is evidenced through the present of long-tail in the transient photocurrent curve obtained by using the time-of-flight (ToF) measurement [9–12]. The long-tail behavior of transient photocurrent indicates that the transport dynamic of charge carriers in organic semiconductor material deviates from the normal diffusion process which is commonly described by the Fick's law. In the normal diffusion transport model, charge carrier is assumed to be a random walker whose trajectory follows a Gaussian distribution and the mean square displacement (MSD) of the trajectory is linearly proportional to the diffusion time, $<x^2(t)> \propto t$. However, it has been known that the MSD of charge carrier moving in a disordered material is given as $<x^2(t)> \propto t^\alpha$, where α is the dispersive parameter, $0 < \alpha < 1$, related to the temperature and energy disorder of the material. This type of charge carrier transport dynamics is categorized as anomalous

---

* Corresponding author. Faculty of Engineering, Multimedia University, Jalan Multimedia, 63100 Cyberjaya, Selangor D.E., Malaysia.
E-mail addresses: kychoo@mmu.edu.my, kychoo77@gmail.com (K.Y. Choo).

http://dx.doi.org/10.1016/j.orgel.2016.10.041

Proceeding/Conference papers

1. Muniandy, S. V., Woon, K. L. and **Choo, K. Y.** (2011). Anomalous charge transport in disordered organic semiconductors. *AIP Conf. Proc. Malaysia Annual Physics Conference, 1328,* 38-42.

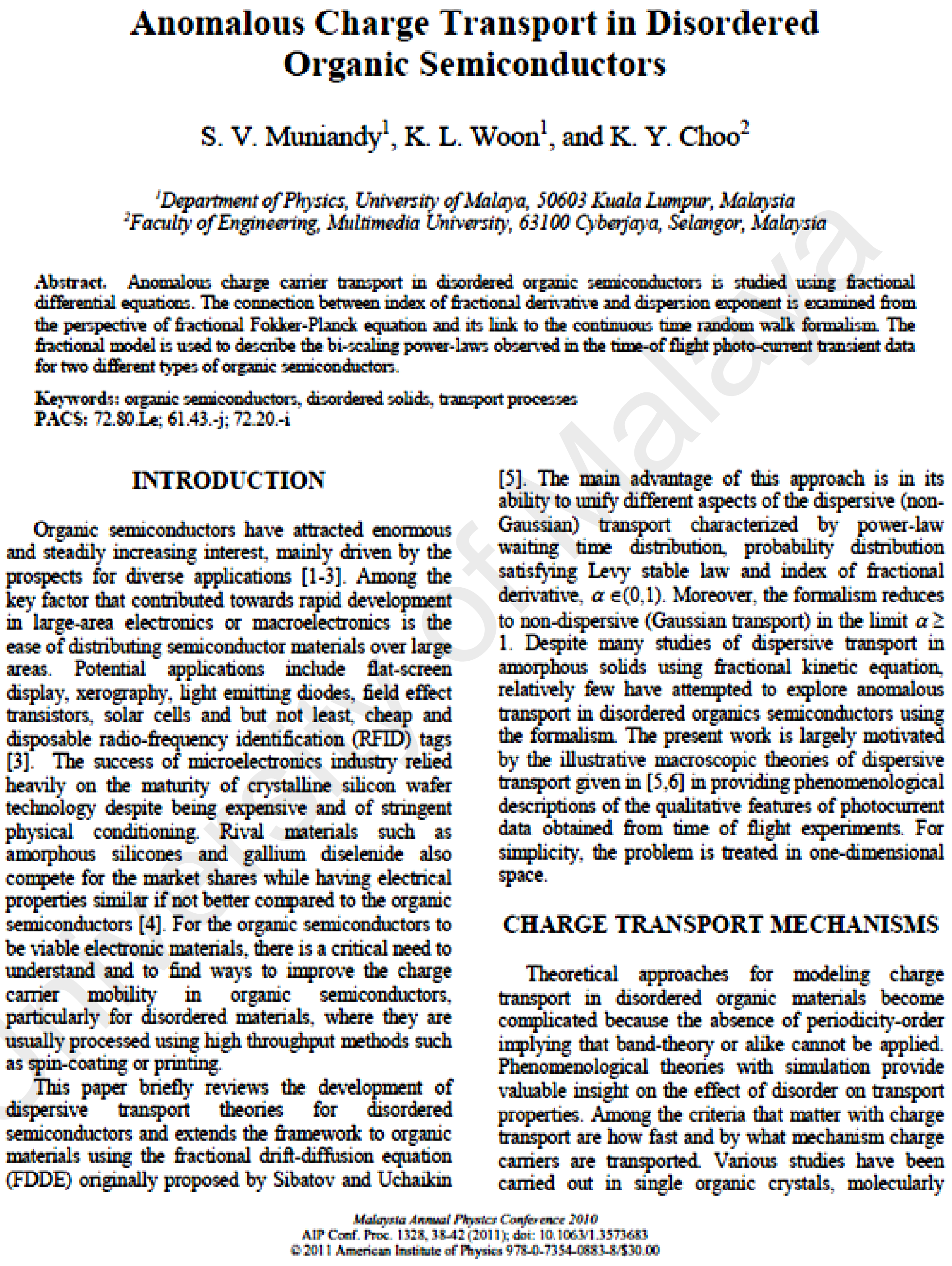

Anomalous Charge Transport in Disordered Organic Semiconductors

S. V. Muniandy[1], K. L. Woon[1], and K. Y. Choo[2]

[1]*Department of Physics, University of Malaya, 50603 Kuala Lumpur, Malaysia*
[2]*Faculty of Engineering, Multimedia University, 63100 Cyberjaya, Selangor, Malaysia*

Abstract. Anomalous charge carrier transport in disordered organic semiconductors is studied using fractional differential equations. The connection between index of fractional derivative and dispersion exponent is examined from the perspective of fractional Fokker-Planck equation and its link to the continuous time random walk formalism. The fractional model is used to describe the bi-scaling power-laws observed in the time-of flight photo-current transient data for two different types of organic semiconductors.

Keywords: organic semiconductors, disordered solids, transport processes
PACS: 72.80.Le; 61.43.-j; 72.20.-i

INTRODUCTION

Organic semiconductors have attracted enormous and steadily increasing interest, mainly driven by the prospects for diverse applications [1-3]. Among the key factor that contributed towards rapid development in large-area electronics or macroelectronics is the ease of distributing semiconductor materials over large areas. Potential applications include flat-screen display, xerography, light emitting diodes, field effect transistors, solar cells and but not least, cheap and disposable radio-frequency identification (RFID) tags [3]. The success of microelectronics industry relied heavily on the maturity of crystalline silicon wafer technology despite being expensive and of stringent physical conditioning. Rival materials such as amorphous silicones and gallium diselenide also compete for the market shares while having electrical properties similar if not better compared to the organic semiconductors [4]. For the organic semiconductors to be viable electronic materials, there is a critical need to understand and to find ways to improve the charge carrier mobility in organic semiconductors, particularly for disordered materials, where they are usually processed using high throughput methods such as spin-coating or printing.

This paper briefly reviews the development of dispersive transport theories for disordered semiconductors and extends the framework to organic materials using the fractional drift-diffusion equation (FDDE) originally proposed by Sibatov and Uchaikin [5]. The main advantage of this approach is in its ability to unify different aspects of the dispersive (non-Gaussian) transport characterized by power-law waiting time distribution, probability distribution satisfying Levy stable law and index of fractional derivative, $\alpha \in (0,1)$. Moreover, the formalism reduces to non-dispersive (Gaussian transport) in the limit $\alpha \geq 1$. Despite many studies of dispersive transport in amorphous solids using fractional kinetic equation, relatively few have attempted to explore anomalous transport in disordered organics semiconductors using the formalism. The present work is largely motivated by the illustrative macroscopic theories of dispersive transport given in [5,6] in providing phenomenological descriptions of the qualitative features of photocurrent data obtained from time of flight experiments. For simplicity, the problem is treated in one-dimensional space.

CHARGE TRANSPORT MECHANISMS

Theoretical approaches for modeling charge transport in disordered organic materials become complicated because the absence of periodicity-order implying that band-theory or alike cannot be applied. Phenomenological theories with simulation provide valuable insight on the effect of disorder on transport properties. Among the criteria that matter with charge transport are how fast and by what mechanism charge carriers are transported. Various studies have been carried out in single organic crystals, molecularly

Malaysia Annual Physics Conference 2010
AIP Conf. Proc. 1328, 38-42 (2011); doi: 10.1063/1.3573683

2. **Choo, K. Y.** and Muniandy, S. V. (2015). Fractional dispersive transport in inhomogeneous organic semiconductors. *Int. J. Mod. Phys.: Conf.*, *36*, 1560008 (16 pages).

7th Jagna International Workshop (2014)
International Journal of Modern Physics: Conference Series
Vol. 36 (2015) 1560008 (16 pages)

DOI: 10.1142/S2010194515600083

Fractional dispersive transport in inhomogeneous organic semiconductors

K. Y. Choo* and S. V. Muniandy†
Department of Physics, University of Malaya,
50603, Kuala Lumpur, Malaysia
†*msithi@um.edu.my*
http://fizik.um.edu.my/svm/Profile.html

Published 2 January 2015

The study of transport dynamics of charge carriers in homogeneous and inhomogeneous organic semiconductor using the variable order time-fractional drift-diffusion equation (VO-TFDDE) is presented in this paper. The fractional-time derivative operator and spatial derivative operator of the time-fractional drift-diffusion equation are discretized respectively using the implicit difference scheme and the centered difference scheme. Self-consistent Poisson solver was incorporated in the model to solve for the electric potential and the localized electric field that sweeps the charge carriers across the device. The homogeneity of the material is represented by the different values or functions of the fractional derivative order. Diffusion transport dynamics is observed when charge carriers are moving in homogeneous crystalline-like structure. In contrast, dispersive transport dynamics is observed when charge carriers are moving in homogeneous amorphous-like structure. For inhomogeneous amorphous-crystalline-mixed structure, pulse broadening effect is impeded as charge carriers are moving towards the crystalline-like region at the other end of the device. Conversely, pulse broadening effect is getting severe if charge carriers are moving across the device with inhomogeneous crystalline-amorphous-mixed structure. Therefore, in order to achieve diffusive-like transport dynamics that could reduce the pulse broadening effect, homogeneous crystalline-like structure or inhomogeneous amorphous-crystalline-mixed structure is recommended for device fabrication.

Keywords: Fractional diffusion equation; dispersive transport; organic semiconductor.

1. Introduction

The discovery of conducting polymer, polyacetylene doped with halogens in 1977 by Heeger, MacDiarmid and Shirakawa has triggered tremendous research in organic electronic materials[1]. Extensive collaborative efforts among physicists, chemists,

[*] The author is also affiliated to the Faculty of Engineering, Multimedia University, Jalan Multimedia, 63100 Cyberjaya, Selangor D.E., Malaysia. Email: kychoo@mmu.edu.my

Conference/Symposium Presentations

1. **Choo**, **K. Y.**, Muniandy, S. V., Woon, K. L., Gan, M. T. and Ong, D. S. (2015). Dispersive charge transport study in periodic structures of crystalline-amorphous hybrid organic materials. *8th Conference of Asian Consortium on Computational Materials Science* (ACCMS-8), National Taiwan University of Science and Technology (NTUST), Taipei, Taiwan on June 16-18. 2015.

2. **Choo**, **K. Y.**, Muniandy, S. V., Woon, K. L., Gan, M. T. and Ong, D. S. (2015). Fractional dynamics of dispersive transport in organic semiconductors. *University of Malaya-Academia Sinica Research Symposium*, University of Malaya, Kuala Lumpur, Malaysia on 18 November 2015.